EFFECTS OF LOW-CETANE FUELS IN COMPRESSION IGNITION ENGINES

by

MAXIM MICHAEL JARMOLUK

A thesis submitted in partial fulfillment of the
requirements for the degree of

MASTER OF SCIENCE IN MECHANICAL ENGINEERING

2026

Oakland University
Rochester, Michigan

Thesis Advisory Committee:

Dan DelVescovo, Ph.D., Chair
Marco Gerini-Romagnoli, Ph.D.
Yongsoon Yoon, Ph.D.
Michael Tess, Ph.D.
Joshua Piehl, Ph.D.

EFFECTS OF LOW-CETANE FUELS IN COMPRESSION IGNITION ENGINES

by

MAXIM MICHAEL JARMOLUK

ADVISOR: DAN DELVESCOVO

Abstract

The U.S. Army requires blended fuels to have a cetane rating of at least 40, but sustainable aviation fuels (SAFs) have very low cetane numbers (DCN ~15), causing delayed combustion. While the link between altered combustion and engine wear is known, this thesis directly correlates low-cetane fuels with specific durability indicators.

A CI V8 engine was tested with a baseline fuel (DCN 43.7) and two low-cetane fuels (DCN 34.8, 29.8) across 19 operating conditions. Peak pressure, pressure rise rate, and crankshaft twist were synthesized into a novel Composite Durability Indicator (CDI).

CDI results show low-cetane fuels increase durability concerns at high- and low-speed conditions relative to identical conditions at baseline, but these increases only exceed the maximum baseline concern at high speeds. At high speed, crankshaft twist was found to bias opposite the direction of rotation, suspected to result from elevated cylinder pressure during the compression stroke.

Table of Contents

List of Tables

List of Figures

List of Figures — Continued

List of Figures — Continued

Chapter 1 Introduction

A form of synthetic fuels, sustainable aviation fuels (SAF) are becoming more prevalent as the aviation industry is moving to reduce emissions. The current most common form of SAF uses hydro-processed esters and fatty acids (HEFA), such as used cooking oils, as the feedstock. However, even at full capacity, HEFA-derived fuels could only meet 13% of the current demand for jet fuel [13]. With demand expected to increase, an alternative will be needed, and alcohol-to-jet fuel (ATJ) is already filling that gap worldwide. Advantages of ATJ include the variety of feedstock pathways and the ability to be blended with conventional jet fuel up to 50%, matching the amount HEFA-derived fuels may be blended [12].

Synthetic jet fuels are qualified for operation use in U.S. military ground vehicles on a limited basis. However, fuels consisting of blends of conventional and synthetic jet fuels must have minimum derived cetane number (DCN) of 40 [23]. Cetane number measures the propensity of a fuel to auto ignite [22], with a higher cetane number indicating a greater tendency to do so.

An issue arises with both of these conditions above intervene, that being that ATJ has a DCN of ~15 [3][52] much lower that permissible for military ground vehicles. The mandate described above is implemented to prevent low-cetane effects in the military engines. The main effect of low-cetane combustion is an increase in ignition delay. This increase in ignition delay results in more fuel being present in the cylinder when combustion starts. Therefore, as combustion starts there is an increase in pressure rise rate resulting in a higher peak pressure in the cylinder. This is effect is documented to be most predominant at low to medium loads [17][20][24].

Separate research has concluded that increases in peak pressure and pressure rise rate present durability concerns. A increase in pressure and consequently temperature within the cylinder were found to accelerate cylinder head cracking, specifically in the valve bridge region [29][30]. Additionally, increases in cylinder pressure were found to increase the maximum film pressure for piston rings, as well as the asperity contact force between the piston rings and cylinder wall [31][31]. Both of which may lead to scuffing of the cylinder wall. Increases in pressure rise rate have been found to increase engine vibration as well as piston slap [35]. In addition, excessive piston slap and the resulting cylinder liner vibration has been found to cause cavitation in diesel engines with wet cylinder liner configurations [36][37][38][39][38][39].

Continuing, peak pressure and pressure rise rate have been found to cause additional secondary effects of ignition delay which are cause for durability concern. Increases in both peak pressure and pressure rise rate were found to increase crankshaft torsion [40], which has been thoroughly studied for the purpose of mitigating [41][42][43]. This is because crankshaft torsion, along with crankshaft bending, having been found to be the main causes of fatigue failure in crankshafts [44][45][48]. More specifically, models for determining fatigue life of crankshafts effectively model real conditions when incorporating both the maximum torsional stress and cyclic torsional strain range [46]. Additionally, crankshaft torsion is not constant for all engine speeds and, as expected, increases as the torsional vibration of the crankshaft approaches the resonant frequency of the crankshaft [27][50], adding another region that may be exaggerated by low-cetane fuels.

With the listed possible ramifications of using low-cetane fuels, it is necessary to fully understand their durability impact for military ground vehicles as well as directly link low-cetane effects to possible durability concerns. This was done through the instrumentation of a compression ignition V8 engine to observe cylinder pressure and crankshaft twist. This engine was run on three fuels ranging in DCN from 43.7 to 29.8 at 19 different operating conditions, ranging in speed and load. The process for analyzing the collected data is outlined in the following paragraphs.

The decision of what metrics to be used to indicate durability effects was guided by literature, including the reasoning provided above. Wear indicators chosen include peak pressure, pressure rise rate, and three crankshaft twist metrics including absolute twist, peak-to-peak twist, and rate of crankshaft twist. The inclusion of the crankshaft twist metrics and observing the low-cetane effects is a major contribution of this research. Each metric was analyzed independently to observe the effects of the low-cetane fuels when compared to the baseline. To better understand the effects, a three-tiered normalization strategy was used to provide three different comparisons of the fuels for each metric. Additionally, specific phenomenon regarding the crankshaft twist metrics were investigated. Specifically, the tendency for absolute twist to bias in the direction opposite of crank rotation as with low-cetane fuels at high-speed conditions.

With all metrics analyzed, they were combined in a Composite Durability Indicator to provide a comprehensive determination of wear.

Chapter 2 Literature Review

2.1 Introduction to Synthetic Fuels

Synthetic fuels are chemically synthesized fuels designed to mimic the physical and chemical properties of traditional fossil fuels [1] [2][4][5]. It is difficult to establish exclusive groups for synthetic fuels, as they can vary in production process, feedstock, application, sustainability, and chemical composition. However, generally, synthetic fuels are grouped based upon the feedstock used. This results in four groups of fuels, biofuels, hydrogen fuels, power-to-liquid (PtL) fuels, and gas-to-liquid (GtL) fuels [1].

While a range of synthesis methods exist, the Fischer–Tropsch process remains the most established for producing aviation-grade hydrocarbons due to its flexibility in feedstocks and high-quality fuel output [1].

2.2 Production of Synthetic Fuels with Fischer-Tropsch Process

Synthetic fuels were first developed in Germany by Friedrich Bergius in the early 20th century, and later the process was improved on with the well-known Fischer-Tropsch process, developed in 1925 by Franz Fischer and Hans Tropsch [6]. The FT process can be used to produce variety of liquid hydrocarbons, such as gasoline, diesel, and jet fuel, through a chemical reaction with hydrogen and carbon monoxide, utilizing variety of feedstocks, including natural gas, coal, syngas, or biomass [7][8]. The FT process uses a catalyst, typically iron or cobalt, to facilitate the reaction between hydrogen and carbon monoxide in a high temperature and pressure reactor [9]. The liquid hydrocarbon and molecular structure produced depends on the specific conditions used. Figure 1 below illustrates the FT process with the input being syngas with Equation 1 above it being the overall equation for the FT process [1], where n is the number of carbon atoms in the resulting hydrocarbon.

$$nH_2 + nCO \rightarrow C_nH_{(2n+2)} + nH_2O \qquad [1]$$

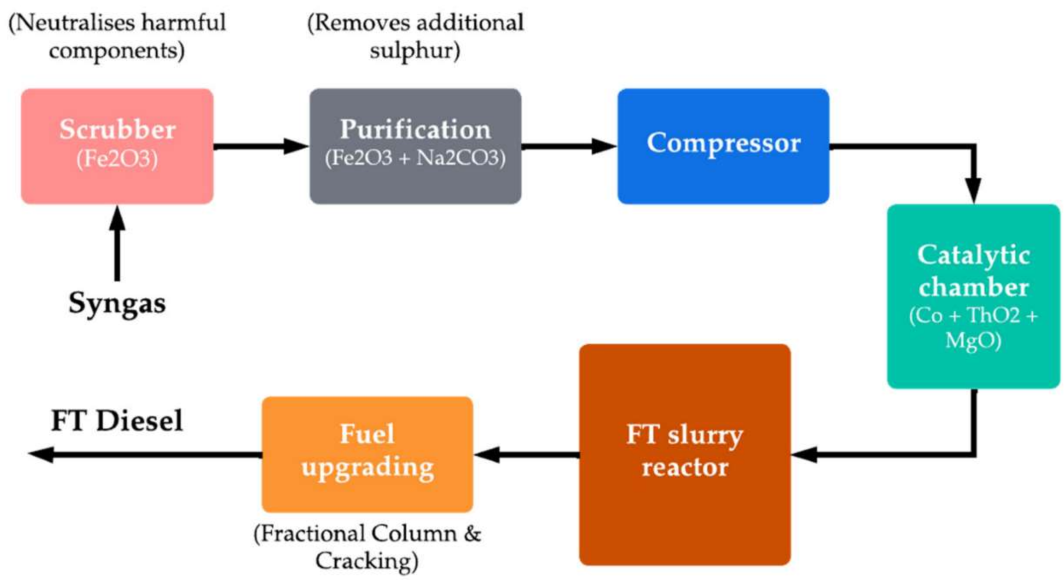

Figure 1: Typical FT Process for FT Diesel Production from Syngas [1]

Synthetic fuels can reduce both the emissions of compression ignition engines and the dependence on fossil fuels [10]. Specifically, synthetic fuels significantly reduce sulfur as a byproduct of combustion, when compared to conventional diesel fuel. The sulfur content can vary based on the feedstock used [10][11]. This has led to synthetic fuels being a very attractive option for alternative fuels.

2.3 Sustainable Aviation Fuels

Aviation accounts for 2% of all carbon dioxide (CO_2) emissions and 12% of CO_2 emissions from transportation. The International Civil Aviation Organization's Carbon Offsetting and Reduction Scheme for International Aviation (CORSIA) has regulated net CO_2 aviation emissions to 2020 levels through 2035. Additionally, the international aviation industry has set a goal of reaching net-zero carbon emissions by 2050 [12]. To reach these goals, more emission-compliant fuels will need to be produced and used for general aviation.

Sustainable aviation fuel (SAF) is a synthetic fuel made from non-petroleum feedstocks and are vital for reducing the emissions of air transportation. SAFs are a reasonable replacement for conventional jet fuels as they can be blended and used in existing aircraft and infrastructure. Limitations exist for the blending of SAFs with conventional jet fuels at a variety of levels, ranging from 10% to 50%, depending on the feedstock [12].

2.3.1 Alcohol-to-Jet SAF

With the push for more sustainable aviation fuels, Alcohol-to-Jet (ATJ) has emerged as a promising alternative. The current most common type of SAF uses hydro processed esters and fatty acids (HEFA), such as used cooking oils, as the feedstock. However, even at full capacity, HEFA-derived fuels could only meet 13% of the current demand for jet fuel [13]. With demand expected to increase, an alternative will be needed and ATJ is already filling that gap worldwide. Advantages of ATJ include the variety of feedstock pathways and the ability to be blended with conventional jet fuel up to 50%, matching the amount HEFA-derived fuels may be blended [12]

ATJ's multiple feedstocks are commonly cellulosic biomass based. For the US and India, agricultural waste and crop ethanol may be used, while Europe is limited to strictly agricultural waste as restrictions prevent the use of crop-based ethanol. The ATJ process, certified under the ASTM D7566 Annex A5 pathway, transforms ethanol from these feedstocks into high-purity synthetic paraffinic kerosene (SPK), which can be blended with conventional jet fuels. This process is similar to that for traditional fossil fuels, including steps such as dehydration, oligomerization, hydrogenation, and fractionation, and is shown in Figure 2 below. During fractionation, the mixture of hydrocarbons is separated, SPK and synthetic paraffinic diesel (SPD) [14].

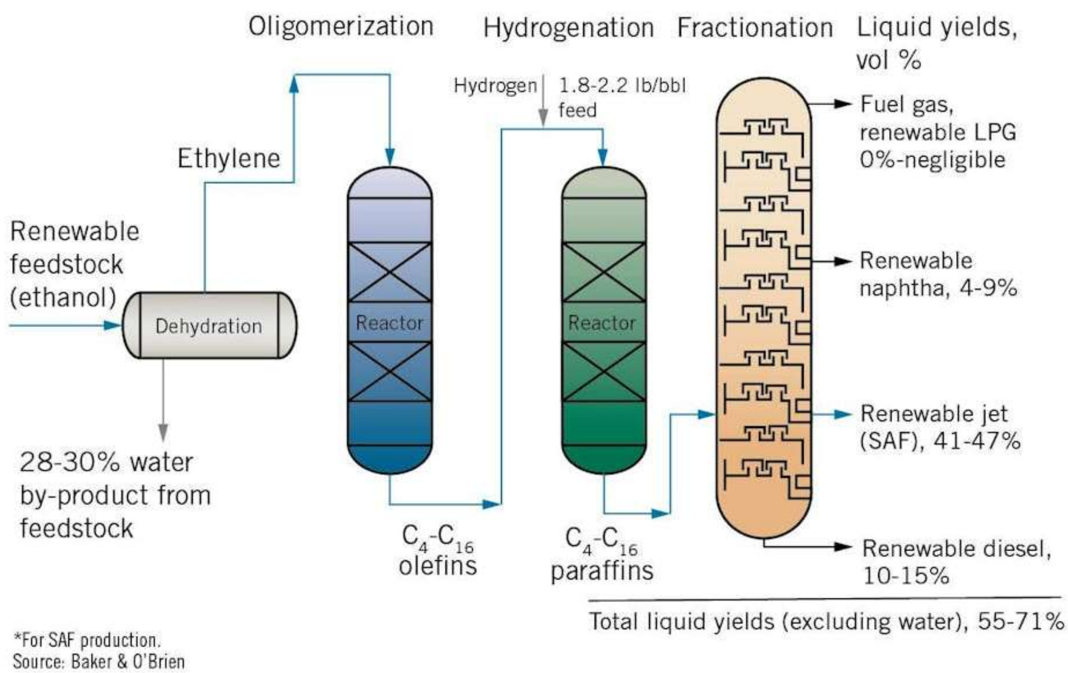

Figure 2: Simplified ATJ Process-flow Diagram for SAF [15]

2.4 Implications for Engine Performance with Use of Synthetic Fuels

Other characteristics of synthetic fuels, beyond sulfur content, can differ from conventional fuels and can be dependent on the feedstock from which the fuel is synthesized. These characteristics include cetane number, flash point, oxidative stability, cloud point, and heat content [16]. A reduction in the cetane number of the fuel in particular has been found to affect combustion performance in compression ignition engines, as the cetane number measures the ignition quality of a fuel [17][19][20][21]. The cetane number of a fuel is dictated by and proportional to the carbon chain length of the alkanes present in the fuel [11]. Therefore, longer carbon chain length results in a lower cetane number, lowering the propensity for the fuel to auto ignite [22].

As stated earlier, the cetane number of the fuel synthesized depends on the feedstock used. Since the resulting fuels vary in carbon chain length, this results in synthetic fuels with cetane numbers both greater and less than conventional fuel. The main limitation of ATJ is the considerably low derived cetane number of ~15 [3][52]. This rating is significantly less than is acceptable, guided by the MIL-DTL-83133 fuel specification for JP-8 which specifies that finished fuels consisting of conventional and synthetic jet fuels blends have a minimum derived cetane number (DCN) of 40 [23].

2.4.1 Ignition delay

Ignition delay is defined as the time lag between the start of injection of the fuel and the beginning of the combustion of the fuel. As expected, since low-cetane fuels have a lower propensity to combust, low-cetane fuels have been found to increase the ignition delay when used, specifically at low to medium load conditions [17][20][24]. This ignition delay was also found to cause a misfire condition at low speed and low load conditions [17]. Misfiring was found to be more prevalent when the engine was not fully warmed up and the ignition delay increased non-linearly as cetane numbers were reduced, increasing significantly for cetane numbers below 35 [24].

2.4.2 Ramifications of Ignition Delay

Ignition delay affects many metrics, either directly or indirectly, that themselves may accelerate wear depending on the extent of the change. This section will first discuss how ignition delay leads to an increase in the variance of both peak pressure and peak pressure rise rate. Additionally, it will be explored how increases in peak pressure and peak pressure rise rate themselves cause increased wear. Furthermore, it will be discussed how increases in peak pressure and peak pressure rise rate themselves excite other secondary wear causing events. Specifically, increases in crankshaft twist, both absolute and peak-to-peak, as well as the rate of crankshaft twist will be investigated.

Due to the ignition delay of low-cetane fuels, the pressure within the cylinder is affected, specifically maximum cylinder pressure and the variance in cylinder pressure increase due to ignition delay. For low-cetane fuels with long ignition delays, most of the fuel is injected before ignition begins, resulting in a large pressure rise rate due to the greater combustion rate. This ultimately increases the maximum pressure within the cylinder [24]. Regarding reductions in cylinder pressure, causing the increase in the variance, this can occur for cases with exceptionally large ignition delays. If the fuel begins to combust near or after top dead center, the expansion caused by the downward movement of the piston and subsequent cooling leads to incomplete combustion. For more extreme cases, the pressure and temperature within the cylinder may reduce to the extent that ignition will not occur at all, leading to a misfire [24].

As discussed previously, depending on the extent of ignition delay increases due to low-cetane fuels, peak cylinder pressure may increase or decrease. For the purpose of determining durability concerns, the effects of increases in peak cylinder pressure will be discussed. As peak cylinder pressure increases, the temperature within the cylinder will increase, as dictated by Gay-Lussac's law [34]. This increase in pressure and temperature within the cylinder were found to accelerate cylinder head cracking, specifically in the valve bridge region [29][30]. Additionally, increases in cylinder pressure were found to increase the maximum film pressure for piston rings, as well as the asperity contact force between the piston rings and cylinder wall [31]. Both of which may lead to scuffing of the cylinder wall. As previously discussed, an increase in peak pressure due to a longer ignition delay is generally accompanied by an increase in pressure rise rate [24]. Increases in pressure rise rate have been found to increase engine vibration as well as piston slap [35]. In addition, excessive piston slap and the resulting cylinder liner vibration has been found to cause cavitation in diesel engines with wet cylinder liner configurations[35][37][38][39].

Continuing with the secondary effects of ignition delay, increases in both peak pressure and pressure rise rate were found to increase crankshaft torsion [40], which has been thoroughly studied for the purpose of mitigating it [41][42][43]. This is because crankshaft torsion, along with crankshaft bending, having been found to be the main causes of fatigue failure in crankshafts [44][45][48]. More specifically, models for determining fatigue life of crankshafts effectively model real conditions when incorporating both the maximum torsional stress and cyclic torsional strain range [46][47]. Crankshaft torsion is not constant for all engine speeds and, as expected, increases as the torsional vibration of the crankshaft approaches the resonant frequency of the crankshaft [27][50]. The rate at which the crankshaft twists, specifically strain rate, is not necessarily relevant for the durability of the crankshaft in a stress inducing sense. For this work, only elastic deformation is expected and due to Hooke's law [49], stress amplitude is only dependent on strain amplitude, not strain rate, under elastic deformation. However, rate of crankshaft twist helps to determine vibration intensity in the crankshaft, which is amplified at the resonant frequency [50].

2.5 Methods for Mitigation of Low-Cetane Effects on Combustion

As synthetic fuels with varying cetane ratings become more prevalent, extensive research has been conducted to understand low-cetane fuel behavior and determine methods to combat the effects [17][18][19][20][24][25].

Beginning with the simplest method, blending low-cetane fuel with higher cetane fuels was found to be quite effective. With a 25-75 blend of JP-8 jet fuel and low-cetane synthetic fuels adequately alleviating a majority of low-cetane effects at all high, medium, and some light load conditions, and a 50-50 blend reasonably alleviating all ignition concerns [17]. This method effectively increases the cetane rating of the fuel, preventing it from inducing low-cetane combustion effects. This strategy may be ideal for older engines that may be difficult to adjust injection timing, injection amount, or the number of injections on.

For a more involved method, it has been found that a close-coupled pilot (CCP) injection can be used to reduce the effects of low-cetane fuels. With proper injection pressure, injection timing, and CCP parameters, the ignition delay tendencies of a low-cetane fuel were effectively mitigated, helping to reshape the heat release profile to mimic that of a higher cetane fuel. The optimized strategy to achieve this outcome involved adjusting the CCP injection to help match the start of combustion and premixed peak of higher cetane fuels, while appropriately delaying the main injection event to match the CA50 timing of higher cetane fuels. This strategy was effective in achieving similar combustion metrics of a DCN 42 fuel with a DCN 31 fuel [25].

Chapter 3 Experimental Setup

3.1 Testing Objectives

The objective of this research is to identify concerning engine operating points when using low-cetane fuels in a representative Army engine under relevant operating conditions. Metrics used to evaluate these conditions and determine areas of concern include combustion parameters such as pressure rise rate, peak pressure, as well as crankshaft twist metrics such as crankshaft twist angle, absolute and peak-to-peak, as well as the rate of crankshaft twist. These selections are determined to be indicators of wear as guided by the conclusions reached in previous literature, discussed in section 2.4.2. Although the rate of crankshaft twist is not expected to cause durability concerns for the crankshaft, considering deformations are only within the elastic range, it is included due to its ability to communicate the violence of combustion and its effects on engine components.

3.2 Engine Selection

The Cummins V903 engine was selected as a representative engine. Engine parameters are shown in Table 1 below.

Table 1: V903 Engine Parameters

Type	4-stroke; 90° V; 8-cylinder
Aspiration	Turbocharge & Aftercooled
Bore & Stroke - in. (mm)	5.50 (140) x 4.75 (121)
Displacement – in^3 (liter)	903 (14.8)
Compression Ratio	15.5: 1
Injection System	MUI, electronically controlled supply pressure

The Cummins V903 was selected as a representative engine due to its use in numerous vehicles for the Army and its numerous characteristics that make it not ideal for use with low-cetane fuels. Specifically, lack of feedback control with a MUI, single injection event, relatively low injection pressure, start of injection is fixed based on engine load, and end of injection time is fixed by a camshaft. Additionally, this engine utilizes stepped timing control for injection. In addition to adjusting injection timing according to the speed and load, all injection timing at low-speed, low-load conditions are shifted in the advanced direction when compared to high-speed, high-load conditions, illustrated in The transition between this relatively advanced to relatively retarded shift is abrupt, taken in one step rather than gradually increasing. This results in conditions just prior to the step timing to have excessive and audible knock, which drastically reduces immediately after the step. All these qualities limit the ability to apply the methods for mitigating low-cetane effects, discussed in section 2.5 Additionally, this engine has the ability to make the same power rating on a variety of fuels, regardless of volumetric energy density. This engine was identical to production engines besides ports for each cylinder within the cylinder heads to allow for cylinder pressure measurement.

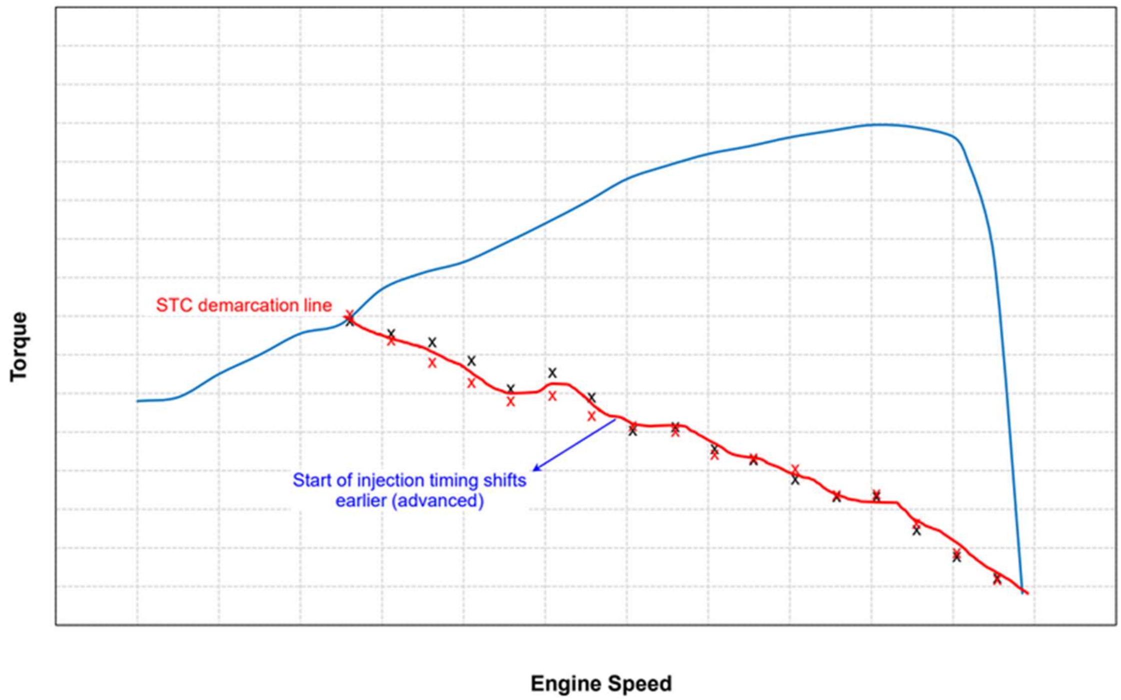

Figure 3: Step Timing Control [52]

3.3 Fuels

Three fuels were evaluated throughout testing: Fuel A, Fuel B, and Fuel C, with derived cetane numbers of 43.7, 34.8, and 29.8 respectively. Fuel A was sourced from Alon USA, Big Spring, TX, and blended with ATJ-8 to produce Fuel B and C. More parameters can be found in Table 2 below.

Table 2: Fuel Properties

Property	Units	Fuel A	Fuel B	Fuel C
Derived Cetane Number (DCN) - ASTM D6890	-	43.7	34.8	29.8
Cetane Index - ASTM D976	-	44.2	44.2	47.1
Jet A: ATJ-8	Vol %	100%: 0%	65.4%: 34.6%	40%: 60%
Aromatics	Vol %	13.9	12.5	8.9
Density (15°C)	kg/m^3	837.7	783.7	775.0
Volumetric Energy Density	MJ/L	53.2	56.2	56.2
Total Sulfur Content	ppm	27	39	27
Kinematic Viscosity (40°C)	mm^2/s	1.47	1.17	1.25

3.4 Test points

Each fuel was evaluated at a total of 19 operating points, including 18 steady state operating points ranging in speed from 800 to 2800 rpm and load from 0% to 100% as well as a full-load, 800 to 2800 rpm sweep. This range of operating points was chosen to provide sufficient detail when observing broad trends. Insufficient data was captured to determine crankshaft twist metrics for Fuel C, this is discussed further in section 5.1.

3.5 Data acquisition

High-speed and low-speed data were collected to evaluate combustion and crankshaft twist metrics. Most measurements were conducted at steady-state conditions with a five-minute stabilization period prior to data acquisition. A diagram of the high-speed data acquisition setup is provided in Figure 4.

3.5.1 High-Speed Data

High-speed data was captured with the use of a Kistler Kibox Type 2893. Four cylinders, cylinders 2, 3, 5, and 8, were instrumented with pressure transducers which were read with Kistler Type 5064C charge amplifiers in the Kibox. The intake manifold was also instrumented with two pressure transducers for the purpose of cylinder pressure pegging. Additionally, a Kistler shaft encoder, Type 2614DK, set with a resolution of 0.1 CA was attached to the front of the crankshaft. Furthermore, a magnetic pickup encoder was attached to the flywheel and read through a Siemens data acquisition system. The front encoder signal was also fed to the Siemens data acquisition system for the sake of synchronizing the data from both encoders.

3.5.2 Low-Speed Data

Low-speed data such as additional intake pressure measurements, temperatures, flow rates, engine speed, and engine torque were read through a NI VeriStand data acquisition system.

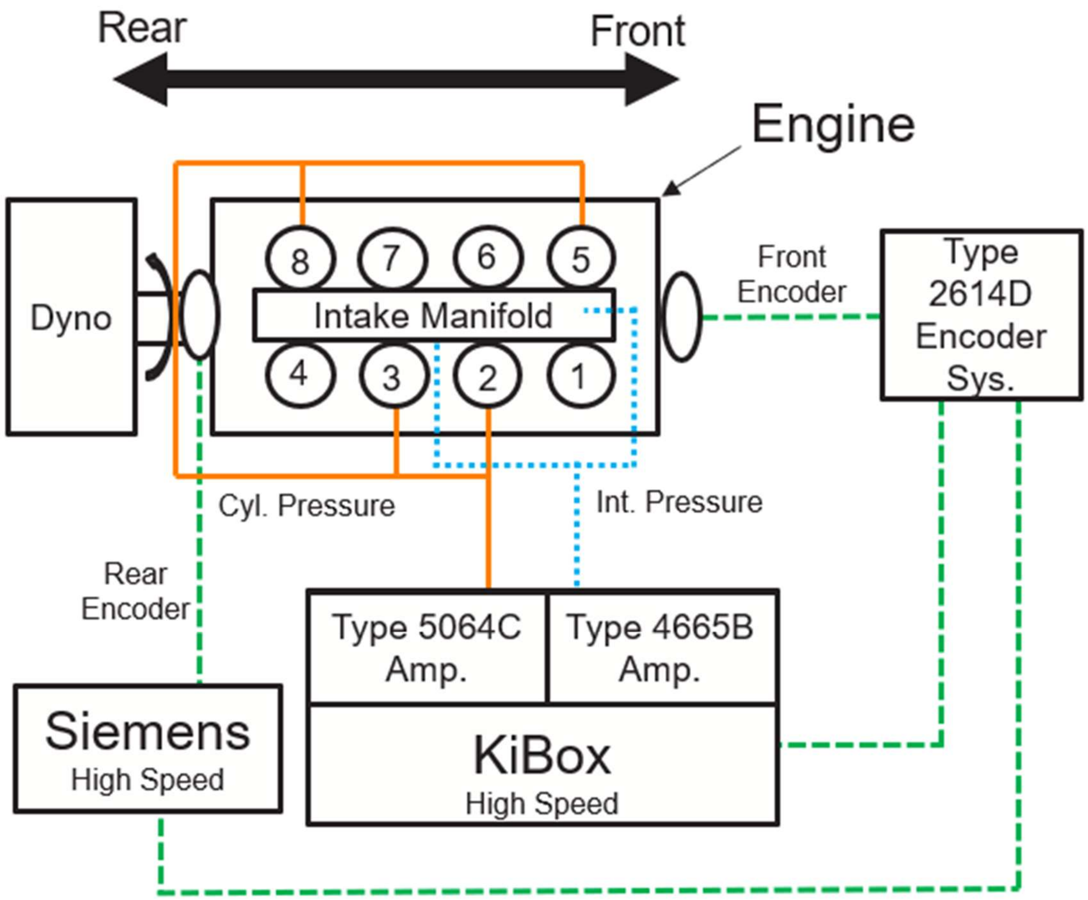

Figure 4: High-Speed Data Acquisition Setup

Chapter 4 Combustion Metrics

4.1 Introduction for All Results

This section provides a roadmap for the results, which are presented across Chapters 4, 5, and 6. Chapter 4 addresses combustion metrics, Chapter 5 covers crankshaft twist, and Chapter 6 synthesizes these results into a Composite Durability Indicator to determine the most concerning conditions. Each section will be analyzed through the lens of durability, accordingly, a ‘concerning’ case is one that is expected to result in accelerated wear or damage to engine components, as discussed in section 2.4.2. To determine concerning cases, three normalization methods will be employed for each metric; (1) metric normalized to the maximum value for each respective fuel, (2) metric normalized to the corresponding Fuel A value on a case-by-case basis, and (3) metric normalized to the maximum Fuel A value across all conditions. These normalizations were selected to highlight different aspects of low-cetane effects. Values obtained from the third method will also be used in the Composite Durability Indicator. Descriptions, analytical purposes, and example insights are provided in Table 3 below. This three-tiered analysis will be consistent with all metrics analyzed. Regarding presentation, intra-fuel normalization is intentionally on a blue scale to not mistakenly convey concerns, merely trends. However, inter-fuel relative and global normalization methods are displayed on a scale from green to red, intuitively displaying least concerning and most concerning cases respectively.

Table 3: Normalization Methods Utilized Throughout Results

Method	Description	Analytical Purpose	Example Insight
Intra-Fuel Normalization	Each data point is normalized to the absolute maximum values recorded for that same fuel	To isolate and compare the fundamental trends	Confirms that peak pressure is correlated with load for all fuels, regardless of cetane rating
Inter-Fuel Relative Normalization	Data points are normalized to the values of Fuel A at the exact same operating conditions	To quantify the relative deviation from the Fuel A	Shows that peak pressures with Fuel are affected by cetane rating across all conditions, maximally at low speeds
Inter-Fuel Global Normalization	Each data point is normalized to the single absolute maximum value observed in Fuel A across all points	To determine if a change in cetane rating creates a new "worst-case" scenario that exceeds the baseline's known maximum and provide perspective	Although Fuel C pressures increase everywhere, they only surpass Fuel A's overall maximum at high speed and load conditions

4.2 Combustion Metrics Overview

This chapter discusses the ignition delay, cylinder pressure, and cylinder pressure rise rate observed across all fuels tested. Ignition delay is discussed to display that low-cetane fuel effects are present, while cylinder pressure and cylinder pressure rise rate are discussed due to their effects on durability, discussed in section 2.4.2. Methods for processing data and performing the relevant calculations are also presented.

4.3 Ignition Delay

As discussed previously, lower cetane fuels are known to increase ignition delay. The ignition delay for each fuel was determined with methods described in the following section, with results presented later. The results presented are intended solely to demonstrate the presence of low-cetane fuel effects and to support the subsequent analysis used to assess the durability implications of low-cetane fuel. Results are presented as ignition delay with respect to crank position as well as ignition delay with respect to time.

4.3.1 Ignition Delay Determination

To obtain an ignition delay value, inherently, start of injection (SOI) and start of combustion (SOC) must be determined. Typically, SOI is given through means of recording the SOI command to the injector or placement of a strain gauge on the injector rocker arm for electronic or mechanical injections respectively. For this research, neither of these methods were employed and subsequently, SOI must be determined from collected data. Specifically, SOI was determined with the use of the apparent heat release rate (AHRR) trace with an example presented in Figure 5. AHRR was calculated using single-zone analysis, shown in [2 below, with n, P, V, and θ being the polytropic index, pressure, cylinder volume, and crank angle respectively. The pressure used was processed with the method shown in section 4.4.1. Additionally, the volume was calculated using an adjusted compression ratio (CR) value. This adjusted CR value of 14.5 was chosen due it providing a more linear increase of pressure with respect to volume during the compression stroke of the logarithm pressure versus volume plot compared to the original CR value of 15.5.

$$AHRR = \frac{n}{n-1} P \frac{dV}{d\theta} + \frac{1}{n-1} V \frac{dP}{d\theta} \qquad [2]$$

Equation 2 above was numerically implemented to determine the apparent heat release rate for each cycle. The value of n for each cycle was determined with a linear regression of the logarithm of processed pressure versus the logarithm of volume trace with pressure and volume values from -45° CA up to -20° CA. A relatively smaller window was chosen to provide a more accurate n value for the region of interest, that being near TDC. Considering that during polytropic compression the value of n is not constant, as it accounts for heat transfer, fitting to a CA region closer to the region of interest will provide a more accurate value. This provided an AHRR trace such as shown below.

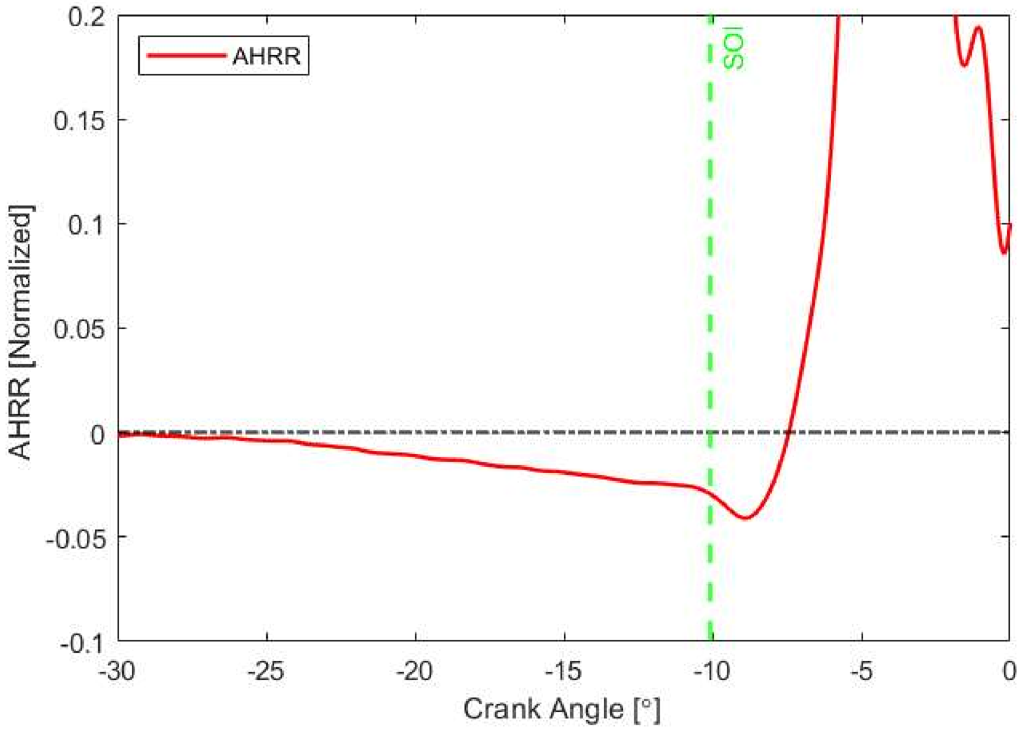

Figure 5: SOI Determination with AHRR, Fuel A at 800 rpm, 0% Load

SOI was designated as the first noticeable deviation from the constant negative slope the AHRR during compression. This reduction in slope signifies the absorption of heat due to the evaporative cooling effect of the injected fuel. This method was utilized for all cases and provided consistent results when comparing identical operating conditions across all three fuels.

Following SOI determination, the SOC was determined. Considering there are many methods for determining start of combustion (SOC) and subsequently ignition delay for a CI engines, ranging from the maxima of the second or third derivatives of cylinder pressure with respect to crank angle or the zero crossing point (from negative to positive) of the AHRR [32], it is important to clearly state the method used for SOC determination. In this thesis, SOC was determined with the use of a modified version of the pressure recovery method proposed by Groendyk and Rothamer [32]. The pressure recovery method was chosen due to its robustness and resilience to in-cylinder pressure oscillations which are common with low-cetane fuels. Additionally, this method does not require the use of the second or third derivative of cylinder pressure, which may be significantly affected by the filtering method. Modifications to the original pressure recovery method will be discussed later.

To begin SOC determination with the modified pressure recovery method, an accurate reference motored pressure trace was calculated. The reference motored pressure trace used for each case was approximated as a polytropic process with Equation 3 below. Pressure values used were processed with the method provided in 4.4.1 and volume values were calculated with the adjusted CR value, discussed previously.

$$PV^n = Constant \qquad [3]$$

The exponent, n, is the polytropic exponent or polytropic index [51], and was determined with a linear regression of the logarithm of pressure versus the logarithm of volume trace. Again, pressure and volume values from -45° CA up to -20° CA were used and provided close agreement in the desired regions. Temporarily, the motored trace was fit to pressure and volume values from -110° CA to -20° CA to observe how the fitting region affected SOC determination, and it was found that SOC remained consistent when fitting to either region. This can be seen in Figure 6 below. Presented are identical cases, only differing in the region from which the motored pressure was fit.

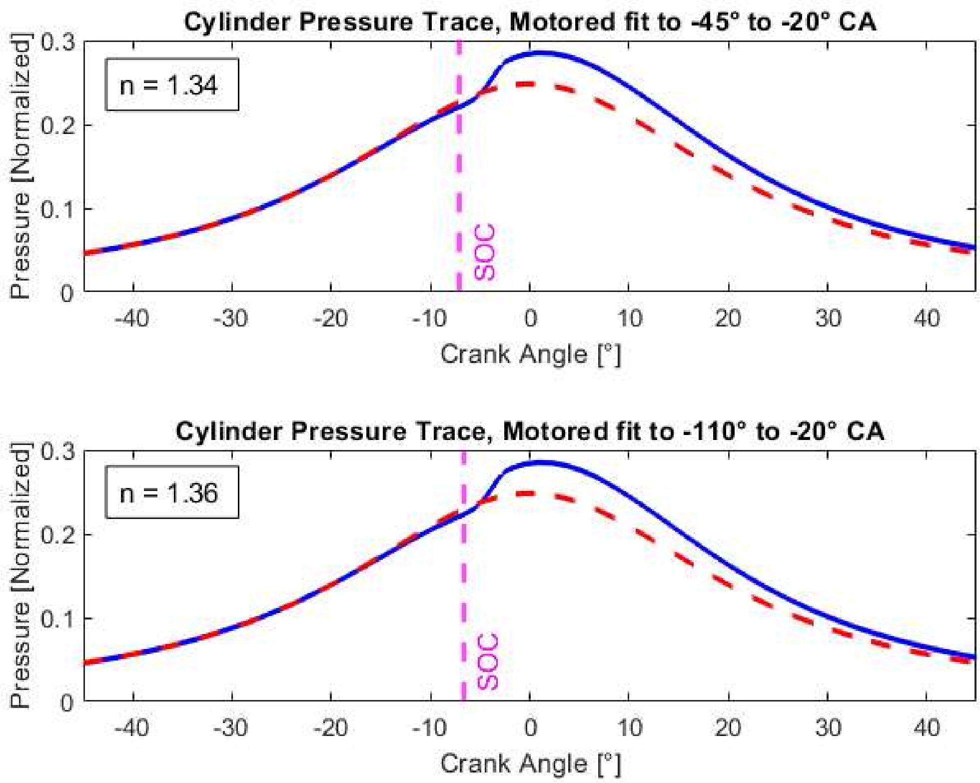

Figure 6: Comparison of Motored Pressure Fit Regions, Fuel A at 800 rpm, 0% Load

For the motored pressure trace fit from -110° CA to -20° CA, shown on the bottom, the measured pressure dips below the motored pressure much earlier than the -45° CA to -20° CA fit. This is not necessarily obvious, however, the change in calculated n shows there is a difference. The cause for this discrepancy is identical to the reasoning provided previously when discussing the AHRR calculation and obtaining an accurate n value. Considering that during polytropic compression the value of n is not constant, differing results from the two fitting regions are due to -45° CA to -20° CA providing a more accurate γ value for near SOI and SOC events when compared to the γ determined from -110° CA to -20° CA. Accordingly, the region of fit was kept narrow at -45° CA to

20° CA and provided consistent and reasonable results when comparing the three fuels, as seen later in Figure 9. With an accurate referenced motored pressure calculated, SOC could then be calculated. An illustration of the method used to calculate SOC is provided in Figure 7 below.

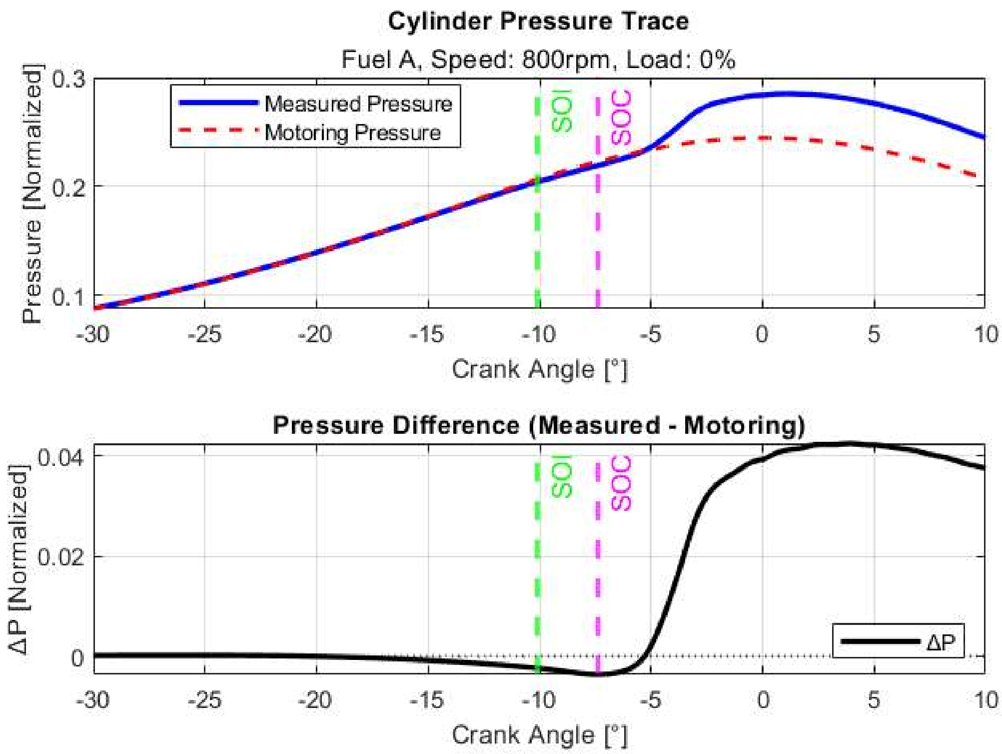

Figure 7: Determination of SOI and SOC with Modified Pressure Recovery Method, Fuel A at 800 rpm, 0% Load

As shown above, to determine SOC, the reference motored pressure was subtracted from the measured cylinder pressure to provide a ΔP curve, shown on the bottom of the figure. As stated previously, the original pressure recovery method's SOC definition was modified. Specifically, start of combustion (SOC) was redefined as the point at which pressure begins to recover rather than the point at which pressure does recover to a referenced motored value, minimum ΔP rather than $\Delta P = 0$. Groendyk and

Rothamer [32] suggest the $\Delta P = 0$ point to signify pressure overcoming the pressure reduction due to evaporative cooling and beginning to rise, indicating energy release due to combustion. However, the data presented shows that the pressure begins to rise before overcoming the reduction in pressure due to evaporative cooling. Of the two parameters, pressure beginning to rise was thought to be a more significant indicator of energy release, compared to pressure recovering. As such, the requirement for pressure to recover was omitted, resulting in the sole indicator of SOC being pressure beginning to rise, minimum ΔP. Using this adjusted method, SOC was first determined in terms of crank angle. This definition was found to closely align with the SOC determined with the AHRR zero crossing point method, another common SOC determination method, as shown in Figure 8 below.

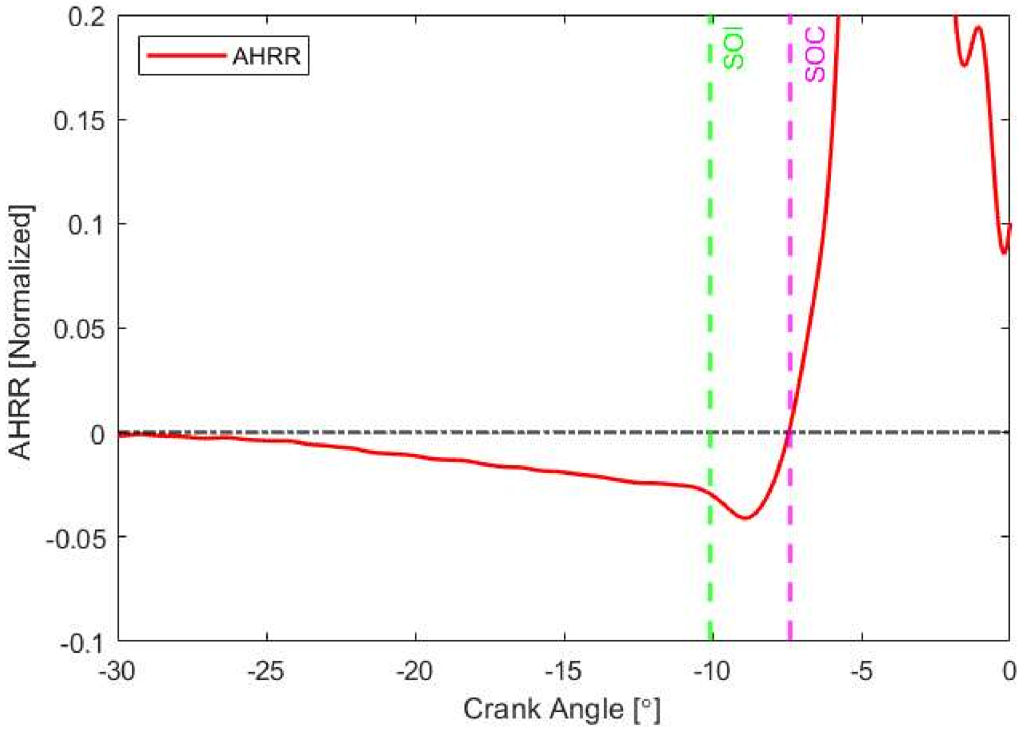

Figure 8: AHRR with SOI and SOC, Fuel A at 800 rpm, 0% Load

In addition to aligning with the AHRR zero-crossing point, SOC results were found to be reasonable when observing pressure traces with the SOI and SOC overlayed. A comparison of pressure traces for the three fuels tested is presented in Figure 9 below.

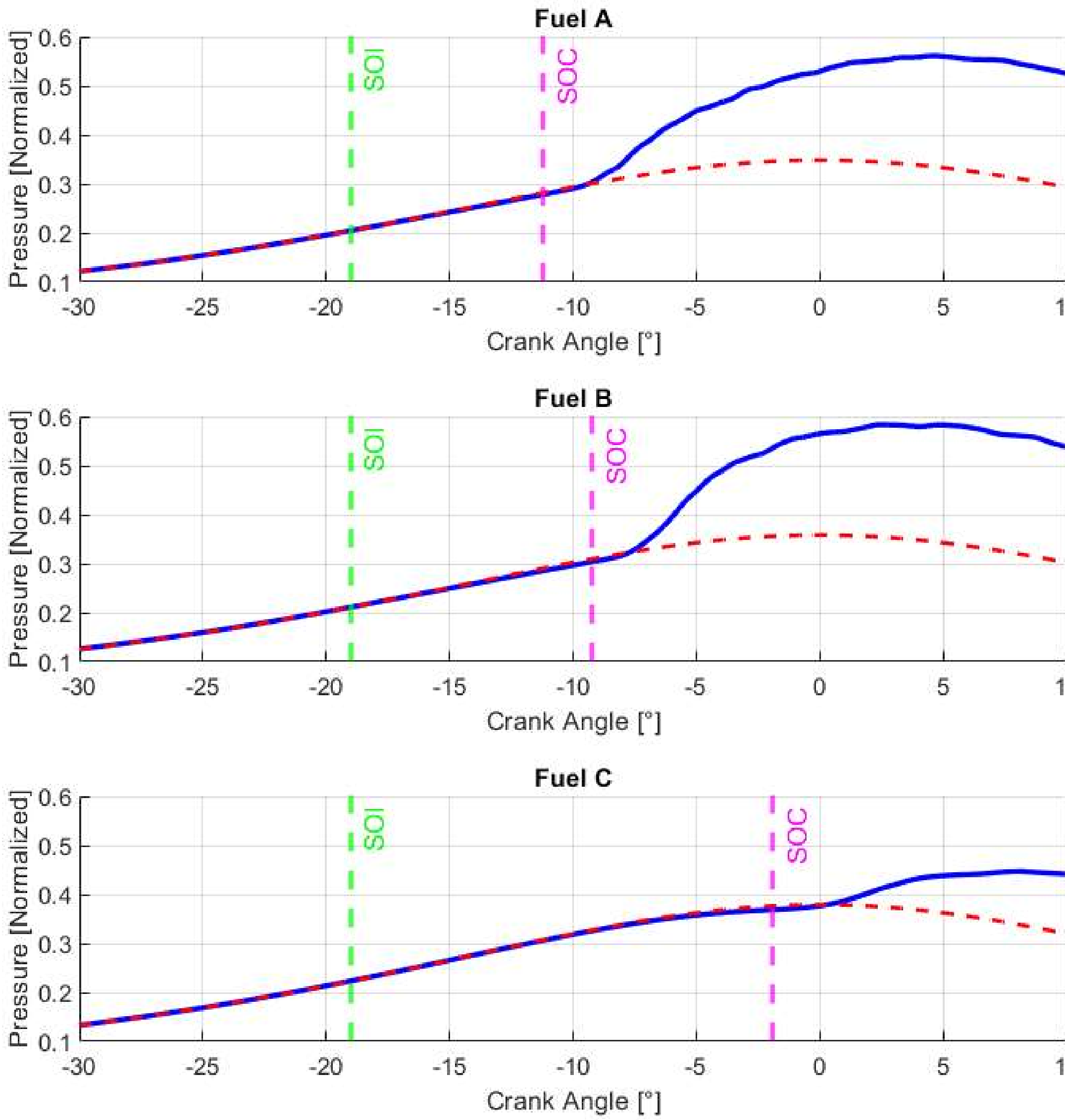

Figure 9: Comparison of Determined SOI and SOC Across Fuels, 2000 rpm, 50% Load, (Blue: Measured Pressure, Red: Motored Pressure)

With SOC and SOI determined for each cycle, the ignition delay in terms of crank angle could be determined by simply subtracting the SOI value from the SOC value. To determine the time ignition delay, the indices of SOI and SOC were used with a calculated time array for each cycle, discussed in the following paragraph, to determine

SOI and SOC occurrences in time. Ignition delay in terms of time could then be calculated by subtracting the SOI time from the SOC time.

To obtain a time array with the same angular resolution as the crank angle encoder (3600 samples per revolution, corresponding to 0.1° CA), the lower-resolution time array provided by the high-speed data acquisition system (360 samples per revolution, time measurement every 1° CA) was interpolated. Interpolation was performed in MATLAB using the built-in interp1 function with piecewise cubic Hermite interpolating polynomial (PCHIP) interpolation, increasing the resolution of the time array from one time measurement per crank angle degree to one measurement per 0.1° CA. This interpolation was done for each cycle to account for fluctuations in engine speed between and throughout cycles.

4.3.2 Ignition Delay Results

Ignition delay values were calculated for all cases. The results presented here are intended solely to demonstrate the presence of low-cetane fuel effects and to support the subsequent analysis used to assess the durability concerns of low-cetane fuel. Ignition delay values will not be used in the Composite Durability Indicator as it is the consequences of ignition delay that affect durability, not necessarily the ignition delay itself. Results are presented using the three normalization methods previously discussed: (1) time and crank angle ignition delay normalized to the maximum value for each respective fuel, (2) time ignition delay normalized to the corresponding Fuel A value on a case-by-case basis, and (3) time ignition delay normalized to the maximum Fuel A value.

Beginning with intra-fuel normalization, results for ignition delay with respect to time are presented below.

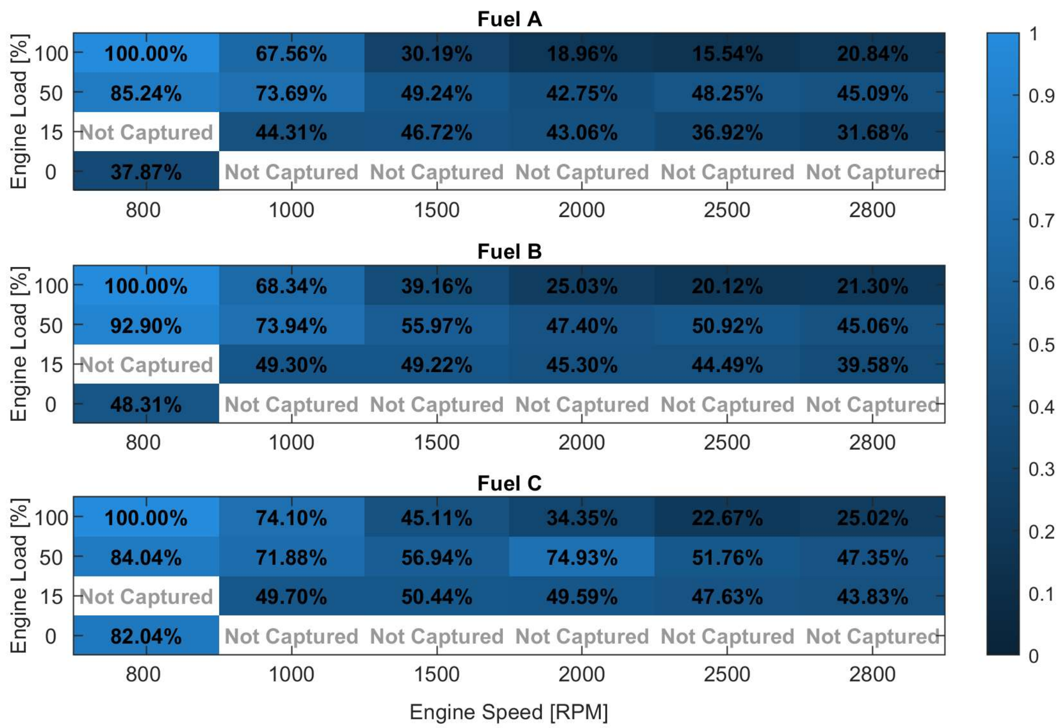

Figure 10: Time Ignition Delay, Normalized to Max. of Respective Fuel

Figure 10 above displays ignition delay values, originally in time (ms), normalized to the maximum value of the respective fuel. As such, values range from 0% to 100%, with dark to light blue cell colors respectively. This is intended to investigate how the trends of ignition delay, specifically the relationship between ignition delay extent and speed and load, change as the cetane rating is lowered. As expected, the time ignition delay is inversely proportional to the engine speed. This is a result of higher engine speeds inherently resulting in less time per cycle. This causes time ignition delay results to be somewhat blurred due to their dependence on engine speed. To remove the time dependency of ignition delay, a similar set of tables is presented in Figure 11 below, except with ignition delay in terms of normalized crank angle delay.

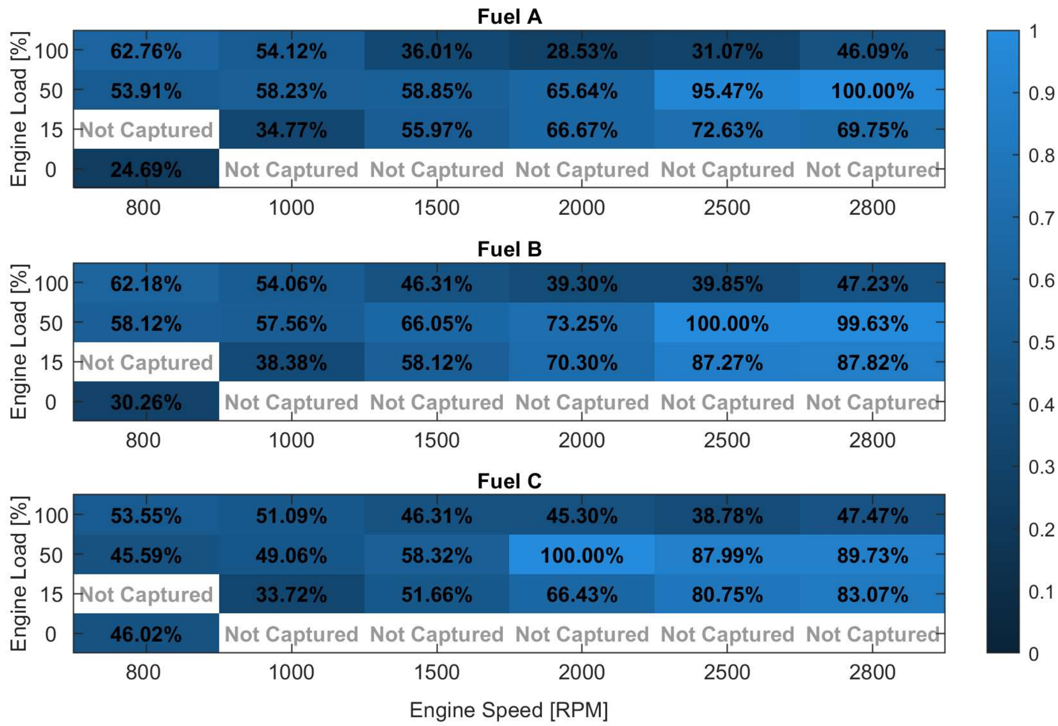

Figure 11:Crank Angle Ignition Delay, Normalize to Max. of Respective Fuel

Figure 11 above is provided to be used in the same manner as Figure 10 previously. That is to see how the relationship between ignition delay and speed and load changes as the cetane rating is lowered. Figure 11 values were originally with respect to crank angle (°) but have been normalized to maximum value of the respective fuel. From both figures, it can be concluded that lowering the cetane rating does not significantly change the relationship of ignition delay with speed and load, for both delays with respect to time or crank angle. That is, the greatest ignition delay in time occurs at low-speed high-load conditions, while the greatest ignition delay with respect to crank angle position occurs at high-speed part-load conditions, regardless of cetane rating. The increase in crank angle ignition delay at high-speed conditions is suspected to be caused by an earlier SOI, not necessarily a later SOC.

Next, changes in values when compared to Fuel A on a case-by-case basis will be investigated. This is intended to communicate what operating conditions present more of a concern when compared to their Fuel A counterparts. First, the change in time ignition delay as cetane rating was lowered will be analyzed, shown below, followed by the change in crank angle ignition delay with a decrease in cetane rating.

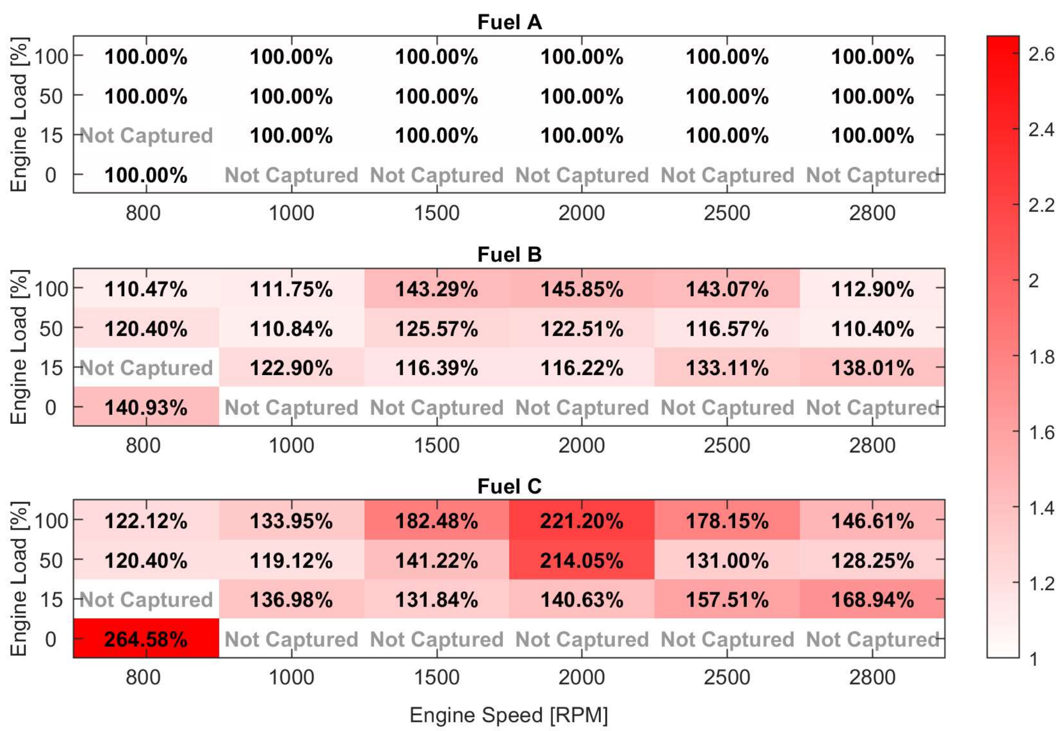

Figure 12: Change in Time Ignition Delay When Compared to Fuel A

Equation 4 defines the normalization procedure for more clarity. This normalizing procedure helps to remove dependence on speed and communicate the greatest changes due to the lowering of cetane rating.

$$Fuel\ B\ \Delta Time\ ID_{Speed(i),Load(j)} = \frac{Fuel\ B\ Time\ ID_{Speed(i),Load(j)}}{Fuel\ A\ Time\ ID_{Speed(i),Load(j)}} \quad [4]$$

Figure 12 above shows the percentage change in time ignition delay for Fuels B and C relative to Fuel A. Percentage values were calculated by normalizing the ignition delay at each engine speed and load condition to the corresponding value for Fuel A, hence, all Fuel A values are 100%. This communicates how time ignition delay is affected across the operating conditions, with darker red indicating values greater than 100% and, if there were any cases fitting the criteria, green would indicate values less than 100% of the Fuel A value. Across all operating conditions, time ignition delay increases as cetane rating is lowered. Interestingly, the greatest increases in time ignition delay, apart from the expected low-speed low-load condition, occur relatively higher speed and load conditions. Specifically, 2000 rpm, 50% and 100% load. These appear to be notable points for only Fuel C although Fuel B changes are slightly elevated in this region.

The effects on crank angle ignition delay are very similar to the effects on time ignition delay, as seen below in Figure 13. Results are expected to be similar as they are inherently measuring the same process.

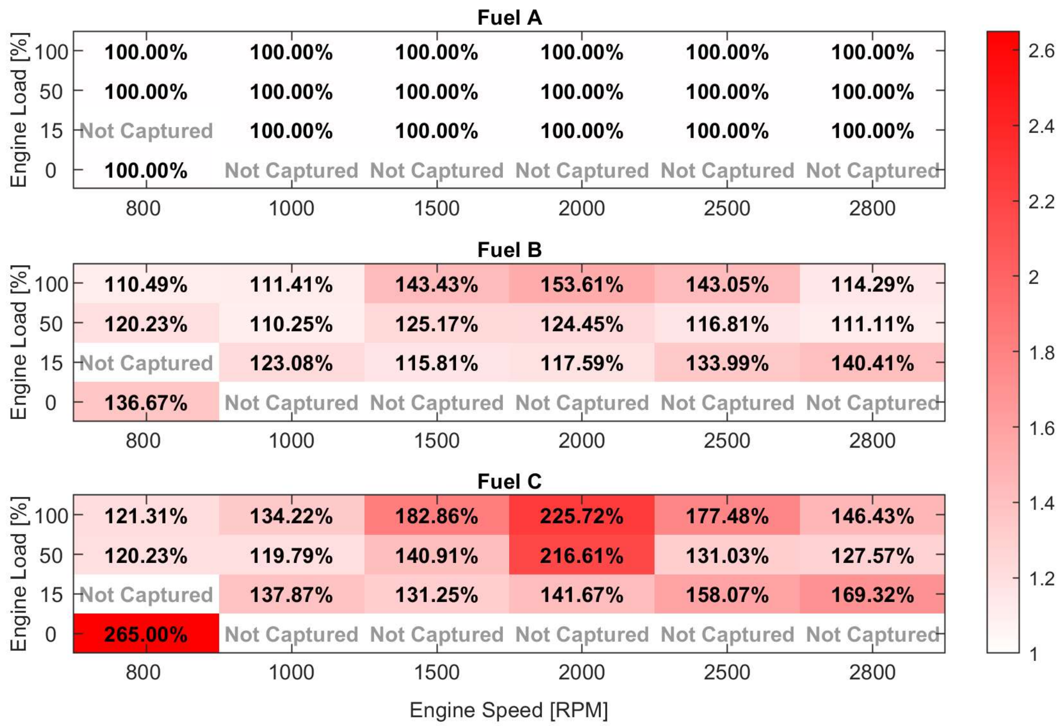

Figure 13: Change in CA Ignition Delay when Compared to Fuel A

From above, the trend of delay increasing across all conditions for crank angle ignition delay is shared as well as the 2000 RPM, 50% and 100% load points of concern for Fuel C. The minimal increase of Fuel B values at high-speed, high-load conditions is somewhat expected as previous research shows that low-cetane effects tend to reduce at these conditions [17][20][24].

Continuing to the next normalization method, Figure 14 and Figure 15 below provide time and crank angle ignition delay values normalized to the respective maximum ignition delay values for Fuel A. This is intended to determine if the changes presented prior are large enough to exceed the global maximum value of Fuel A. This will communicate conditions that present a concern that exceeds that of the maximum concern presented by Fuel A. This method will be more applicable when used later for peak pressure, peak pressure rise rate, and crankshaft twist values.

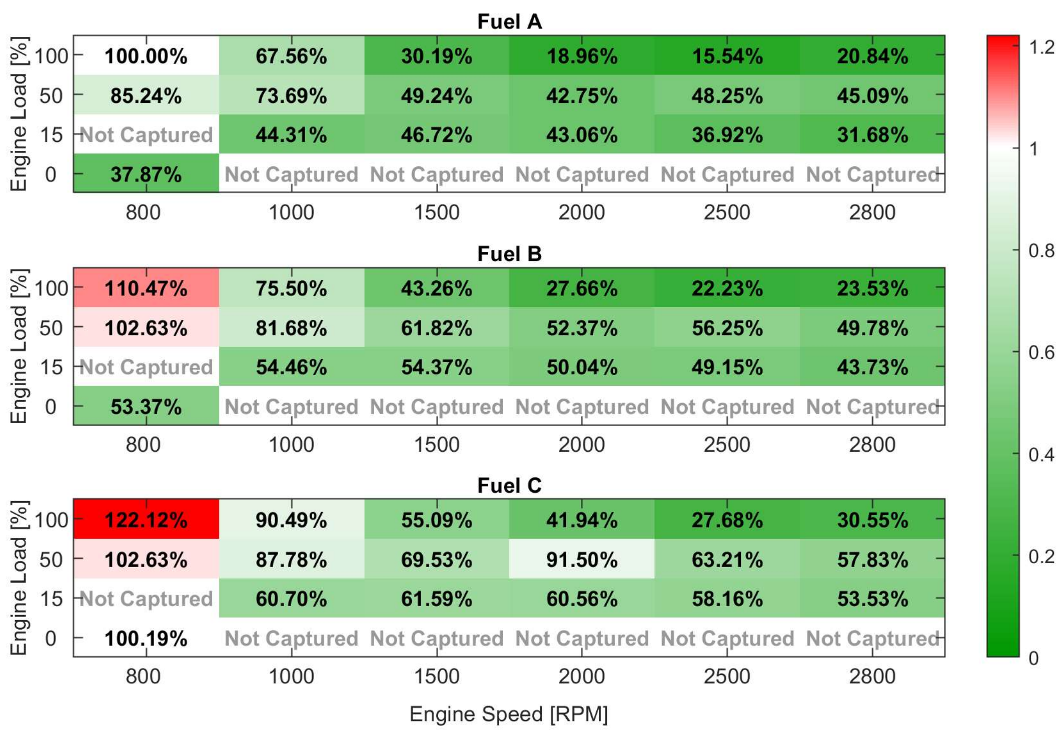

Figure 14: Time Ignition Delay Normalized to Max. Time Ignition Delay of Fuel A

From above, values of time ignition delay only exceed the maximum time ignition delay from Fuel A at the lowest speed and high load condition. This is expected considering trends from Figure 10 show time ignition delay is greatest at this operating point as well as Figure 11 displayed that time ignition delay increased across all operating conditions. Partially removing the dependency on engine speed inherent with time ignition delay by looking at crank angle ignition delay provides Figure 15 below.

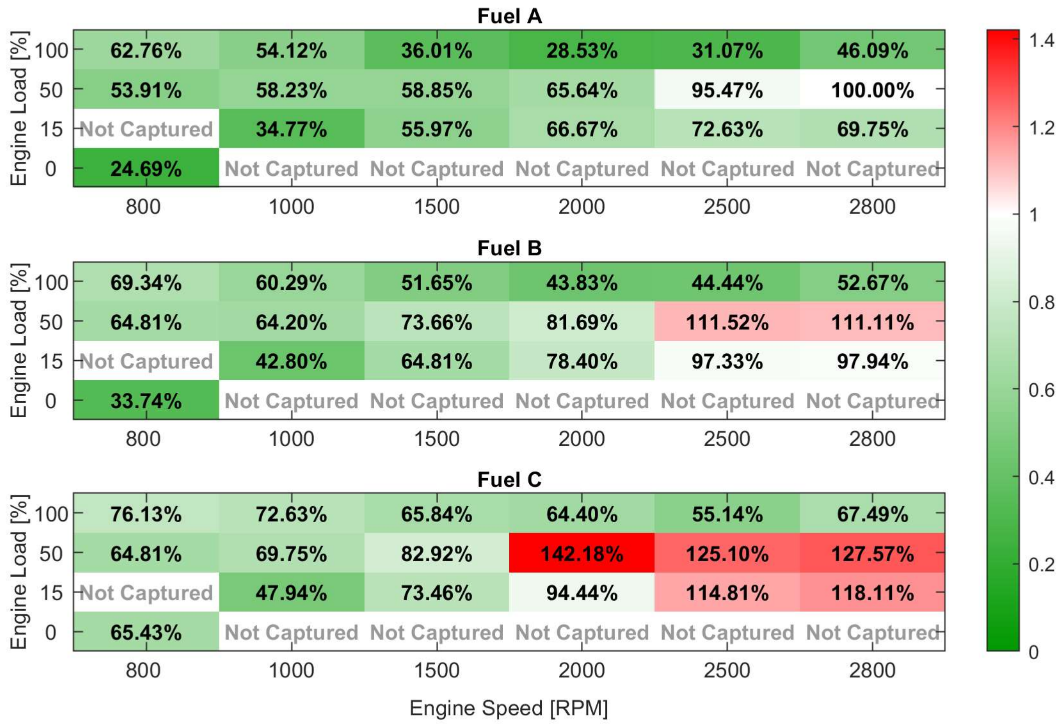

Figure 15: CA Ignition Delay Normalized to Max. CA Ignition Delay of Fuel A

From Figure 15 above, a number of conditions have crank angle ignition delay values that do exceed the maximum crank angle ignition delay present for Fuel A. However, these values are centered around high-speed, low-load conditions, contrary to results from Figure 14. The location of these values is expected considering trends from Figure 11 show crank angle ignition delay is greatest in this region as well as Figure 13 which shows that crank angle ignition delay increases across all operating conditions. Additionally, of the two points of extremely large increases in ignition delay, 2000 rpm at 50% and 100% load, only the 50% load cases exceeds the maximum ignition delay present for all of Fuel A. This suggests that the 2000 rpm, 50% load case presents more of a concern, additionally, it will prove to be notable when analyzing peak pressure and peak pressure rise rate in the following sections.

From the results shown, it is concluded that lowering the cetane rating of the fuel did cause an increase in ignition delay, both with respect to time and crank angle. However, these changes did not change the fundamental relationship of ignition delay with speed and load. Both metrics increased across all operating conditions, but the locations of greatest increase differed. Time ignition delay showed the greatest increase at low speeds while crank angle ignition delay showed the greatest increase at higher speeds. Additionally, Fuel B and C ignition delay values did exceed the global maximum values present for Fuel A at certain conditions. Specifically, 2000 rpm at 50% load displayed excessive ignition delay. With the conclusions regarding how ignition delay is affected, presented above, it can be concluded that an increase in ignition delay, a typical low-cetane effect, is present. Therefore, the following analysis is valid for determining the effects of low-cetane fuels on other metrics.

4.4 Cylinder Pressure

Cylinder pressures were collected from four of the eight cylinders, specifically cylinders 2, 3, 5, and 8. This section will discuss the processing methods as well as notable results with regards to low-cetane effects.

4.4.1 Cylinder Pressure Processing

Cylinder pressures were collected from four cylinders and processed to be used in analysis. This section will discuss the pegging and filtering methods utilized.

Cylinder pressures were pegged using the thermodynamic pegging method in the KiBox software during cylinder pressure data acquisition. Additionally, the crank angle offset was adjusted such that the logarithm of cylinder pressure versus the logarithm of cylinder volume curve, measured during a hot motoring condition, exhibited a sharp cusp at TDC, indicating correct TDC phasing.

As the filtering method used will significantly affect the observed cylinder pressure and pressure rise rate discussed in the subsequent section, it is essential to include the filtering method employed. All cylinder pressure data was filtered using a Butterworth low-pass filter with a cutoff frequency of 4000 Hz and an order of four, applied using zero-phase forward-backward filtering. It should be noted that a forward-backward filtering effectively doubles the filtering order, resulting in 8th order filtering. A Butterworth filter was selected due to its maximally flat frequency response in the passband. This results in uniform attenuation across the passband prior to the cutoff frequency and minimizing induced ripple from the filtering method. The cutoff frequency was iteratively determined by visually comparing raw and filtered pressure traces to ensure that the overall shape, peak pressure magnitude, and timing of the pressure trace were preserved. A cutoff frequency of 4000 Hz was found to sufficiently attenuate high-frequency oscillations, primarily associated with pressure transducer dynamics and mechanical vibrations, while retaining the characteristic features of the combustion pressure trace.

4.4.2 Cylinder Pressure Results

As with every metric discussed in the following sections, cylinder pressure results will be analyzed through a lens of durability. Accordingly, the average peak pressure will be the main discussion of this section. Values shown represent the average peak pressure observed across all cycles recorded for a given operating condition. Analysis will follow the same format as shown in the ignition delay section. That being with three normalization methods: (1) normalizing to the maximum of each respective fuel, (2) normalizing on a case-by-case basis, (3) normalizing to the maximum value from Fuel A. The coefficient of cylinder pressure variance will also be included for completeness and to display additional effects of low-cetane fuels.

To begin determining low-cetane fuels' effects on average peak pressure, first the trends of average peak pressure with respect to speed and load will be determined from Figure 16 below.

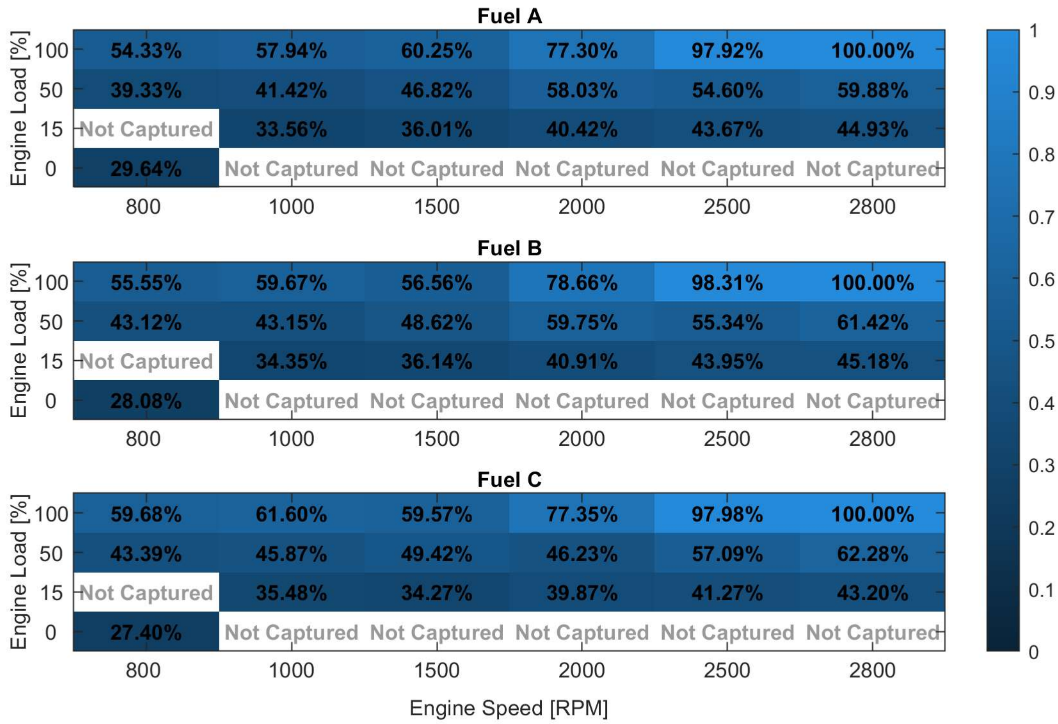

Figure 16: Avg. Peak Pressure Trends, Normalized to Max. of Respective Fuel

Figure 16 illustrates the average peak cylinder pressure for each fuel under various speed and load conditions. The value in each cell represents the average pressure recorded across all cycles and cylinders for a specific operating point. To facilitate a direct comparison of trends, each cell value was normalized to the single greatest average peak pressure achieved across all cases for their respective fuel.

The primary observation is a strong, positive correlation between peak cylinder pressure and both engine speed and load. This trend was exhibited consistently by all tested fuels, with the highest pressures occurring at the maximum speed and load condition and the lowest at idle. More significantly, the uniformity of this trend indicates that the expected increases of average peak pressure at low-speed, low-load conditions due to low-cetane fuels [17][20][24] do not fundamentally affect the relationship between engine operating conditions and peak cylinder pressure. While the absolute pressure values do vary, as shown in subsequent analysis, the shape of the pressure response across the engine map remains unchanged.

To now understand how low-cetane fuels affect peak cylinder pressure at varying operating conditions, the change in peak cylinder pressures when compared to Fuel A are presented in Figure 17 below.

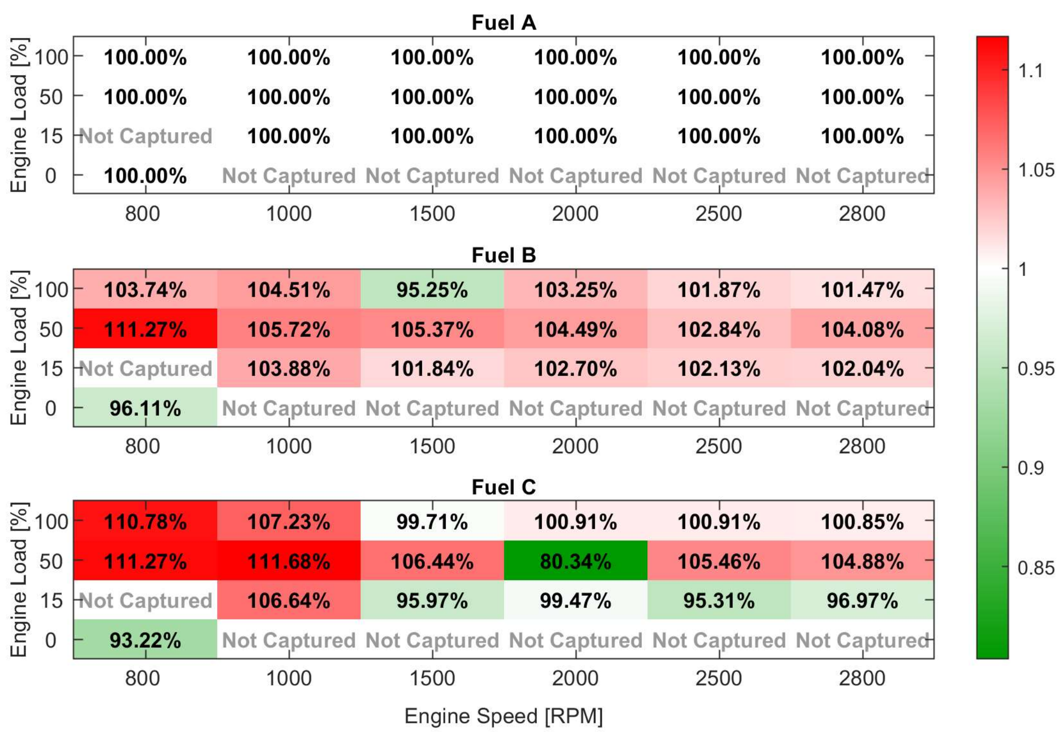

Figure 17: Changes in Avg. Peak Pressure When Compared to Fuel A

Figure 17 above displays how peak cylinder pressure is affected across operating conditions when compared to Fuel A values. Red indicates values greater than 100% of the Fuel A values and green indicates values less than 100% of the Fuel A values. Although increases in peak pressure occur at most conditions, the greatest increases of peak cylinder pressure were centered around low-speed, part-load conditions. This is consistent between Fuel B and C, with Fuel C exhibiting the largest increases. From this, it can be concluded that the durability concern is increased across most regions when reducing the cetane rating, especially at low-speed, part-load conditions when comparing identical operating conditions. Peak cylinder pressure is minimally increased at high-speed conditions for both Fuel B and C as expected [17][20][24]. Interestingly, Fuel C displays a large reduction in peak pressure at 2000 RPM, 50% load that is not shown in Fuel B. The suspected cause of this is the excessive ignition delay at this specific point when referring to Figure 13 previously displayed, included below for convenience.

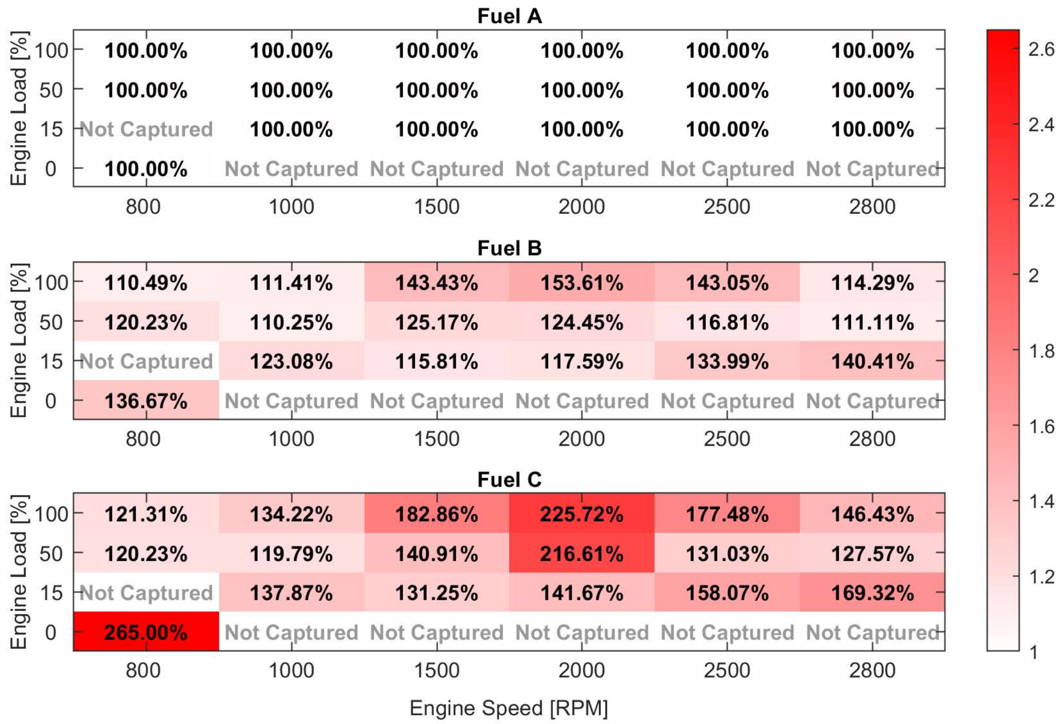

Figure 13: Change in CA Ignition Delay when Compared to Fuel A

The 2000 RPM, 50% load case for Fuel C had an exceptionally long crank angle ignition delay, specifically 216% of that calculated for the same case with Fuel A. This larger ignition delays caused SOC to not occur until just before TDC, resulting in reduced peak pressure. Interestingly, Fuel C displayed a 0.3% increase in torque compared to Fuel A at this point, while Fuel B showed a 2.2% increase in torque. Changes in peak pressure are shown in the pressure trace comparison of all fuels for this case in Figure 18 below. Results in Figure 18 exemplify the phenomenon, previously discussed in section 2.4.2, that increasing ignition delay increases peak pressure to an extent, beyond which, peak cylinder pressures are reduced.

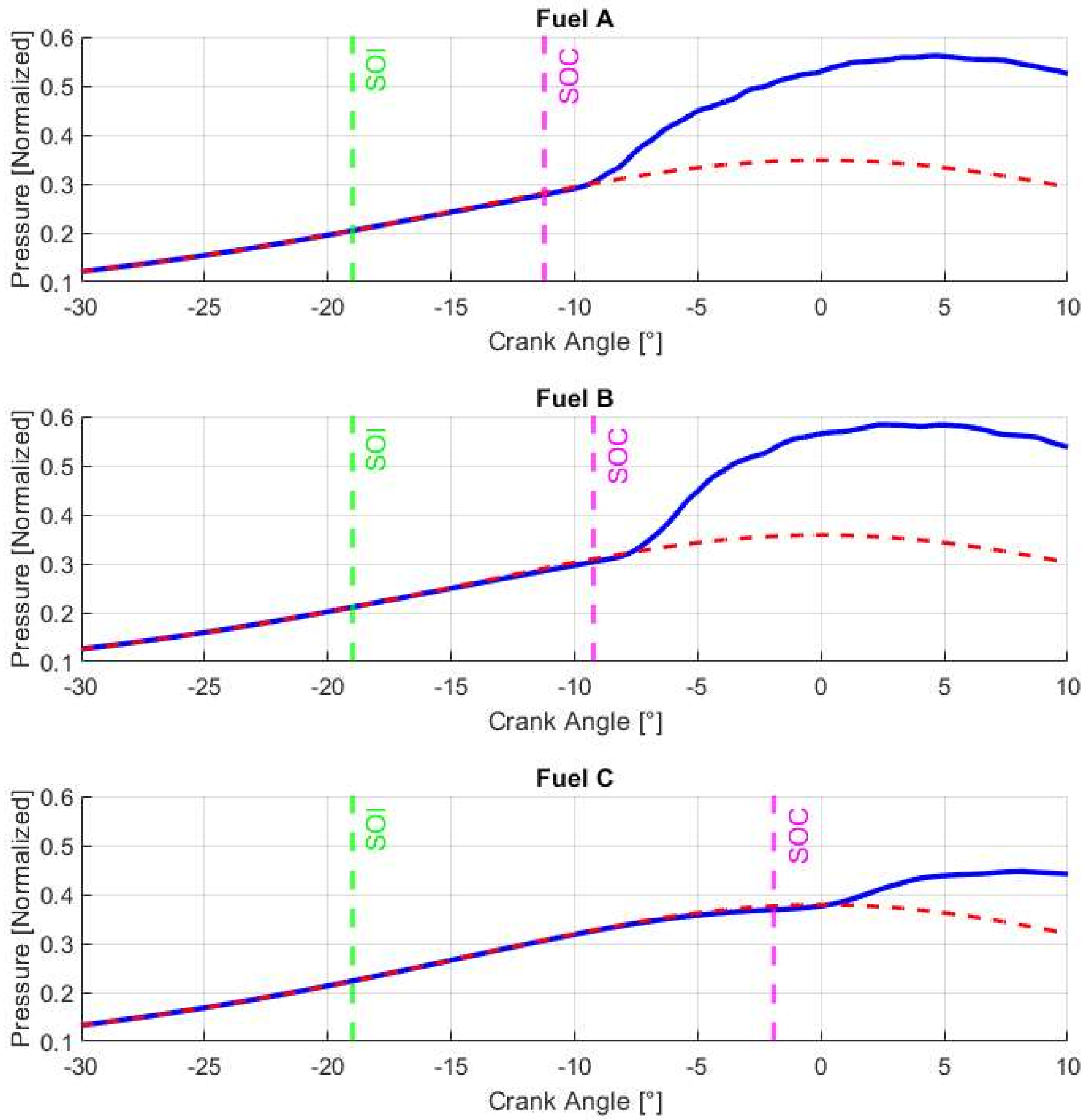

Figure 18: Pressure Trace Comparison at 2000 RPM, 50% Load

(Blue: Measured Pressure, Red: Motored Pressure)

Additionally, the 2000 rpm, 100% load case also displays a large increase in ignition delay compared to its Fuel A counterpart. This increase is ~10% more of a change than the 50% load case, without a significant reduction in average peak pressure in Figure 17. Consulting Figure 11, the crank angle ignition delay for the 100% load case is only 45% as large as the ignition delay present in the 50% load case. This suggests that despite a relatively large local increase, the increase in ignition delay at 100% load was not enough to reduce peak pressure to the same extent as the 50% load case.

To determine the extent at which peak pressure values were increased, peak pressure values were normalized to the maximum peak pressure value of Fuel A and are presented in Figure 19 below. This is intended to display what operating points exceed the global maximum cylinder pressure of Fuel A, presenting the most concerning conditions.

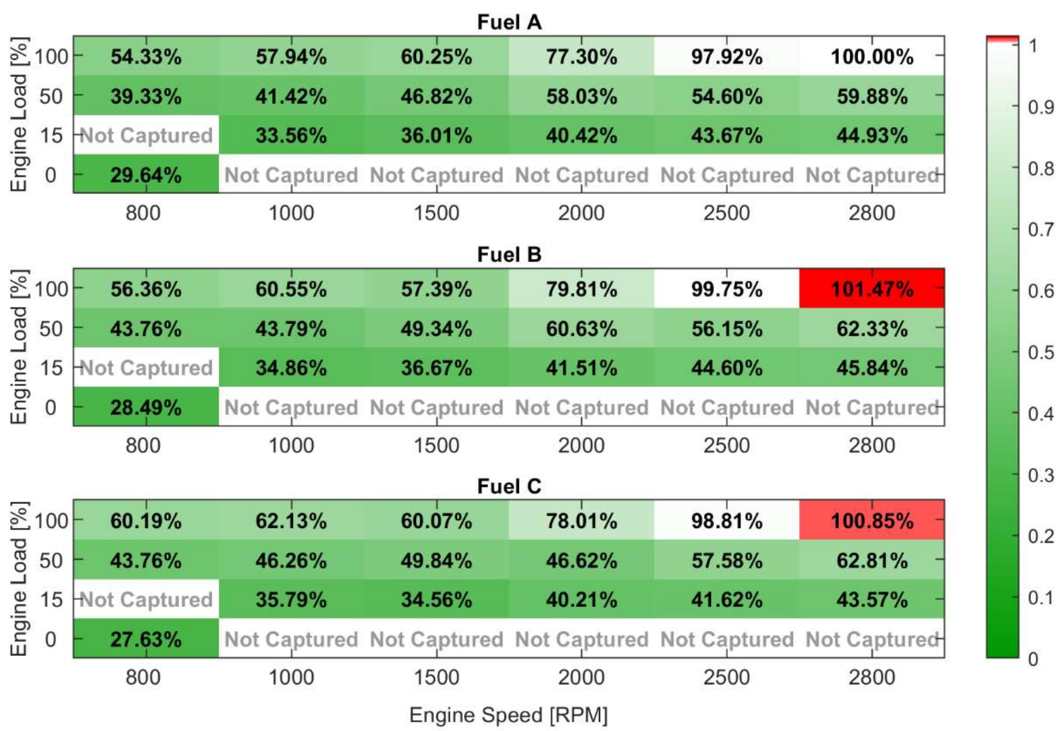

Figure 19: Avg. Peak Pressure Normalized to Max. of Fuel A

From above, peak pressures for Fuel B and C exceed the maximum of Fuel A only at high-speed, high-load conditions. This is expected after analysis of Figure 16 and

Figure 17, from which it was concluded that maximum cylinder pressure is proportional to speed and load, as well as maximum cylinder pressure increases at these specific conditions with low-cetane fuels respectively.

For a conclusion of peak cylinder pressure results, first it was determined low-cetane fuels do not affect the relationship between peak pressure and speed and load. All fuels displayed that peak pressure has a strong positive correlation with both speed and load regardless of cetane rating. Additionally, peak cylinder pressures tend to increase across most operating conditions, only decreasing due to excessive ignition delay. This suggests a local increase in the durability concern. However, these increases in peak pressure for low-cetane fuels only exceed the maximum peak pressure recorded for Fuel A at high-speed, high-load cases.

For additional understanding of how peak pressure is affected by low-cetane fuels, how much the peak cylinder pressure fluctuated for each case will be investigated. The coefficient of cylinder pressure variance is presented in Figure 20 below and can be analyzed in conjunction with Figure 17.

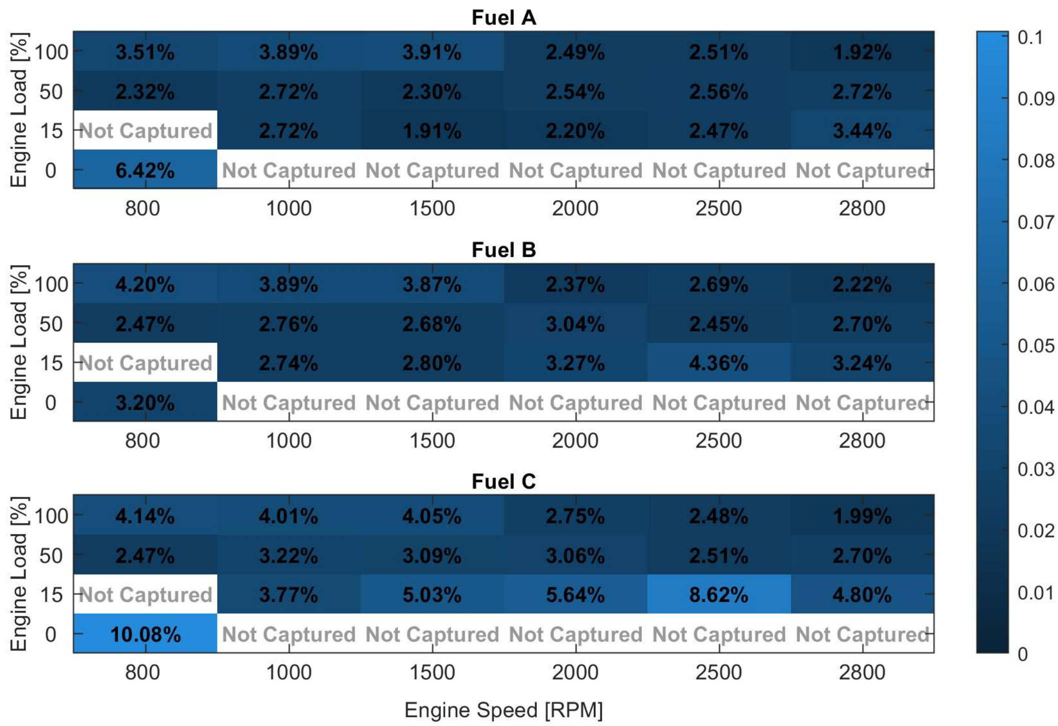

Figure 20: Coefficient of Variance of Peak Pressure

CV values presented are not normalized with respect to each other, and the gradient spans all three fuels. This displays that the CV tends to marginally increase as cetane rating is decreased except for select regions. Regions of relatively large increases in CV include 15% load for Fuel C, spanning from 1500 RPM to 2800 RPM as well as idle for Fuel C. An increase in CV is expected as increasing ignition delay may increase or decrease peak pressure, depending on the extent, as shown just prior. To further understand changes in the coefficient of variance, Figure 17, shown previously, is shown below for convenience.

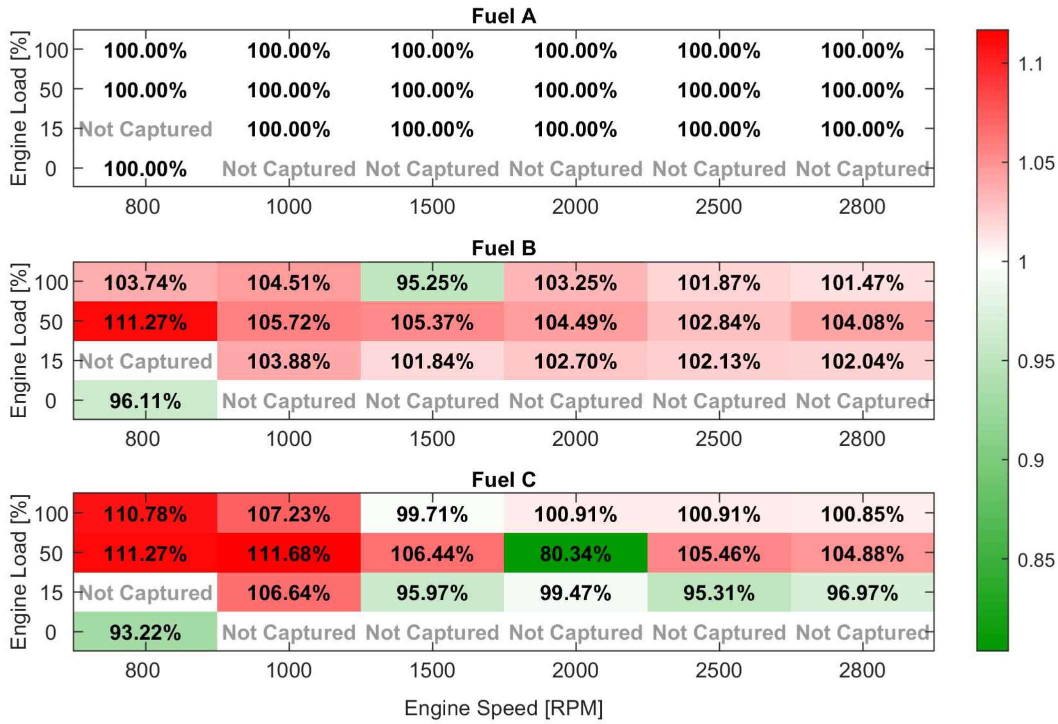

Figure 17: Changes in Avg. Peak Pressure When Compared to Fuel A

Figure 17 above displays the changes in average peak pressure when compared to Fuel A on a case-by-case basis. Most cases display an increase in average peak pressure except two notable regions, previously noted from Figure 20. Those regions being 15% load for Fuel C, spanning from 1500 RPM to 2800 RPM as well as idle for Fuel C. For the 15% load region of Fuel C, Figure 20 displays a relatively large increase in the CV when compared to the same region for Fuel A. However, Figure 17 does not display any outstanding increases in maximum peak pressure in this region, actually slightly the opposite. This suggests that the elevated CV is not caused by high-magnitude outliers, but rather by an increased frequency of lower peak pressure cycles, which reduces the mean while increasing relative variability Peak Cylinder Pressure Rise Rate

Peak pressure rise rates (PPRR) were calculated both with respect to crank angle and with respect to time. However, for the purpose of analyzing durability concerns, only PPRR with respect to time will be discussed. Although results with respect to time are blurred because of their dependency on engine speed as discussed previously, the potential for combustion to cause engine damage is a function of its time-based impact. Therefore, analyzing results in the time domain is critical for durability analysis, as it directly captures the intensity and violence of the combustion event. This allows for more effective comparison of durability effects across a range of engine speeds as compared to a PPRR with respect to crank angle. PPRR will be analyzed using the previously utilized three normalization method approach. The average PPRR value used for normalization for a given operating condition and fuel is calculated as the mean of the calculated PPRR values across all recorded cycles at that condition and fuel.

4.4.3 Cylinder Pressure Rise Rate Determination

Pressure rise rate (PRR) was determined using the gradient function in MATLAB, which utilizes the central difference method for determining the rate of change as shown in Equation 5 below, with P and t being the measured pressure and time respectively.

$$PRR_i = \frac{P_{i+1} - P_{i-1}}{t_{i+1} - t_{i-1}} \qquad [5]$$

From the calculated PRR of a cycle, the PPRR could be determined by simply taking the maximum value across the cycle. Then the average PPRR was obtained by taking the mean of these maximum values.

4.4.4 Peak Cylinder Pressure Rise Rate Results

The analysis process for PPRR will be nearly identical to that done for peak cylinder pressure. That is first observing trends, then changes, and finally concerning operating points when compared to the maximum value from Fuel A. The coefficient of variance with the average PPRR is also included for completeness.

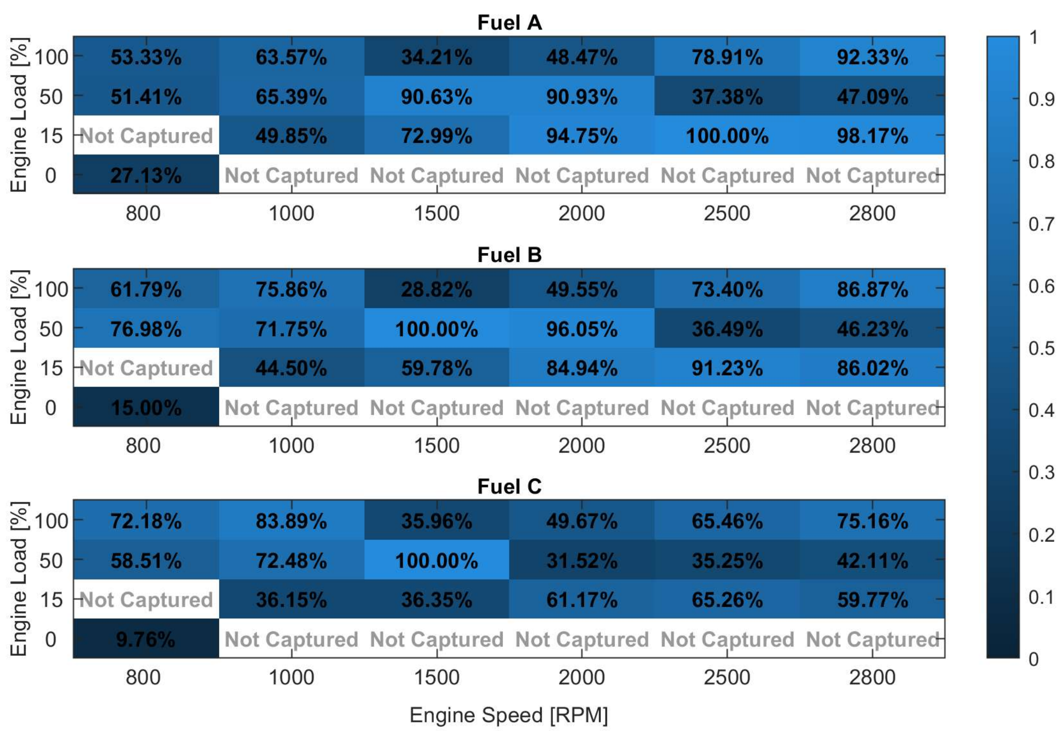

Figure 21: Avg. Peak Cylinder Pressure Rise Rate, Normalized to Max. of Respective Fuel

As utilized before, Figure 21 above will be used to observe trends of the PPRR and note any changes with cetane rating. Interestingly, the location of the maximum PPRR changed from a high-speed, low-load condition for Fuel A to a part-speed, part-load condition for Fuels B and C. However, Fuel A does show a local increase in PPRR at this specific location. Further determination of changes in PPRR can be done with Figure 22 below.

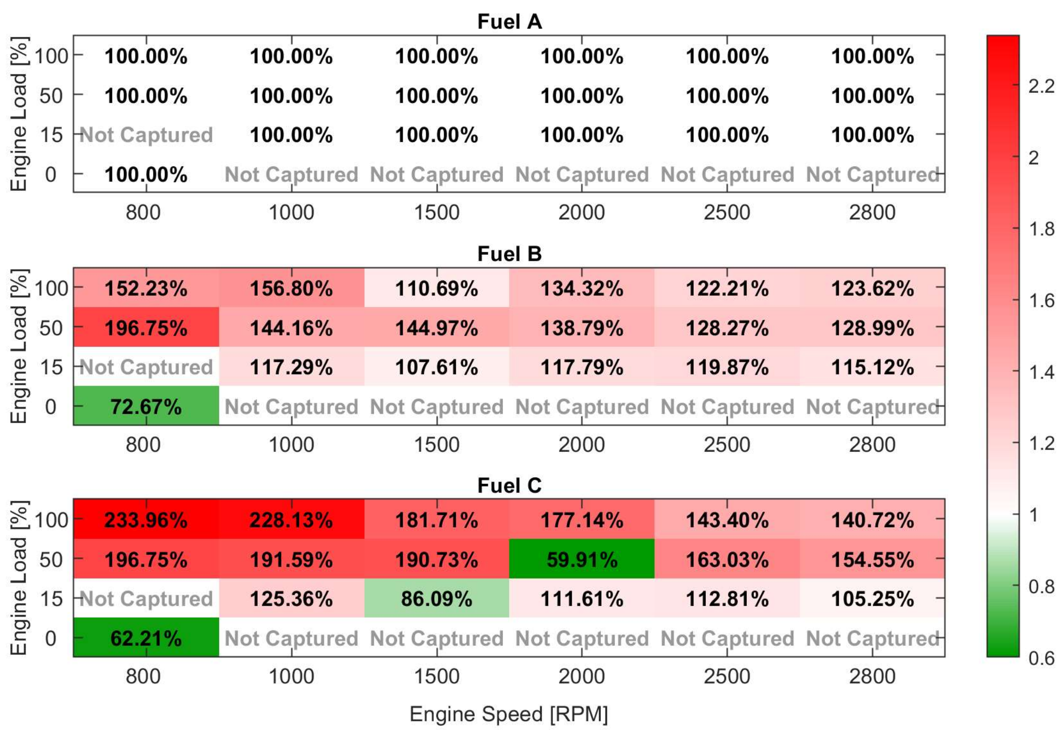

Figure 22: Changes In Avg. Peak Pressure Rise Rate When Compared to Fuel A

Figure 22 above provides further context to help understand the changes in trends noted in Figure 21. Figure 22 shows that the average PPRR has increased across a majority of cases, however, increasing to a greater extent at lower speed conditions. This helps to explain the shift in maximum PPRR location when changing cetane rating that was previously discussed. From Figure 21, Fuel A already presented 1500 RPM, 15% load as a local maximum for PPRR. With an increase in PPRR across all cases, more so at low speeds, this increased this local maximum enough to become a global maximum for all cases. Additionally, effects of the exceptionally large ignition delay at 2000 RPM, 50% load for Fuel C can still be seen with a reduction in PPRR for that case. Figure 23 is shown below to understand the magnitude of changes presented above..

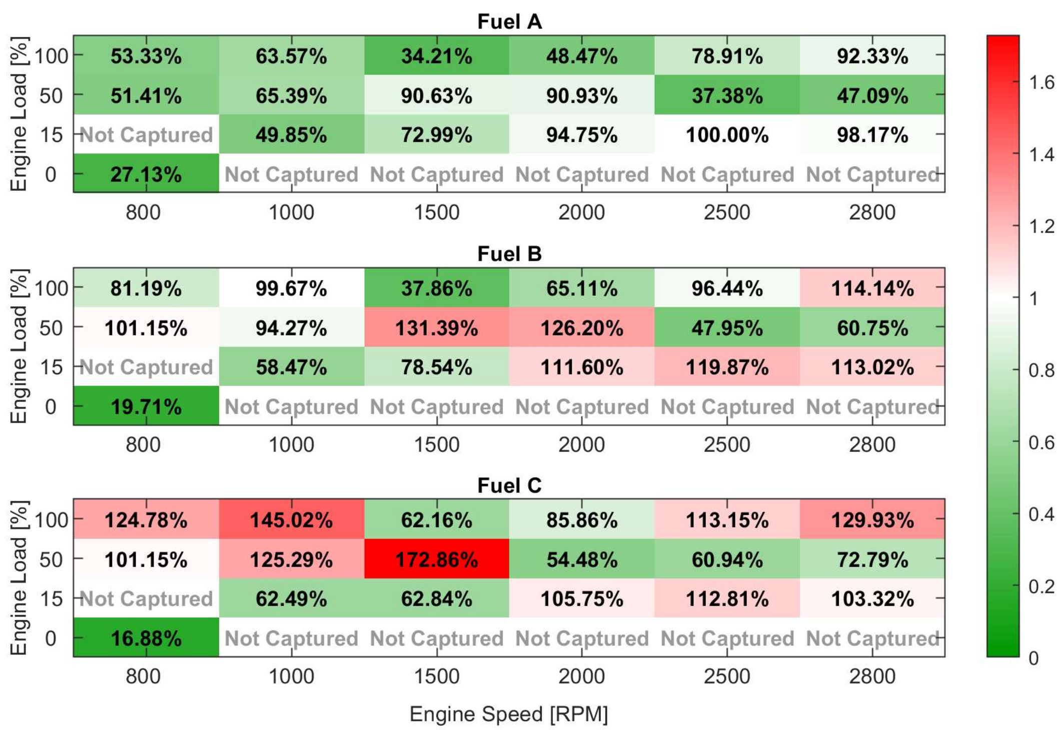

Figure 23: Peak Pressure Rise Rate Normalized to Max. of Fuel A

Figure 23 above displays the average PPRR of each case normalized to the maximum PPRR calculated for Fuel A. Red shading indicates that the PPRR for that case is larger than the largest PPRR observed for Fuel A. This allows the determination of which cases present more of a durability concern than would ever be seen with Fuel A. Consistent with both Fuel B and C, there appears to be a band of concerning conditions spanning from low-speed, high-load, to high-speed, low-load. This band is hypothesized to be a result of the step timing control utilized for injection timing in this engine, discussed in section 3.2. The transition between relatively advanced and relatively retarded is abrupt, causing conditions just prior to the shift to have excessive and audible knock. This knocking drastically reduces just after the step, which occurs at similar conditions as the band that is presented above. The case with the greatest concern for both fuels is the 1500 RPM, 50% load. Comparing Fuel B to Fuel C, Fuel C is not entirely uniformly more concerning, greater increases in concern appear at low-speed, high-load conditions. Again, the 2000 RPM, 50% load case for Fuel C displays results not consistent with the trends of neighboring cases.

From results shown for PPRR, it can be concluded that lowering the cetane rating of the fuel used does have an impact on the speed and load at which the greatest PPRR occurs. Both Fuel B and C shifted the location of maximum PPRR to part-speed, part-load conditions as opposed to high-speed, low-load conditions as seen for Fuel A. Additionally, PPRR increased across a majority of operating conditions, only reducing at idle for Fuel B and at a few points for Fuel C, including the excessive ignition delay condition, 2000 RPM, 50% load. This suggests an increase in durability concern for most cases on a case-by-case basis. These increases resulted in PPRR values that exceeded the maximum value observed for Fuel A more sporadically, with a band of increased PPRR around the step timing control shift region.

For a more thorough understanding of PPRR behavior, the CV of PPRR for each operating condition will be investigated and is presented in Figure 24 below.

Figure 24: Peak Pressure Rise Rate CV

CV values above are not normalized, and the gradient spans all three fuels. From Figure 24 above, CV values tend to increase as the cetane rating is decreased at a similar rate as seen in the CV for peak pressure values. Additionally, the region with the greatest coefficient of variance appears to be similar, that being for Fuel C and at high-speed, low-load conditions and idle. Combining this information with Figure 22 previously shown, provided below for convenience, will aid in the understanding of how PPRR is fluctuating to cause the CV to increase.

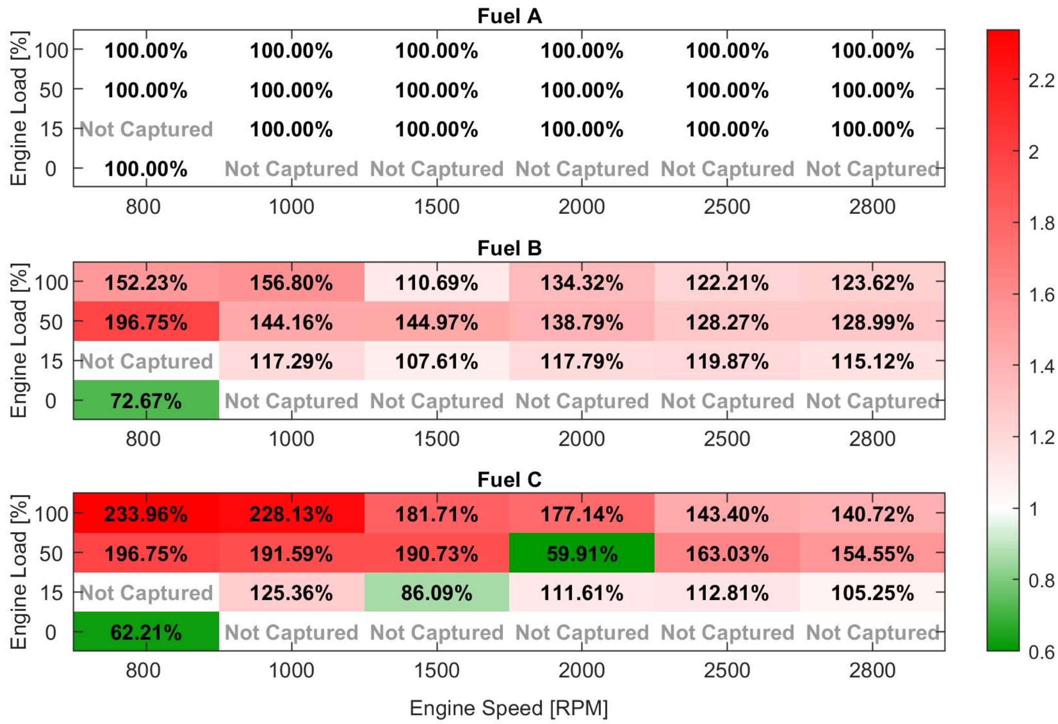

Figure 22: Changes In Avg. Peak Pressure Rise Rate When Compared to Fuel A

Figure 22 above shows that average peak pressure rise rates for Fuel C are relatively low at high-speed, low-load and idle conditions compared to neighboring points. Additionally, the difference between neighboring points is greater than that of similar conditions for Fuel B. Additionally, PPRR values for this region aren't excessively reduced. This suggests that the elevated CV is not caused by high-magnitude outliers, but rather by an increased frequency of low-PPRR cycles, which reduces the mean while increasing relative variability

Chapter 5 Crankshaft Twist

The twist of the crankshaft was determined with the use of a pair of encoders attached to the front and rear of the crankshaft. There are limitations to this method, which will be discussed in the following section. Three metrics were calculated from crankshaft encoder data captured, guided by literature discussed in section 2.4.2: absolute twist angle, peak-to-peak twist angle, and rate of twist. Absolute twist angle and peak-to-peak twist are used to represent maximum torsional stress and cyclic torsional strain, both of which have been used as predictors of crankshaft life [46][47]. Rate of twist specifically is not directly linked to any wear mechanisms within the crankshaft; however, it was chosen as an indicator of the vibration and violence that crank train components are subjected to. For each of these metrics, the maximum value recorded throughout data acquisition was determined and will be the main subject of analysis. An illustration of the determination for each of these metrics is provided in Figure 25 below as well as a description and the purpose of each metric in Table 4.

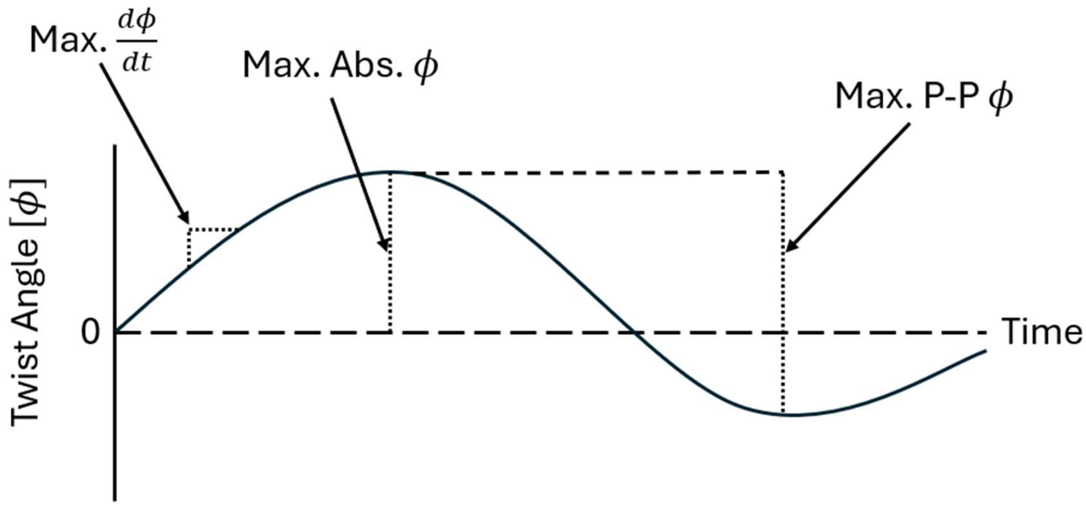

Figure 25: Calculated Crankshaft Twist Metrics

Table 4: Calculated Crankshaft Metrics

Metric	Calculation and Description	Analytical Purpose
Absolute Twist Angle (ϕ)	Calculated as the maximum absolute twist angle. Provides maximum deflection from the neutral position.	Proportional to maximum strain (γ) and, since within materials elastic limit, proportional to maximum stress (τ).
Peak-to-peak Twist Angle (P-P ϕ)	The total range of torsional motion, calculated as the difference between the maximum and minimum observed angles at an operating condition	Proportional to the cyclic strain range ($\Delta\gamma$).
Rate of Twist ($\frac{d\phi}{dt}$)	The first derivative of the instantaneous twist angle signal with respect to time. Quantifies the speed of torsional deflection.	Serves as an indicator of shock loading as well as crank train vibration and violence

5.1 Crankshaft Twist Measurement Limitations

There are three limitations with the twist data presented. First of which is regarding what data was collected. Insufficient data was collected for Fuel C, resulting in some operating points for Fuel C labeled ‘Not Captured’. The second and third limitations are regarding two-encoder method. Specifically, this method limits the ability to observe all twists along the crankshaft accurately, which in turn limits the ability to accurately calculate the torsional stress and torsional strain along the crankshaft. These latter two limitations are discussed in more depth in for the remainder of this section.

As for the second limitation, when observing crankshaft position only on either end with the two-encoder method, there may exist a condition that results in the mid-section of the crankshaft significantly twisting without the front and rear encoders observing the same magnitude of twist. An illustration of this a situation like this is shown in Figure 26 below.

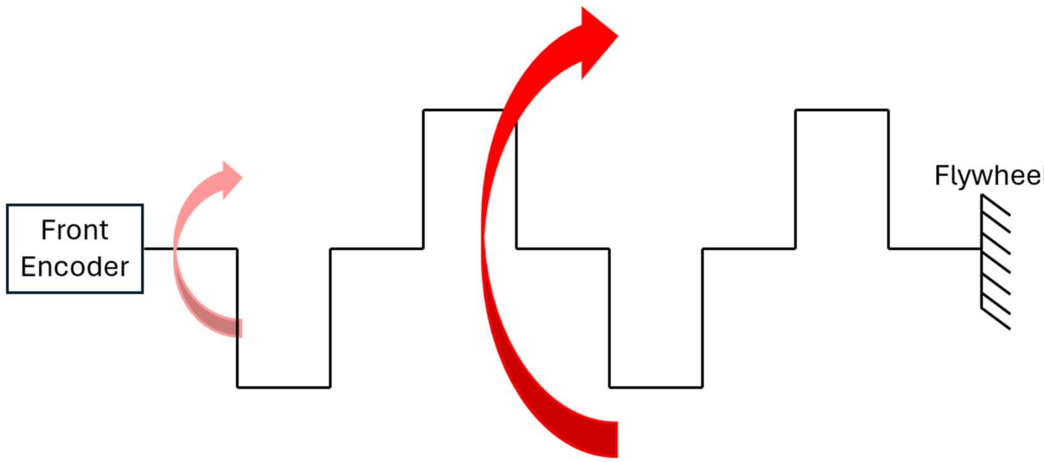

Figure 26: Possible Crankshaft Twist Scenario

Figure 26 illustrates a scenario in which there is more twist in the crankshaft than is observed with the front and rear encoders. This would result from a larger twist midway along the length of the crankshaft and the inertia of both ends of the crankshaft limiting observed twist. For explanation purposes, the flywheel encoder is assumed to be fixed, as the inertia of the flywheel in addition to the dynamometer will significantly increase the force required to rotate the rear as compared to the front. This increase in force required prevents the flywheel and attached encoder from assuming the same twist angle as anywhere in the crankshaft, reducing observed change in position by the rear encoder. The front end of the crankshaft can be considered freer when compared to the flywheel. This can be assumed since the only restrictions preventing the front end from assuming the same twist as anywhere in the crankshaft is the inertia of the crankshaft and inherent crank train friction between the maximum twist location and the encoder.

Accordingly, twist angles for explanation purposes will be in reference to the flywheel position. Figure 27 below provides further clarification of what the scenario described above would entail with exaggerated twist angles.

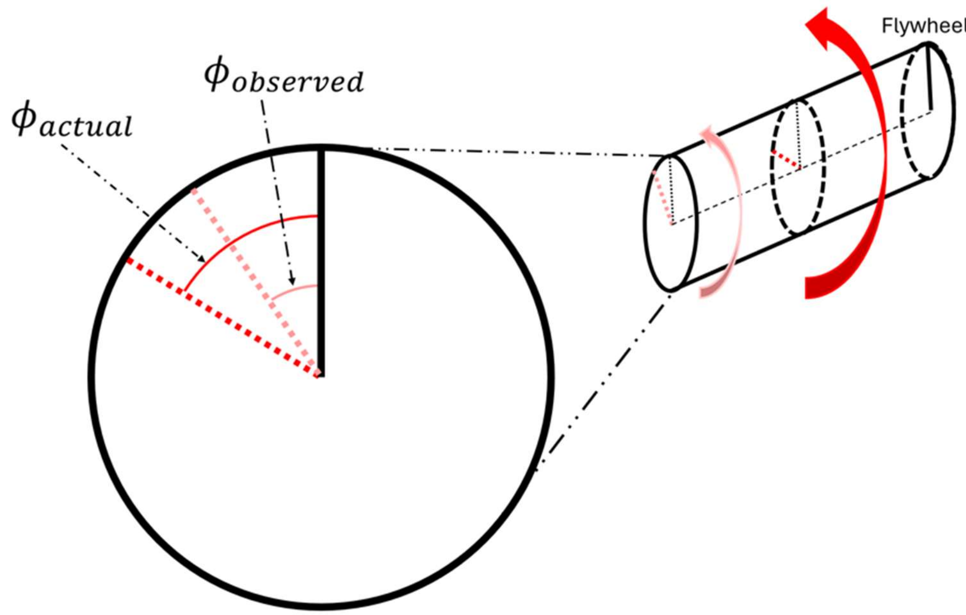

Figure 27: Observed and Actual Twist Along Crankshaft

Figure 27 extends the scenario presented in Figure 26 by modeling the crankshaft as a simplified beam with a larger twist angle occurring midway along its length. Figure 27 illustrates the difference between the actual crankshaft twist angle, ϕ_{actual}, and the twist angle observed by the front encoder, $\phi_{observed}$, when a localized maximum twist occurs at the center of the crankshaft.

When only two encoders are installed at the front and rear of the crankshaft, this deformation would be measured as a smaller twist than is actually present within the shaft, highlighting a limitation of the two-encoder method. However, as the location of maximum twist moves closer to the front of the crankshaft, the observed twist angle approaches the actual twist angle. This occurs because a maximum twist nearer to the front reduces the available inertia between the twist location and front encoder that would otherwise attenuate the deformation.

Consequently, while the collected data remains valid, it does not provide a complete representation of the torsional dynamics along the entire crankshaft. Not all combustion-induced deformations are captured with their true magnitudes; however, torsional responses originating from the front cylinders are expected to be the most prominent and exhibit the largest measured twist angles, as shown in Figure 28 below.

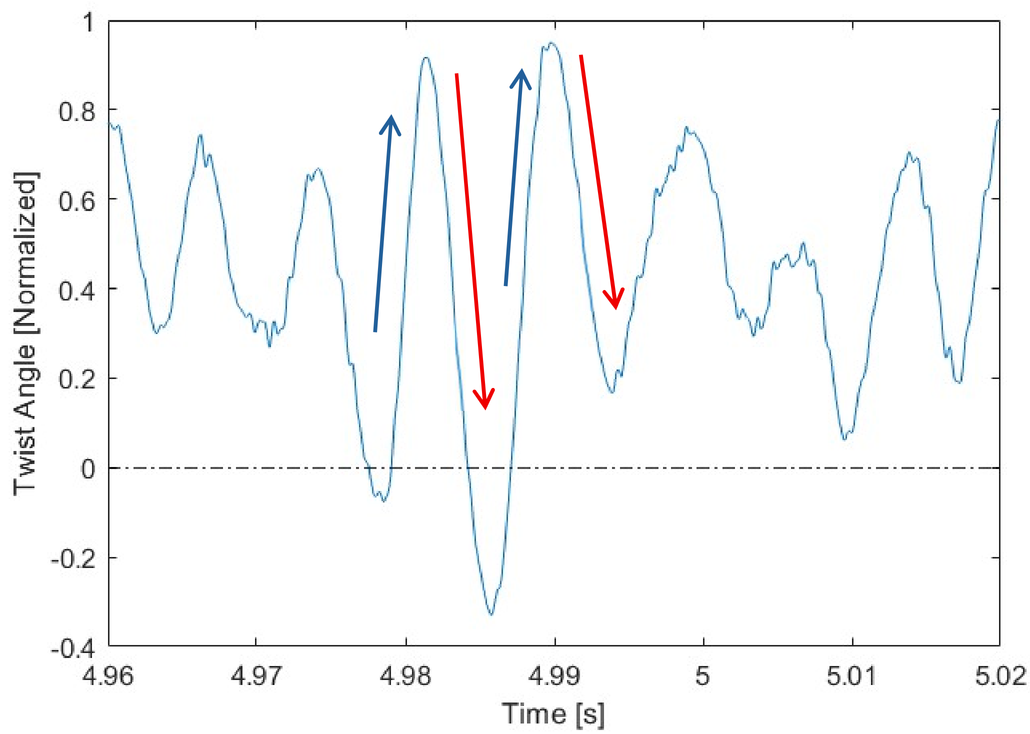

Figure 28: Normalized Twist Angle, Fuel A: 2000 rpm, 100% Load

(Blue Arrow: Compression, Red Arrow: Combustion)

Figure 28 shows the crankshaft twist angle measured using the two encoders. As described in Section 5.2, the twist angle calculation is defined such that a positive twist angle indicates the front encoder position is lagging the rear encoder position, while a negative twist angle indicates the front encoder is leading the rear encoder position, both relative to the direction of crankshaft rotation.

Under this sign convention, crankshaft twist resulting from compression of the air–fuel mixture produces an increase in twist angle, corresponding to deformation opposite the direction of rotation. Conversely, crankshaft twist resulting from combustion produces a decrease in twist angle, corresponding to torsional deformation in the direction of rotation.

The time window shown in Figure 28 spans 0.06 s, which corresponds to two complete crankshaft rotations at 2000 rpm. With this interval, and based on the explanation above, eight individual compression and combustion events are clearly distinguishable. Furthermore, given the firing order of 1-5-4-8-6-3-7-2, and noting that cylinders one and five are closest to the front encoder, shown in Figure 29 below, the observation of the two largest twist events occurring consecutively is consistent with the expected torsional response. Specifically, deformations due to the front most cylinders will be the largest observed.

With the reasoning above, taking the maximum twist angles observed provides the most accurate representation of deformation due to compression and combustion.

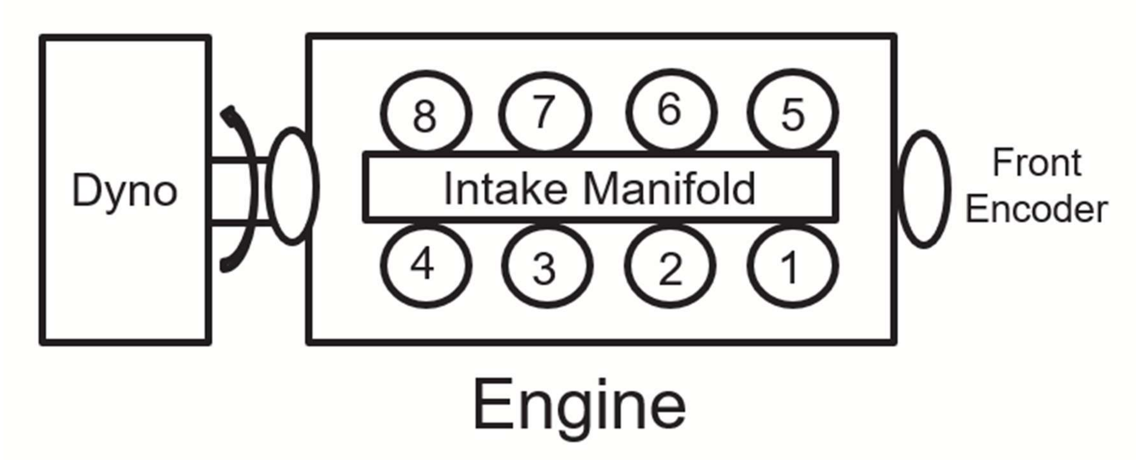

Figure 29: Cylinder Numbering Convention

The third limitation of the two-encoder method is the inability to accurately calculate strain within the crankshaft; accordingly, results will be shown as normalized angles of twist rather than using the observed twist to obtain a shear stress or shear strain value. This decision was made based on three reasons presented below, all based on the shear strain equation, shown in Equation 6 below [33], in which γ, ρ, ϕ, and L are the shear strain, radial distance, twist angle, and length respectively.

$$\gamma = \frac{\rho\phi}{L} \qquad [6]$$

First, calculating strain within the crankshaft with any amount of accuracy is not feasible for this research. Calculations would require detailed knowledge of the geometry of the crankshaft which was not available for this research. This also limits the ability to calculate stress in the crankshaft. Furthermore, to account for the lack of geometry and simplifying the crankshaft to a beam to obtain a strain with the use of a constant length and radius was investigated. Although this would allow for the results of this thesis to be compared to other research, all results have been normalized, mitigating the benefits of obtaining a simplified strain value. Ultimately, it was decided to continue with the use of normalized twist angle due to the twist angle inherently being proportional to the strain amount as shown in Equation 6 prior. Therefore, as an example, a 15% increase in twist angle will result in a 15% increase in strain [33]. Furthermore, with Hooke's law and the assumption that only elastic deformations will occur, a 15% increase in strain will result in a 15% increase in stress [49].

5.2 Maximum Absolute Crankshaft Twist

Maximum absolute crankshaft twist, representing the maximum deflection from the neutral position, was calculated. This value is proportional to the maximum strain as previously discussed and is an indicator of stress within the crankshaft.

To begin calculating the absolute crankshaft twist, the front encoder's position was subtracted from the rear encoder's position as shown in Equation 7 below. This provided twist angle as a function of time with positive and negative values representing the front encoder position lagging or leading of the rear encoder's position respectively.

$$\Delta\phi_i = \phi_{rear_i} - \phi_{front_i} \quad [7]$$

Following this, the maximum absolute value of twist was determined, giving the maximum crankshaft twist as $\Delta\phi_{max}$ in Equation 8 below. This provides the maximum deflection from the neutral position.

$$\Delta\phi_{max} = max|\Delta\phi| \quad [8]$$

5.2.1 Maximum Absolute Crankshaft Twist Results

As in previous sections, first trends with respect to each fuel will be discussed. Maximum absolute twist values, normalized to the maximum twist for each fuel, are presented below in Figure 30.

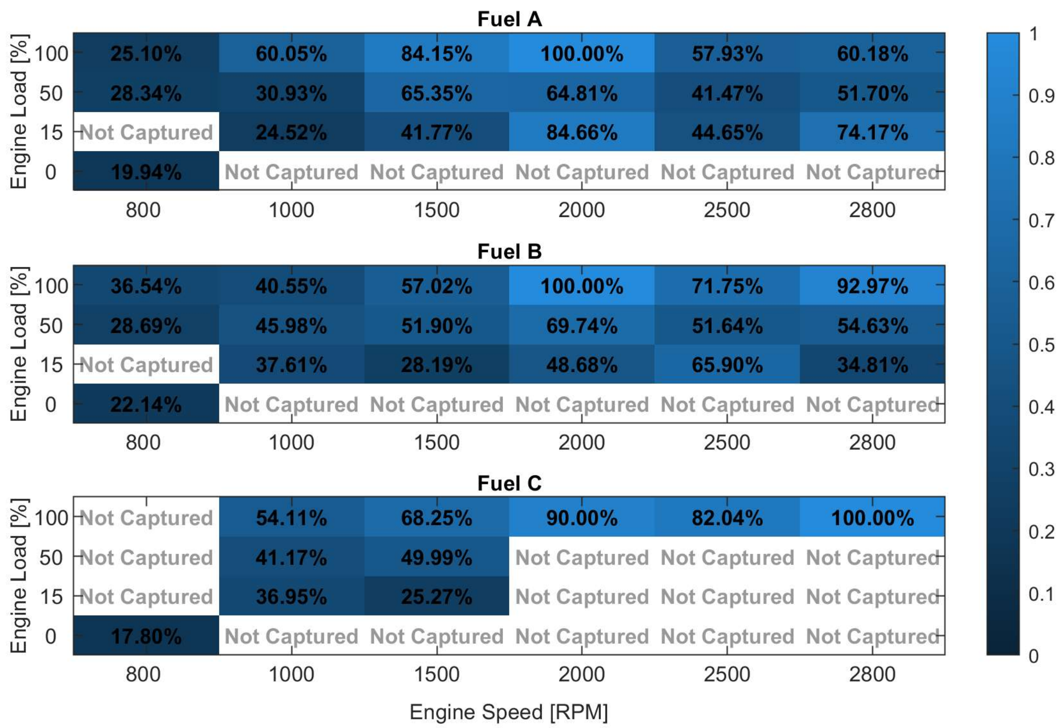

Figure 30: Max. Abs. Twist, Normalized to Max. of Respective Fuel

Maximum absolute twist values for each fuel show a strong trend of peaking near 2000 RPM. This trend is consistent regardless of load. Considering none of the combustion metrics previously discussed displayed any outstanding behavior at 2000 rpm, this suggests that the increase in twist may be due to 2000 rpm exciting the resonant frequency in the crankshaft. To investigate this further, a fast Fourier Transform (FFT) was calculated for absolute crankshaft twist during a speed sweep at 100% load and is presented in Figure 31 below.

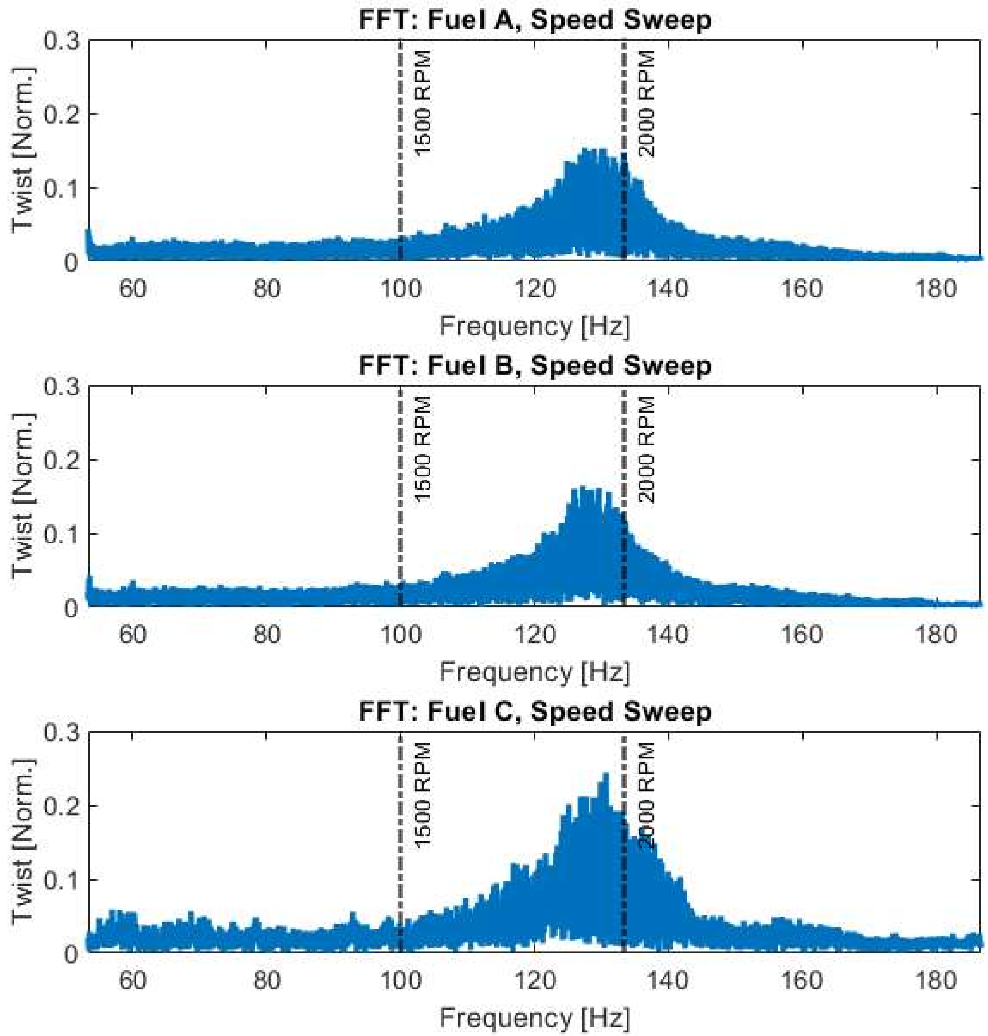

Figure 31: FFT of Max. Abs. Twist for Speed Sweep,100% Load

Figure 31 presents crankshaft twist amplitude across a frequency range, specifically focusing on the 4th order vibration across an engine speed range of 800 to 2800 RPM, 53 to 186 Hz respectively. This range was arrived at with two deductions. First, the crankshaft's fundamental torsional resonant frequency is predicted to be within

50-500 Hz [27][53]. Next this range was narrowed to only include the 4th order, representing the primary combustion frequency for the V8 engine (four firing events per rotation), which is the order that has been found to have the greatest influence on crankshaft torsional vibration and failure [27][53].

FFTs for all fuels show a distinct increase in torsional twist magnitude at approximately 130 Hz, corresponding to a 4^{th} order vibration at 1950 RPM, strongly the resonant frequency of the crankshaft is or is near 130 Hz. Twist amplitude appears to increase the most at this resonance as cetane rating is reduced, however, this increase is marginal for Fuel B and more significant for Fuel C. Further analysis can be done with Figure 32, displaying the difference in maximum absolute twist when compared to Fuel A, below.

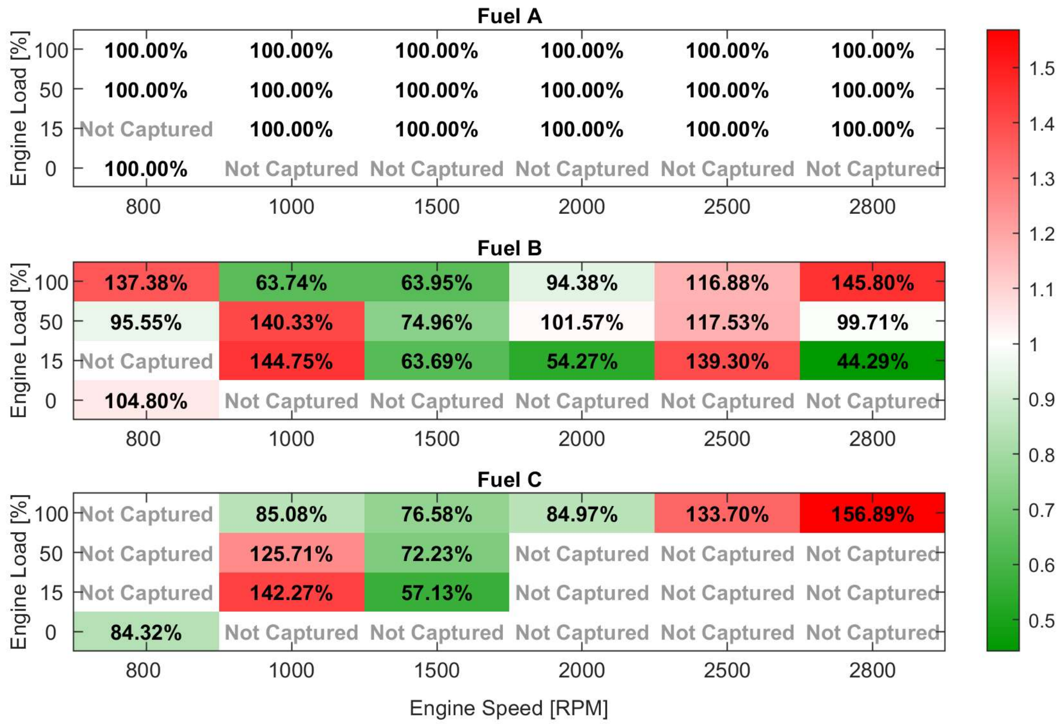

Figure 32: Change in Max. Abs. Twist When Compared to Fuel A

Interestingly results from Figure 32 display that maximum absolute twist tends to increase at most operating conditions outside of the resonant speed, while Figure 31 displayed torsional amplitude increasing most at the resonant speed. The greatest relative increases in maximum absolute twist occur at high-speed, high-load conditions. This results is notable considering previous research concluded that low-cetane effects are minimal at these conditions [17][20][24].

The hypothesized reason for the lack of twist increase at resonant speed is that the crankshafts natural dynamic amplification is a dominant factor at resonant speed. This results in the absolute twist magnitude being amplified for all cases regardless of cetane value, possibly masking the effects of violent low-cetane combustion. In contrast at nonresonant speeds, the effects of low-cetane are much more prevalent due to the natural amplification being minimal.

Regardless, the general increase in maximum absolute twist outside of the torsional resonance still signifies a heightened durability concern when compared to Fuel A on a case-by-case basis. To contextualize this risk, Figure 33 is presented to determine if the increases present result in maximum absolute twist values that exceed the greatest maximum absolute twist value present across Fuel A.

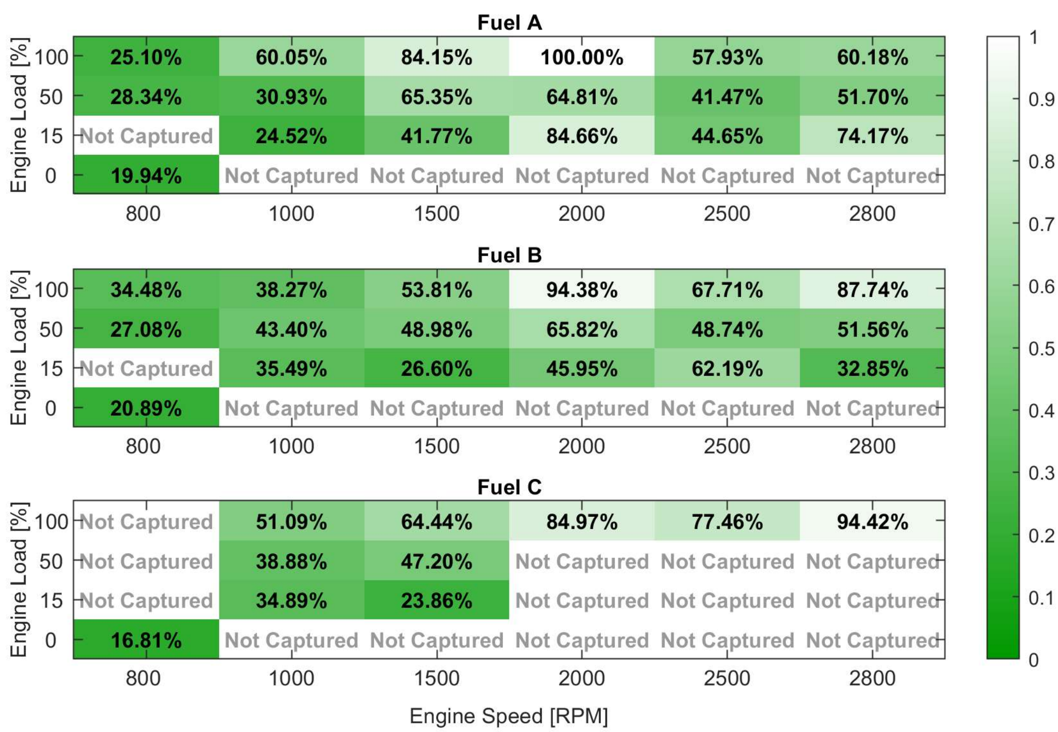

Figure 33: Max. Abs. Twist, Normalized to Max. of Fuel A

Despite relative increases in maximum absolute twist, as seen in Figure 32, no cases exceed the maximum absolute twist observed for Fuel A. However, the increases in maximum absolute twist at high-speed, high-load conditions for Fuels B and C are shown to be quite significant. Maximum absolute twist values for Fuels B and C at these conditions reach 87% and 94% of the greatest maximum absolute twist present in Fuel A respectively, while the high-speed, high-load case for Fuel A only reaches 60% of this value. Furthermore, the Fuel C value even exceeds its own maximum absolute twist value present at resonance, a similar result as seen in Figure 30.

To conclude the results presented, the resonant frequency of the crankshaft is excited in the speed range tested and each fuel displayed an increase in maximum absolute twist in this region. However, the dynamic amplification at resonance is believed to have masked low-cetane effects as increases in maximum absolute twist when compared to Fuel A on a case-by-case basis were only outside of the resonance region. With knowledge of the resonance location, its notable that the maximum absolute twist for Fuel C occurred outside of this region, at a high-speed, high-load condition, a region thought to not be affected by low-cetane fuels [17][20][24]. Additionally, this condition was not outstanding for Fuel A. Despite increases on a case-by-case basis, maximum absolute twist values for Fuels B and C never exceeded the maximum value present for Fuel A across all conditions.

5.3 Peak-to-Peak Crankshaft Twist

Peak-to-peak crankshaft twist, representing the total range of torsional motion from the minimum to the maximum observed angle, was also calculated. This value is proportional to the total cyclic strain range ($\Delta\gamma$) and will be the primary indicator of the repetitive loading conditions that contribute to material fatigue.

Calculating the peak-to-peak crankshaft twist begins with an identical first step to calculating the maximum absolute crankshaft twist, that being determining the twist angle as shown previously. With an array of twist angle values, the minimum twist angle was subtracted from the maximum twist angle as shown in Equation 9 below, providing peak-to-peak twist. This provided the spread of the twist angle, ultimately the difference between the highest peak and the lowest trough.

$$\Delta\phi_{P-P} = \phi_{max} - \phi_{min} \qquad [9]$$

5.3.1 Peak-to-Peak Crankshaft Twist Results

First, peak-to-peak twist values were compared for each fuel. This allowed for the observation of the trends of peak-to-peak twist present. Results are presented in Figure 34 below.

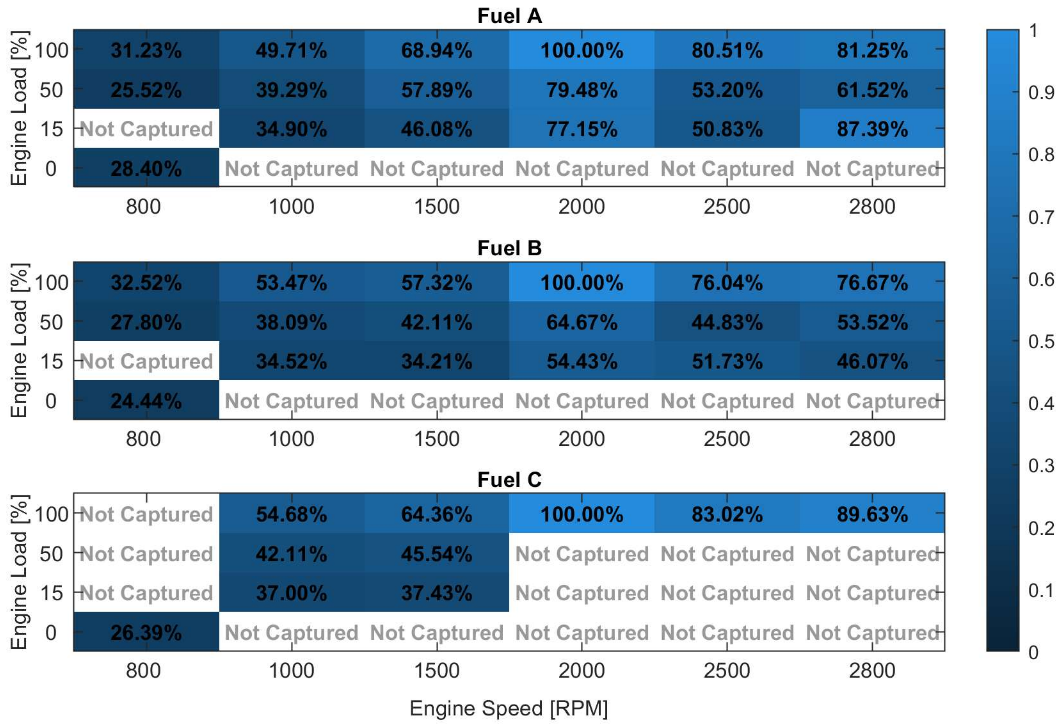

Figure 34: Max. Peak-to-Peak Twist, Normalized to Max. of Respective Fuel

From Figure 34 above, it can be seen that for all fuels, the maximum peak-to-peak twist values are centered around 2000 RPM, 100% load. This suggests that cetane rating does not change the relationship between peak-to-peak twist and speed and load. As for the increase in peak-to-peak twist being at 2000 RPM, reasoning for this is identical to that provided previously, that being the resonant frequency of the crankshaft occurs just below this speed.

Figure 35 below displays the change in peak-to-peak twist for Fuels B and C when compared to Fuel A. This allows for the determination of how differing conditions are affected by the cetane rating, with respect to the peak-to-peak twist.

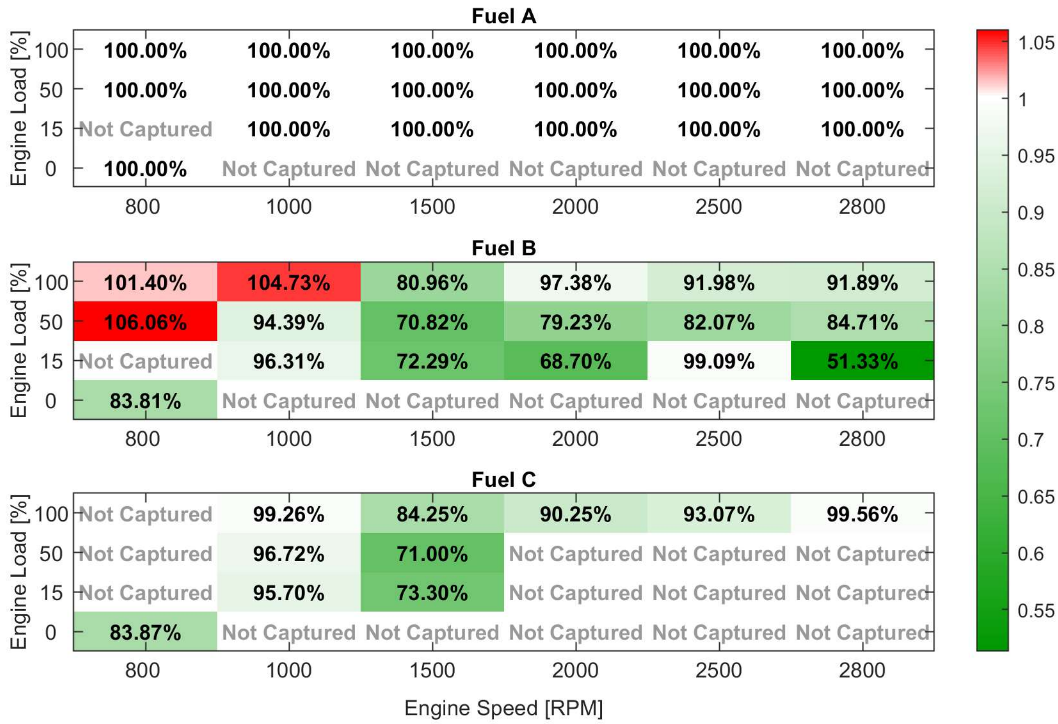

Figure 35: Change in Max. P-P Twist When Compared to Fuel A

From Figure 35, peak-to-peak twist values reduce for most cases, except for low-speed, high-load conditions. Contrary to results from the maximum absolute twist, shown in Figure 32, Figure 35 does not display an increase in maximum peak-to-peak twist at high speeds. Figure 36 below displays what a shift in the twist signal would look like that would cause the contrary results presented above.

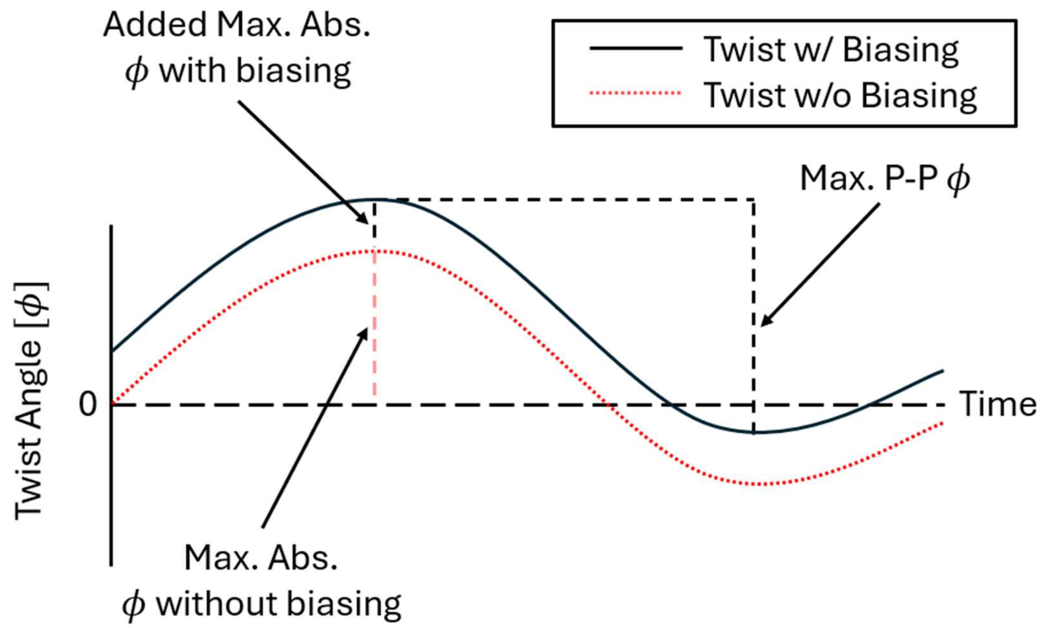

Figure 36: Increase in Max. Twist without Increase in P-P Twist

Comparing Figure 32 and Figure 35 further with the representations of twist biasing above, this twist biasing appears to be dependent on speed and cetane rating. Dependence on speed is noted as peak-to-peak changs only deviate from the absolute twist changes at higher speeds. Additionally, dependence on cetane rating is observed as the disparity between absolute and peak-to-peak twist values increases as cetane rating is lowered. This suggests that at higher speeds, lowering the cetane rating encourages biasing twisting. To confirm these dependencies with collected data, Figure 37 and Figure 38 are provided below.

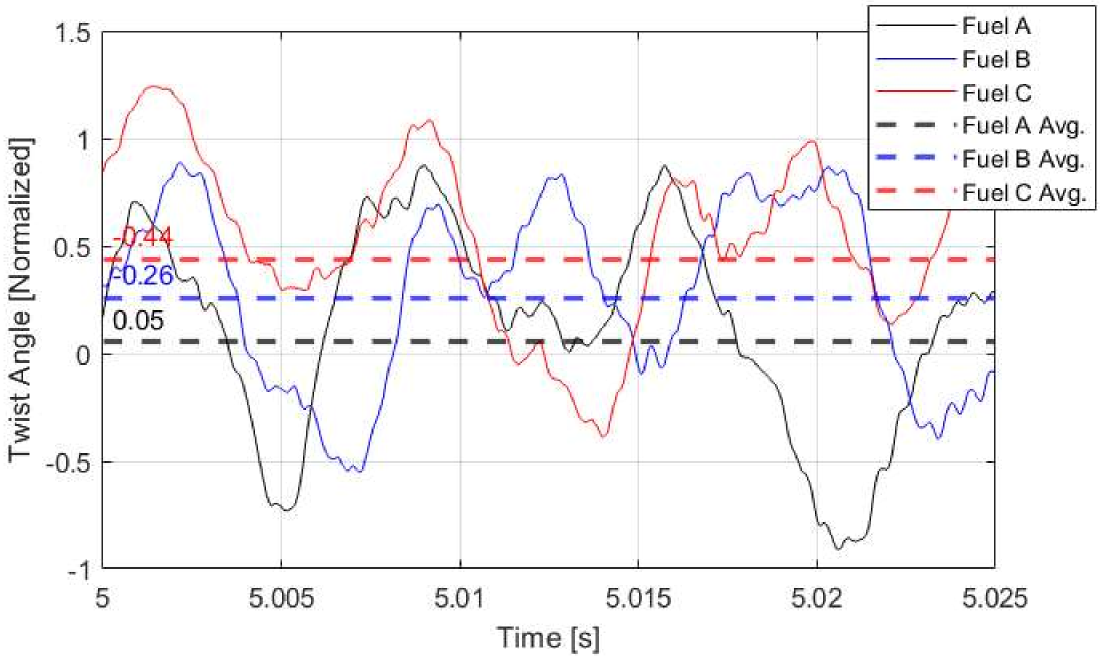

Figure 37: Twist Biasing, 2500 rpm, 100% load

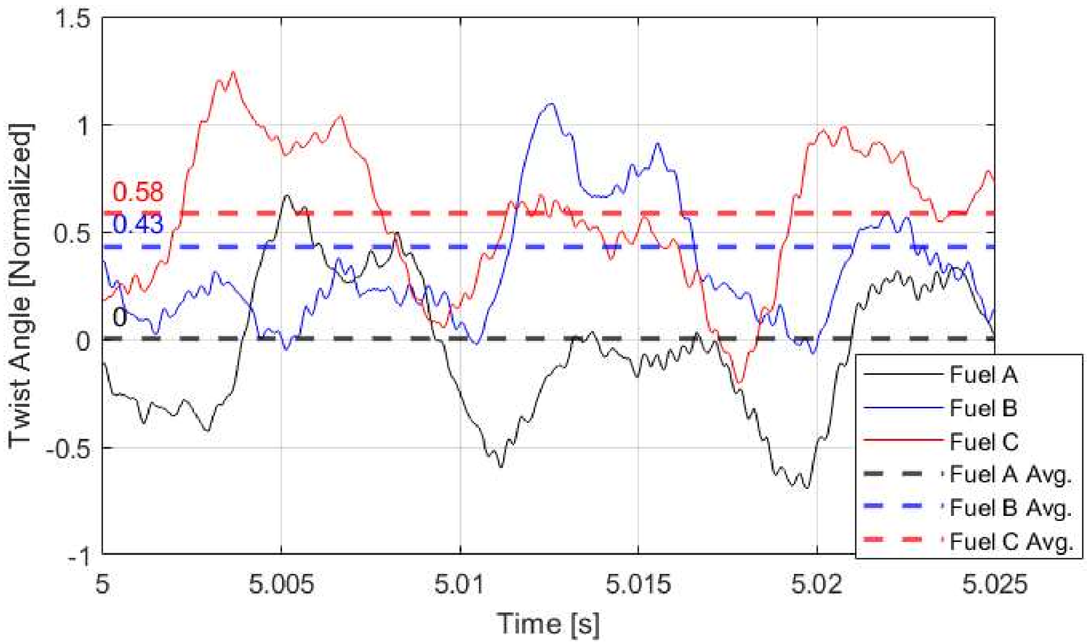

Figure 38: Twist Biasing, 2800 rpm, 100% load

Figure 37 and Figure 38 present the twist signals for each fuel at 100% load for 2500 and 2800 RPM, respectively. All signals are normalized to the maximum twist value of Fuel A at their respective operating condition. The mean value of each signal, aiding in the detection of twist biasing, is indicated by a dashed line. The primary finding is that this twist biasing becomes more pronounced with a combination of increasing engine speed and decreasing fuel cetane number. Notably, only the low-cetane fuels exhibit this speed-dependent shift with the mean twists for Fuel A being similar for both speeds. This suggests the biasing is not a simple inertial effect of higher speed, but rather a phenomenon specific to low-cetane combustion at high speeds.

Given that the shifts present are positive and conclusions from Figure 28 suggesting positive deformations occur due to compression stroke work, the positive shift in the mean twist implies a greater average deformation occurring during the compression stroke. An increase in compression work would be expected to reduce net torque output, and the results partially support this hypothesis. At both speeds, Fuel C shows a 1% torque reduction compared to Fuel A. However, Fuel B displays a marginal torque increase.

A potential point of confusion is how significant torque is produced if the measured twist remains largely positive, suggesting minimal deformation in the direction of rotation. However, it’s important to note the twist angles shown are inherently the front encoder position subtracted from the rear. This means that twist values follow a gradient between the front and rear encoder position, allowing for negative twist angles that will not be observed by the front encoder. However, given that the front cylinders' torque contribution should be accurately captured, Section 5.1, the lack of significant negative twist at the front suggests potential uneven torque distribution among the cylinders. To investigate the root cause of this increased compression-stroke deformation and the resulting twist biasing, the corresponding cylinder pressure traces are analyzed Figure 40 below.

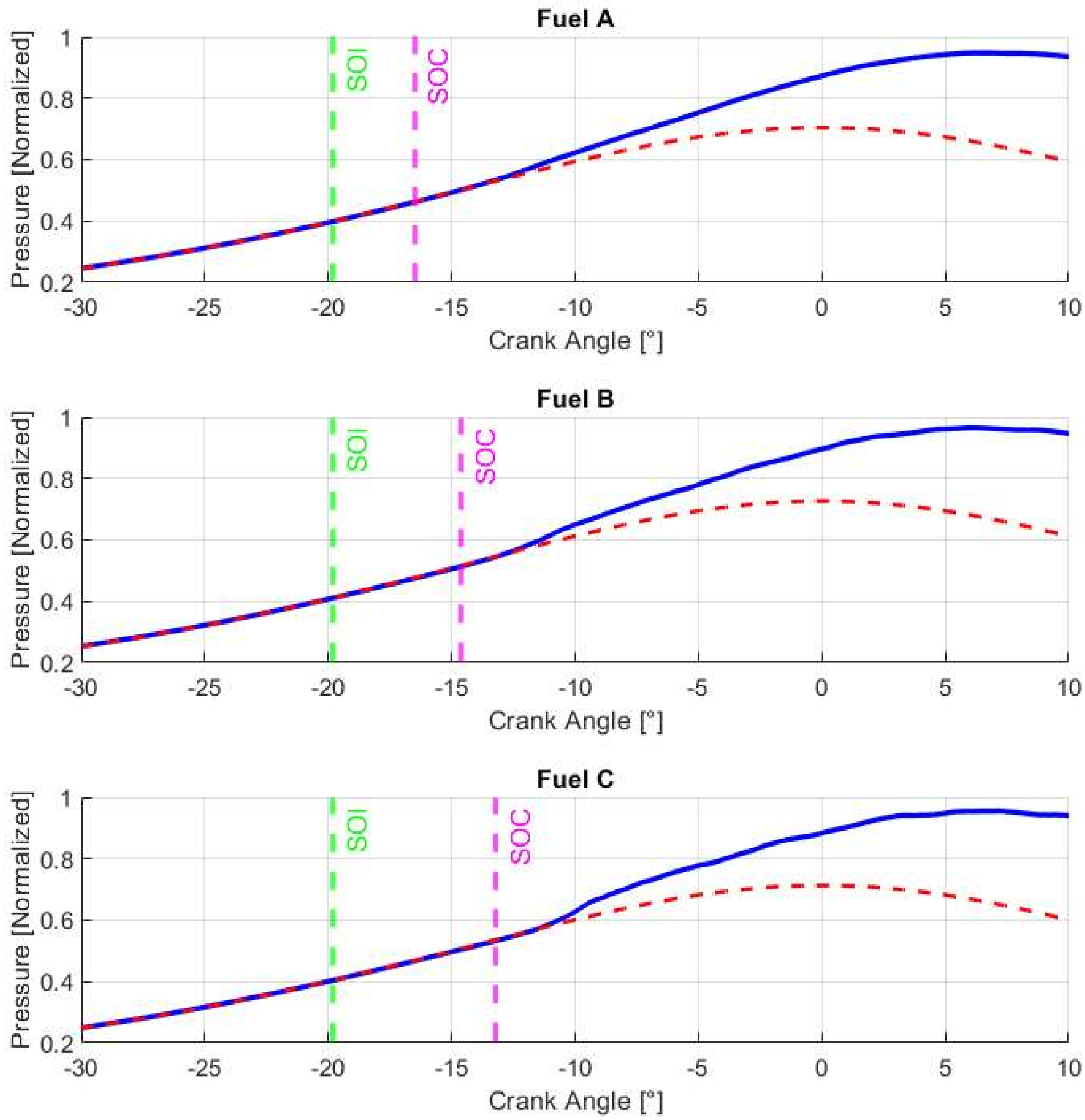

Figure 39: Comparison of Pressure Traces, 2500 rpm, 100% Load

(Blue: Measured Pressure, Red: Motored Pressure)

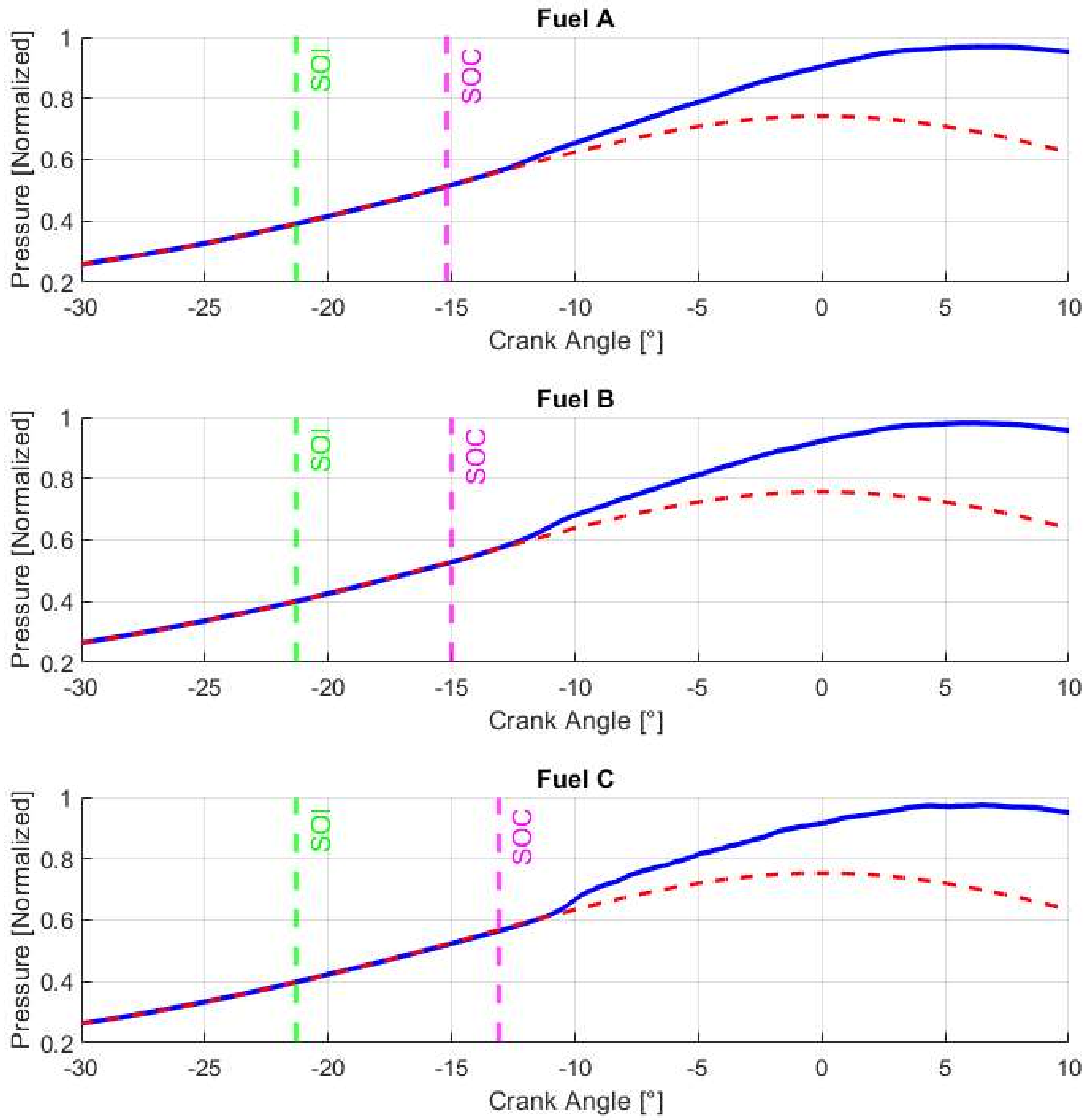

Figure 40: Comparison of Pressure Traces, 2800 rpm, 100% Load

(Blue: Measured Pressure, Red: Motored Pressure)

For both sets of pressure traces above, they appear to reach the same peak pressure, however, the pressure around -10° is slightly elevated for both Fuel B and C when compared to Fuel A. This increase in pressure at this location is hypothesized to cause the increased deformation observed during compression.

Regarding the increase in torque for Fuel B despite increased compression work, Fuel B does reach a marginally larger peak pressure value. This increase in peak pressure and pressure throughout the expansion stroke inherently must offset and overcome the increase in work during the compression stroke, resulting in a marginal 0.5% increase in torque output.

For a conclusion of this twist biasing discussion, initially it was found that at high-speeds, peak-to-peak twist values did not change with cetane rating at a similar rate as the maximum absolute twist values. It was hypothesized that this was due to a uniform shift in twist values, that was dependent on cetane rating in combination with engine speed. This was confirmed with Figure 37 and Figure 38. The cause for this twist biasing is suspected to be local increases in pressure before TDC in low-cetane fuels that are not present in Fuel A. These increases in pressure prior to TDC would result in more deformation during the compression causing twist biasing and an overall decrease in torque output due to increased compression work, all of which were observed for Fuel C. Additionally, a new low-cetane concern was presented, that being an uneven distribution of torque output across the cylinders. This was concluded based on the lack of negative deformation due to front-most cylinder combustion.

To determine if the increases of peak-to-peak twist at low-speed, high-load exceeds the maximum peak-to-peak twist present for Fuel A, Figure 41 is provided below.

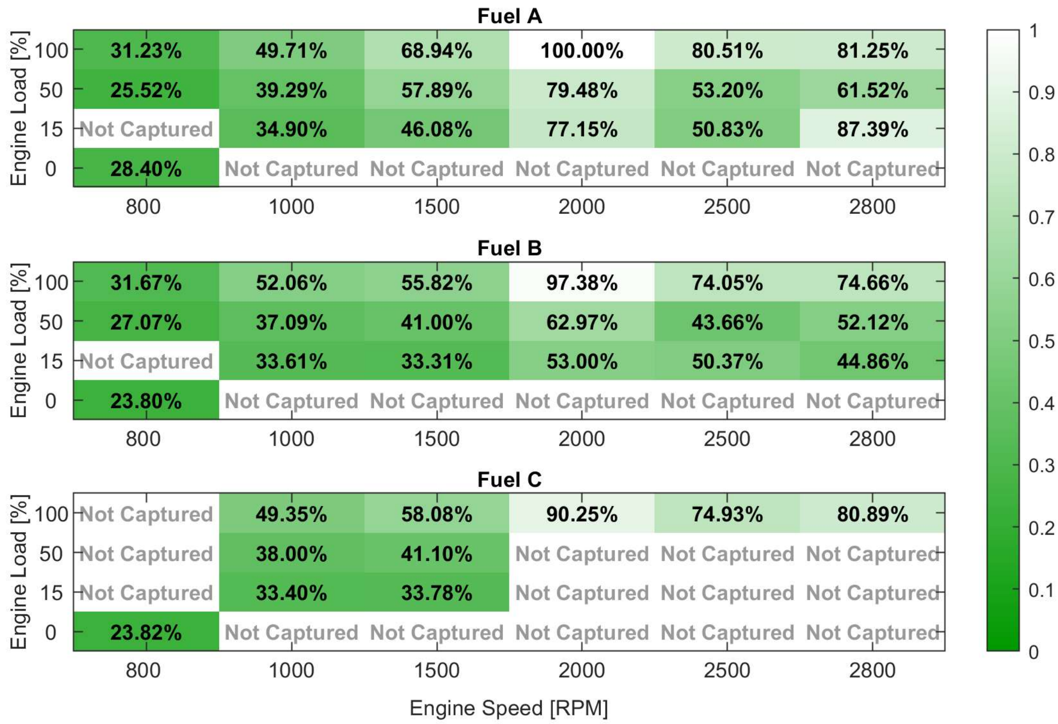

Figure 41: Max. P-P Twist, Normalized to Max. of Max. P-P twist of Fuel A

As seen in Figure 41 above, no cases for Fuel B or C exceed the maximum peak-to-peak twist present for Fuel A cases. Suggesting the cyclic strain range observed for low-cetane fuels does not exceed the maximum cyclic strain range observed in Fuel A.

From the results presented, it is concluded that peak-to-peak twist displays the same trends on the engine map as maximum absolute twist. Those trends consist of an increase with speed and a peak at 2000 RPM due to the resonance of the crankshaft. However, unlike maximum absolute twist, peak-to-peak twist only increased at low-speed, part to high-load conditions when compared to Fuel A values on a case-by-case basis. It's theorized that increases in ignition delay at high-speeds result in local pressure spikes that cause increased deformation during the compression stroke. This would allow for twist values to become biased in one direction, reducing peak-to-peak twist without necessarily affecting maximum absolute twist. Although some increases in peak-to-peak twist were observed, presenting a durability concern relative to their specific Fuel A counterparts, none of these increases resulted in a peak-to-peak twist that exceeded values recorded for Fuel A.

5.4 Maximum Absolute Rate of Crankshaft Twist

With absolute twist being proportional to strain as discussed prior, maximum absolute rate of twist is proportional to the rate of strain. Although the rate of strain is not relevant for the elastic deformation expected in the crankshaft [49] it will serve as an indicator of violence and vibration that the crank train is subjected to.

Maximum absolute rate of crankshaft twist was calculated using the gradient function in MATLAB, which utilizes the central difference method for determining the rate of change as shown in Equation 10 below, with ϕ and t being the measured twist and time respectively.

$$ROT_i = \left| \frac{\phi_{i+1} - \phi_{i-1}}{t_{i+1} - t_{i-1}} \right| \qquad [10]$$

The maximum value for each operating condition was determined for each fuel and used for the results presented in this section.

5.4.1 Maximum Rate of Crankshaft Twist Results

To begin analysis of absolute rate of crankshaft twist results, trends will be investigated and are presented in Figure 42 below.

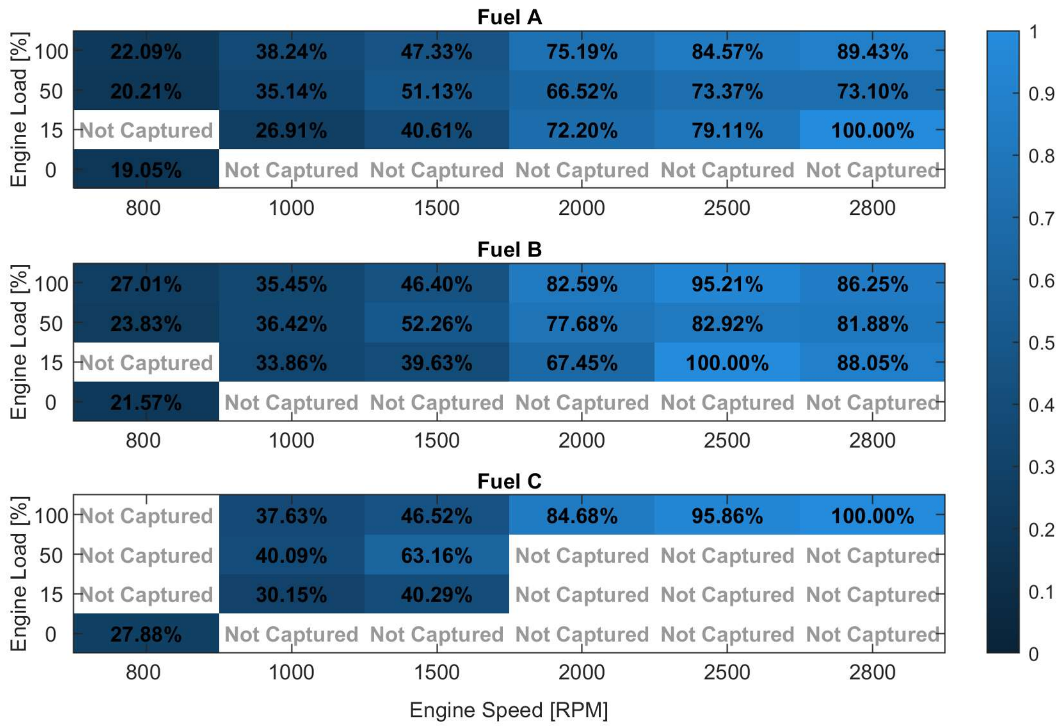

Figure 42: Trends of Rate of Crankshaft Twist

From above, rate of crankshaft twist shows a strong positive correlation with engine speed across all fuels. However, Fuel B differs from Fuel A in the specific locations of maximum rates of twist. Specifically, maximum rates of twist for Fuel A occur at high-speed, low-load conditions while maximum rates of twist for Fuel B occur at slightly lower speed and at both low and high loads. Additionally, the 1500 rpm, 50% load point appears to become more prominent as cetane rating is lowered. Regardless, general trends remain consistent as cetane rating is lowered. Interestingly, the rate of crankshaft twist does not seem to be affected by resonance.

To determine how the rate of twist changes on a case-by-case basis, maximum rate of twist results were normalized to their respective Fuel A counterparts and are presented below.

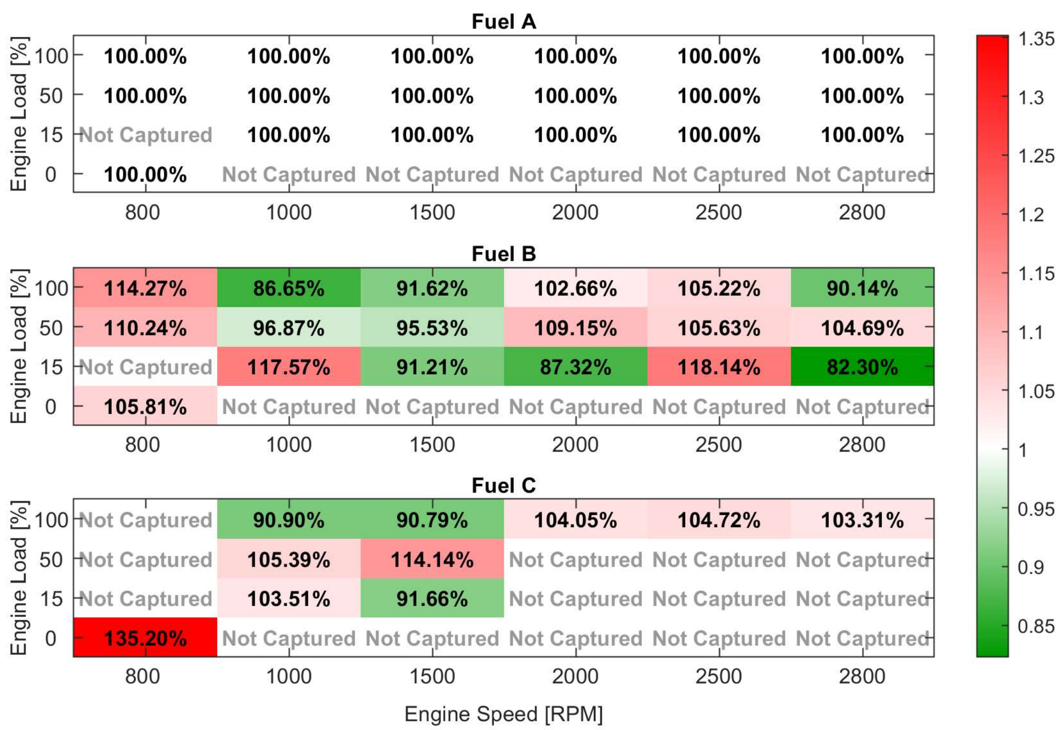

Figure 43: Changes in Rate of Crankshaft Twist when Compared to Fuel A Values

In contrast to the rate of twist magnitude shown previously in Figure 42, the change in maximum rate of crankshaft twist does not exhibit a strong correlation with engine speed or load, instead, the data is more scattered. However, rate of twist of the crankshaft tends to increase in select regions as the cetane rating is lowered. Suggesting that lower cetane fuels do increase the concern for these select regions. One notable finding is the non-consistent significance of idle between low-cetane fuels. For Fuel C, the change in rate of twist at idle is substantially higher than at any other measured operating point. However, while Fuel B shows an increase in the rate of twist at idle, it does not exceed neighboring points to the same extent and is not the global maximum.

To determine if the changes observed in Figure 43 result in rates of twist that exceed those present in Fuel A, Figure 44 is provided below.

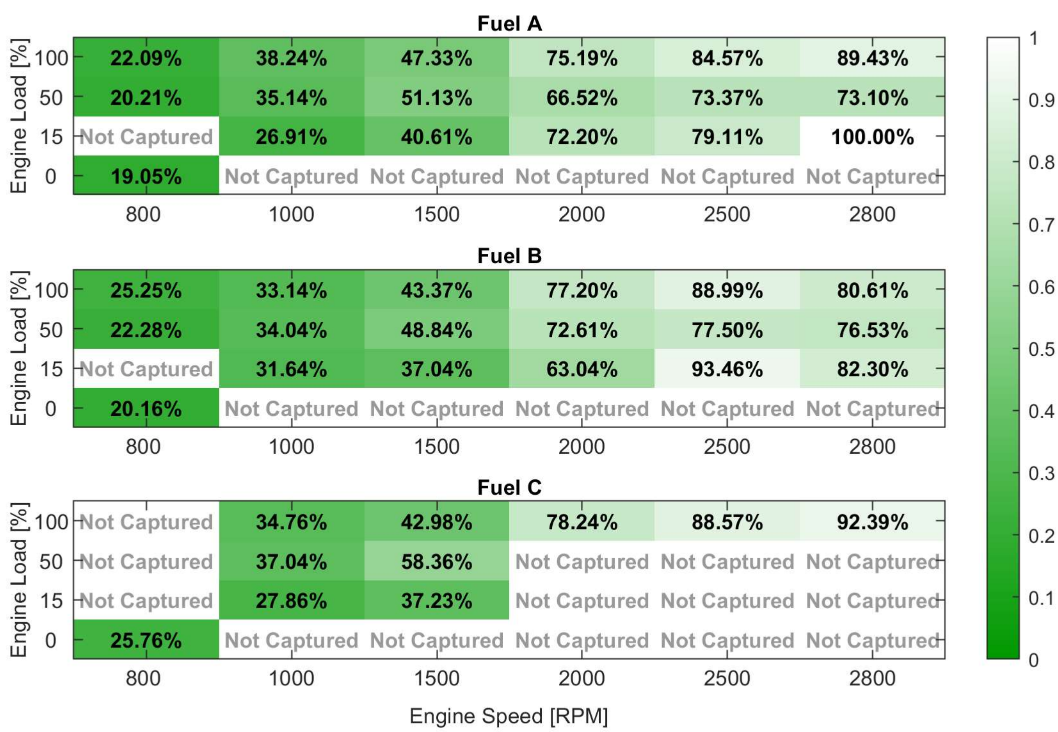

Figure 44: Rate of Crankshaft Twist, Normalized to Max. of Fuel A

Figure 44 above reveals that despite the rate of twist being increased in select regions as cetane rating is lowered, these changes did not result in a rate of twist that exceeded the global maximum value observed for Fuel A. Consistent with Figure 42, the maximum rate of twist slightly changes as cetane rating is lowered.

From the results presented, it can be concluded that the maximum rate of crankshaft twist has a strong relationship with engine speed, regardless of cetane rating and resonance. However, lower cetane fuels shifted the maximum crankshaft twist location on the engine map, but marginally, and did not affect the broader trend. Additionally, lower cetane fuels were found to increase the maximum rate of crankshaft twist, although somewhat sporadically with no definitive trend. Despite local increases in the rate of crankshaft twist between fuels, suggesting local increases in violence and vibration, no low-cetane values exceeded the maximum rate of crankshaft twist present in Fuel A.

Chapter 6 Composite Durability Indicator

To more completely understand the effects of low-cetane fuels on the durability of engine components, metrics previously discussed will be combined to create a Composite Durability Indicator. This final metric will be used to determine how much the durability concern has increased at each operating condition. The method used to determine this composite durability indicator is presented below.

$$CD\ Score = \frac{P_{Avg.Max} + PPRR_{Avg.} + \phi_{max.abs} + \phi_{max.P-P} + \frac{d\phi}{dt}_{max}}{5} \qquad [11]$$

All values input into Equation 11 were normalized according the inter-fuel global normalized method for their respective metric prior to being added. This was done to purely display percent increases and not have metrics with inherently larger values overshadow others. Additionally, the resulting total of all normalized values was divided by five to provide a more intuitive result that from which percentage changes could easily be determined. This results in durability possibly ranging from zero to one for Fuel A and scores beyond one only being possible for cases of Fuel B or C that exceed the maximum durability score of Fuel A.

6.1 Composite Durability Scores

Beginning in the same manner as in previous sections, first, trends will be examined and discussed. Trends of the durability score are presented below in Figure 45.

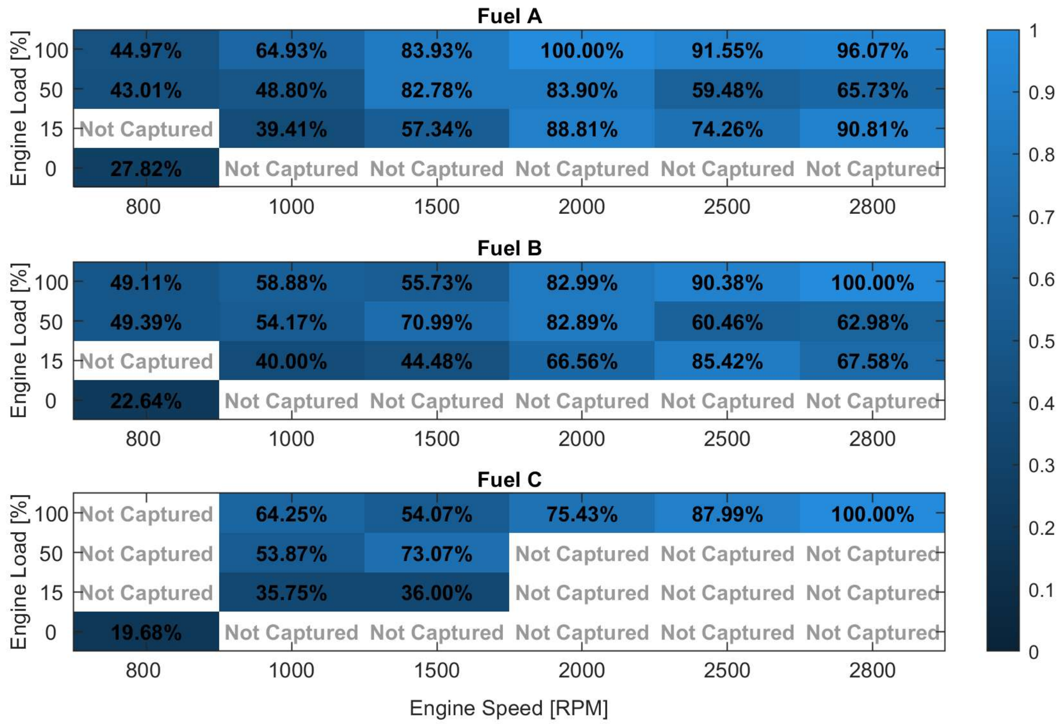

Figure 45: Trends of Durability Score

From above, trends pertaining to the location of most concern cases remain broadly consistent between fuels, that being more concerning at high-speed, high-load conditions. However, as cetane rating is reduced the location of the most concerning case deviates. The most concerning point for Fuel B and C being at 2800 RPM, 100% load, compared to Fuel ’s being at 2000 RPM, 100% load. Additionally, low-speed conditions appear to become more significant compared to the peak concern for low-cetane fuels. These changes are more effectively displayed in Figure 46 below.

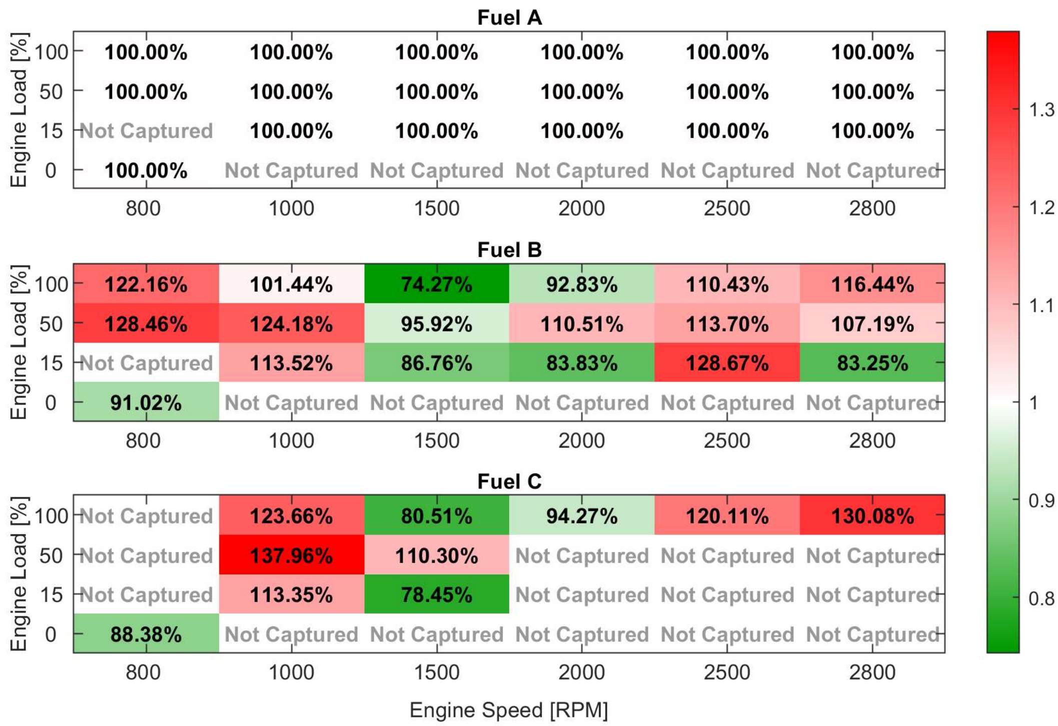

Figure 46: Change in Durability Score when Compared to Fuel A Values

From Figure 46 above, it can be seen that as cetane rating is lowered, concern noticeably increases, specifically at high and low-speed conditions. Values at low-speed and part-to-high-load conditions for Fuel B show up to a 28% increase in durability concern. Fuel C values at this condition are predicted to show even greater concern, however, due to the lack of collected twist data for Fuel C, an accurate durability score could not be calculated. To determine if these increases in durability score resulted in operating conditions that exceeded the maximum durability score of Fuel A, Figure 47 is provided below.

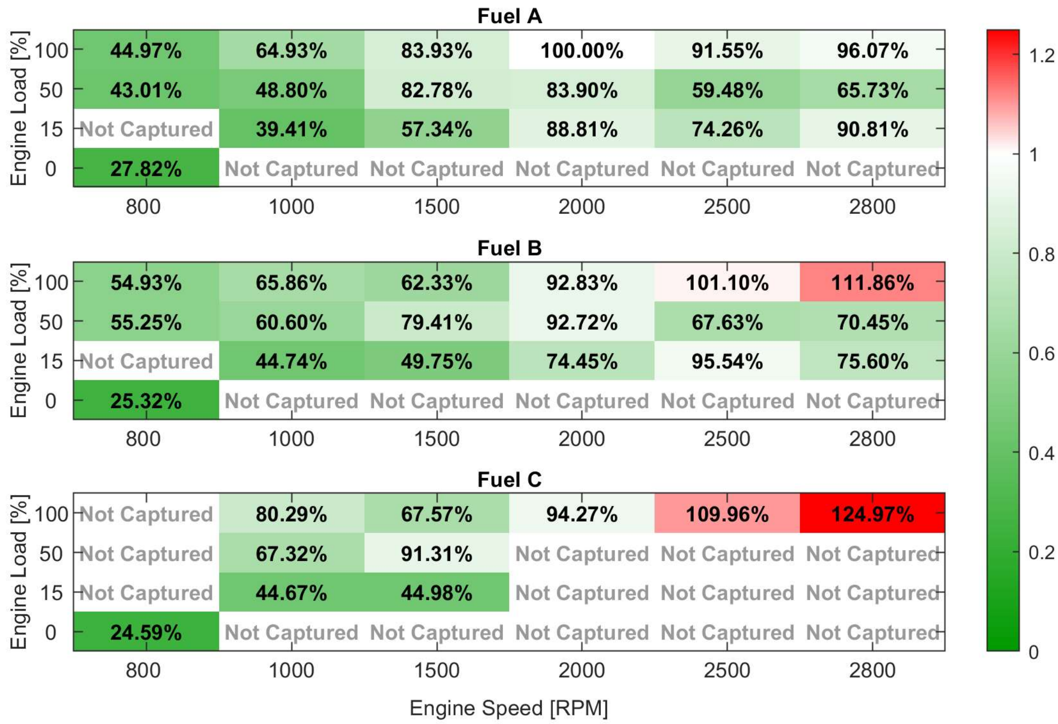

Figure 47: Durability Score

Figure 47 provides the calculated durability score, providing insight into the most concerning operating conditions. As discussed previously, the location of greatest concern shifts from 2000 rpm, 100% load for Fuel A to 2800 rpm, 100% load for Fuels B and C. Furthermore, the concern for Fuels B and C is reduced at the 2000 rpm, 100% load condition compared to Fuel A. At low-speed conditions, although low-cetane fuels presented a relative increase in concern, this increases was not enough to exceed the greatest concern present for Fuel A. Consulting metrics individually, average peak pressure appears to be a strong indicator of durability concern. Initially, average peak pressure values, normalized to the global maximum of Fuel A, appear to be a viable indicator of durability. However, upon further analysis, average peak pressure does not display the same in maximum durability concern for Fuel A, being shifted up by 800 rpm for average peak pressure. Additionally, average peak pressure does not display the same elevated values leading up to high-speed, high-load conditions. This can be seen more clearly in a correlation between the average peak pressure and durability score presented below.

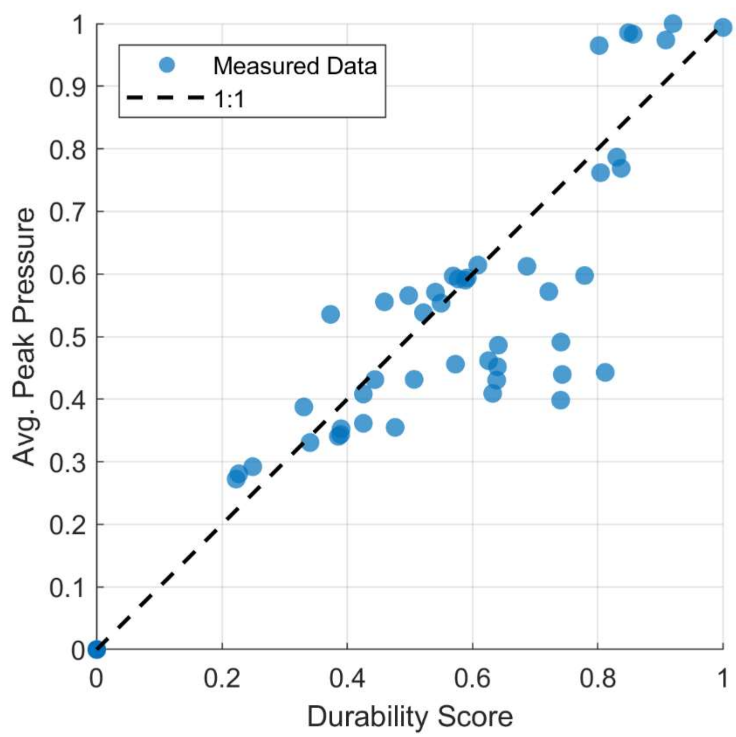

Figure 48: Avg. Peak Pressure to Durability Score Correlation

From Figure 48, it can be seen that average peak pressure overpredicts the greatest durability concerns while underpredicting intermediate concerns. This exemplifies how durability concerns arise from a multitude of factors, encouraging the use of a Composite Durability Indicator.

Results from the Composite Durability Indicator help to show what regions of the engine map present the most concern, that being high-speed conditions at high load, as well as how these regions shift as cetane rating is lowered. Fuel B and C showed a shift of the most concerning case up 800 rpm relative to Fuel A, from 2000 rpm to 2800 rpm. Additionally, the durability scores were shown to increase at most operating conditions, increasing to the greatest extent when compared to their Fuel A counterparts at low-speed conditions. However, these increases at low speed were not enough to exceed the global maximum durability score of Fuel A for both Fuel B and C. Although increases at high-speed, high-load conditions did exceed the global maximum of Fuel A, with Fuel C displaying greater concerns relative to Fuel B. Average peak pressure was found to be a useful predictor of most concerning conditions determined by the durability score. However, average peak pressure underpredicted intermediate durability concerns. This highlights the usefulness of the composite durability indicator as it combines multiple indicators to provide a more thorough prediction of durability concerns.

Chapter 7 Conclusion

Results were presented with a three-tiered normalization approach: 1) metric normalized to the maximum value for each respective fuel, (2) metric normalized to the corresponding Fuel A value on a case-by-case basis, and (3) metric normalized to the maximum Fuel A value across all conditions. These normalizations were selected to highlight different aspects of low-cetane effects. Values obtained from the third method were also used in the Composite Durability Indicator.

Utilizing this indicator, the locations of greatest ignition delay with respect to time and crank angle were determined, low and high-speed conditions respectively. Additionally, increases in ignition delay with respect to time and crank angle were observed across all conditions. However, these increases only led to ignition delay exceeding the global maximum Fuel A values with respect to time and crank angle at low-speed and high-speed conditions respectively.

For average peak pressure, first it was determined low-cetane fuels do not affect the relationship between peak pressure and speed and load. All fuels displayed that peak pressure has a strong positive correlation with both speed and load regardless of cetane rating. Additionally, peak cylinder pressures tended to increase across most operating conditions, only decreasing due to excessive ignition delay. This suggested local increases in the durability concern. However, these increases in peak pressure for low-cetane fuels only exceeded the maximum peak pressure recorded for Fuel A at high-speed, high-load cases.

From results shown for PPRR, it was concluded that lowering the cetane rating of the fuel used did have an impact on the speed and load at which the greatest PPRR occurred. Both Fuel B and C shifted the location of maximum PPRR to part-speed, part-load conditions as opposed to high-speed, low-load conditions as seen for Fuel A. Additionally, PPRR increased across a majority of operating conditions, only reducing at idle for Fuel B and at a few points for Fuel C, including the excessive ignition delay condition, 2000 RPM, 50% load. This suggested an increase in durability concern for most cases on a case-by-case basis. However, these increases resulted in PPRR values that exceeded the maximum value observed for Fuel A more sporadically, with a band of increased PPRR around the step timing control shift region.

To begin the crankshaft twist discussion, limitations of the measurement were discussed, followed by analysis of maximum absolute twist, signifying stress within the crankshaft. The resonant frequency of the crankshaft was excited in the speed range tested and each fuel displayed an increase in maximum absolute twist in this region. However, the dynamic amplification at resonance is believed to have masked low-cetane effects as increases in maximum absolute twist when compared to Fuel A on a case-by-case basis were only shown outside of the resonance region. With knowledge of the resonance location, its notable that the maximum absolute twist for Fuel C occurred outside of this region, at a high-speed, high-load condition, a region thought to not be affected by low-cetane fuels [17][20][24]. Additionally, this condition was not outstanding for Fuel A. Despite increases on a case-by-case basis, maximum absolute twist values for Fuels B and C never exceeded the maximum value present for Fuel A across all conditions.

Peak-to-peak twist results, signifying cyclic strain range, displayed the same trends on the engine map as maximum absolute twist. Those trends consisted of an increase with speed and a peak at 2000 RPM due to the resonance of the crankshaft. However, unlike maximum absolute twist, peak-to-peak twist only increased at low-speed, part to high-load conditions when compared to Fuel A values on a case-by-case basis. It's theorized that increases in ignition delay at high-speeds result in local pressure spikes that cause increased deformation during the compression stroke. This would cause twist values to become biased in one direction, reducing peak-to-peak twist without necessarily affecting maximum absolute twist. Although some increases in peak-to-peak twist were observed, presenting a durability concern relative to their specific Fuel A counterparts, none of these increases resulted in a peak-to-peak twist that exceeded values recorded for Fuel A.

Maximum rate of crankshaft twist results, signifying violence and vibration, showed a strong relationship with engine speed, regardless of cetane rating and resonance. However, lower cetane fuels shifted the maximum crankshaft twist location on the engine map, but marginally, and did not affect the broader trend. Additionally, lower cetane fuels were found to increase the maximum rate of crankshaft twist, although somewhat sporadically with no definitive trend. Despite local increases in the rate of crankshaft twist between fuels, suggesting local increases in violence and vibration, no low-cetane values exceeded the maximum rate of crankshaft twist present in Fuel A.

All metrics were then combined into a Composite Durability Indicator. Initial this indicator was used to determine what regions of the engine map present the most concern, that being high-speed conditions at high load, as well as how these regions shift as cetane rating is lowered. Fuel B and C showed a shift of the most concerning case up 800 rpm relative to Fuel A, from 2000 rpm to 2800 rpm. Additionally, the durability scores were shown to increase at most operating conditions, increasing to the greatest extent when compared to their Fuel A counterparts at low-speed conditions. However, these increases at low speed were not enough to exceed the global maximum durability score of Fuel A for both Fuel B and C. Although increases at high-speed, high-load conditions did exceed the global maximum of Fuel A, with Fuel C displaying greater concerns relative to Fuel B. Average peak pressure was found to be a useful predictor of most concerning conditions determined by the durability score. However, average peak pressure underpredicted intermediate durability concerns. This highlighted the usefulness of the composite durability indicator as it combines multiple indicators to provide a more thorough prediction of durability concerns.

Chapter 8 Future Work

Future work considerations include adjusting what data was collected, adjusting the composite durability indicator to account for metrics that may be determined to be better indicators of durability effects, and further investigation into twist biasing..

To begin with the adjustments to what data was collected, simply collecting the remaining points for Fuel C would help to obtain a better understanding of how durability concerns change as cetane rating is reduced.

Additionally, the number of metrics collected could be altered. Specifically, the metrics chosen for this research strictly pertain to internal engine components. Future work could investigate including metrics pertaining to durability outside of the engine. For instance, for engines that have forced induction through the means of turbocharger, it may be advantageous to consider metrics such as exhaust gas temperatures, burn rates, or soot production. Similar metrics may be useful for engines with aftertreatment systems as well.

An additional adjustment to the Composite Durability Concern could be made with respect to weighting. Depending on the metrics used or if the durability concern of interior or exterior components is needed to determine, it may be ideal to add weighting factors to for each metric. This will help to adjust the composite durability indicator to fit any engine based on the weakest link in the system. For example, for a single cylinder engine, crankshaft twist may not be as great of a concern when compared to a multi-cylinder inline engine. Reducing the weight of crankshaft twist metrics could account for this reduction in concern and produce more applicable results.

Finally, twist biasing was briefly discussed in Section 5.3.1. Further research and analysis should be conducted as the results shown indicate significant low-cetane effects at high-speed, high-load conditions. These results present a significant addition to the previously concluded effects low-cetane fuels [17][20][24]. Further research should be undertaken to fully understand the effects of low-cetane fuels on crankshaft dynamics.

References

[1] V. Ram and S. R. Salkuti, "An overview of major synthetic fuels," Energies, vol. 16, no. 6, p. 2834, 2023, doi: 10.3390/en16062834.

[2] T. Białecki, "Mathematical model of the combustion process for turbojet engine based on fuel properties," Int. J. Energy Environ. Eng., vol. 13, no. 4, pp. 1235–1247, 2022, doi: 10.1007/s40095-022-00489-2.

[3] K. Kim, P. Wiersema, J. I. Ryu, W. Lee, K. Min, E. Mayhew, J. Temme, C.-B. M. Kweon, and T. Lee, "Experimental and data-driven chemical kinetic modeling study of alcohol-to-jet (ATJ) synthetic biofuel for sustainable aviation fuels," Fuel, vol. 368, Art. no. 131630, Jul. 2024, doi: 10.1016/j.fuel.2024.131630.

[4] J. M. Ngũgĩ, S. Richter, M. Braun-Unkhoff, C. Naumann, and U. Riedel, "A study on fundamental combustion properties of oxymethylene ether-1, the primary reference fuel 90, and their blend: Experiments and modeling," Combustion and Flame, vol. 243, p. 111996, 2022, doi: 10.1016/j.combustflame.2022.111996.

[5] V. Okoro, U. Azimov, and J. Munoz, "Recent advances in production of bioenergy carrying molecules, microbial fuels, and fuel design – A review," Fuel, vol. 316, p. 123330, 2022, doi: 10.1016/j.fuel.2022.123330.

[6] K. Chalastras and C. Anastasiou, "The German synthetic fuel effort: Origins, development, and legacy," Historia Scripta, May 15, 2025. [Online]. Available: https://www.historiascripta.org/modern-era/the-german-synthetic-fuel-effort-origins-development-and-legacy/ [Accessed: Oct. 15, 2025].

[7] D. H. Chun, G. B. Rhim, M. H. Youn, et al., "Brief review of precipitated iron-based catalysts for low-temperature Fischer–Tropsch synthesis," Topics in Catalysis, vol. 63, pp. 793–809, 2020, doi: 10.1007/s11244-020-01336-6.

[8] R. G. dos Santos and A. C. Alencar, "Biomass-derived syngas production via gasification process and its catalytic conversion into fuels by Fischer Tropsch synthesis: A review," Int. J. Hydrogen Energy, vol. 45, no. 36, pp. 18114–18132, 2020, doi: 10.1016/j.ijhydene.2019.07.133.

[9] P. K. Gupta, V. Kumar, and S. Maity, "Renewable fuels from different carbonaceous feedstocks: a sustainable route through Fischer–Tropsch synthesis," Journal of Chemical Technology and Biotechnology, vol. 96, no. 4, pp. 853–868, 2021, doi: 10.1002/jctb.6644.

[10] LEC Partners, "Synthetic Diesel," LEC Partners, 2024. [Online]. Available: https://lee-enterprises.com/synthetic-diesel/. [Accessed: Oct. 15, 2025].

[11] N. Dunford, Diesel Fuels Derived from Renewable Sources, Oklahoma State University Extension Fact Sheet FAPC 177, Jul. 2019.

[12] U.S. Department of Energy, "Sustainable Aviation Fuel," Alternative Fuels Data Center, [Online]. Available: https://afdc.energy.gov/fuels/sustainable-aviation-fuel [Accessed: Oct. 15, 2025].

[13] "Alcohol to Jet Fuel: What You Need to Know," ResourceWise – Sustainability Blog, Prima Markets / ResourceWise, Apr. 5, 2023. [Online]. Available: https://www.resourcewise.com/blog/environmental-blog/alcohol-to-jet-fuel-what-you-need-to-know [Accessed: Oct. 15, 2025].

[14] R. Marsh and L. Hudson, "Next-Generation SAF by LanzaJet and IAG," LanzaJet News & Insights, Jan. 15, 2025. [Online]. Available: https://www.lanzajet.com/news-insights/next-generation-saf-by-lanzajet-and-iag [Accessed: Oct. 20, 2025].

[15] P. Shah, "ATJ offers viable pathway to increased SAF production," Oil & Gas Journal, Jan. 16, 2024. [Online]. Available: https://www.ogj.com/refining-processing/article/14303748/atj-offers-viable-pathway-to-increased-saf-production [Accessed: Oct. 20, 2025].

[16] A. Karmakar, S. Karmakar, and S. Mukherjee, "Properties of various plants and animals feedstocks for biodiesel production," Bioresource Technology, vol. 101, no. 19, pp. 7201–7210, 2010, doi: 10.1016/j.biortech.2010.04.079.

[17] P. Schihl, L. Hoogterp-Decker, and E. Gingrich, "The ignition behavior of a coal to liquid Fischer-Tropsch jet fuel in a military relevant single cylinder diesel engine," SAE Int. J. Fuels Lubr., vol. 5, no. 2, pp. 785–802, 2012, doi: 10.4271/2012-01-1197.

[18] P. Schihl, E. Gingrich, and L. Decker, "The combustion and ignition characteristics of varying blend ratios of JP-8 and a coal to liquid Fischer-Tropsch jet fuel in a military relevant single cylinder diesel engine," SAE Int. J. Fuels Lubr., vol. 8, no. 2, pp. 501–514, 2015, doi: 10.4271/2015-01-9073.

[19] M. Tess, M. Kurman, and C. Kweon, "Spray characterization and ignition delay measurements of JP-8 and IPK in a constant-pressure flow chamber," SAE Int. J. Engines, vol. 9, no. 2, pp. 899–909, 2016, doi: 10.4271/2016-01-0736.

[20] Y. Kidoguchi, C. Yang, and K. Miwa, "Effects of fuel properties on combustion and emission characteristics of a direct-injection diesel engine," SAE Technical Paper 2000-01-1851, 2000, doi: 10.4271/2000-01-1851.

[21] D. A. Rothamer and L. Murphy, "Systematic study of ignition delay for jet fuels and diesel fuel in a heavy-duty diesel engine," Proc. Combust. Inst., vol. 34, no. 2, pp. 3021–3029, 2013, doi: 10.1016/j.proci.2012.06.085.

[22] J. B. Heywood, Internal Combustion Engine Fundamentals, 2nd ed. New York, NY, USA: McGraw-Hill, 2018.

[23] Detail Specification: Turbine Fuel, Aviation, Kerosene Type, JP-8 (NATO F-34), NATO F-35, and JP-8+100 (NATO F-37), MIL-DTL-83133K, U.S. Department of Defense, Jul. 2018.

[24] C. Wong and D. Steere, "The effects of diesel fuel properties and engine operating conditions on ignition delay," SAE Technical Paper 821231, 1982, doi: 10.4271/821231.

[25] M. Tess, E. Gingrich, S. Stoll, “Combustion Strategies for Low-Cetane Fuels”, In Proceedings of the Ground Vehicle Systems Engineering and Technology Symposium (GVSETS), NDIA, Novi, MI, Aug. 13-15, 2019.

[26] T. Dickerson, A. McDaniel, S. Williams, D. Luning-Prak, et al., "Start-up and steady-state performance of a new renewable alcohol-to-jet (ATJ) fuel in multiple diesel engines," SAE Technical Paper 2015-01-0901, 2015.

[27] C. Nerubenko and G. Nerubenko, "Self-tuning twistal vibration dampers for V8 engines," SAE Technical Paper 2017-01-1819, 2017, doi: 10.4271/2017-01-1819.

[28] L. Du, F. Yang, Y. Hu, and L. Xu, "Active damping control of twistal vibration in a diesel hybrid powertrain," SAE Technical Paper 2019-01-2342, 2019, doi: 10.4271/2019-01-2342.

[29] H. Ashouri, B. Beheshti, and M. R. Ebrahimzadeh, "Analysis of fatigue cracks of cylinder heads in diesel engines," J. Theoret. Appl. Mech., vol. 54, no. 2, pp. 369–383, 2016, doi: 10.15632/jtam-pl.54.2.369.

[30] P. Mahajan, R. Bodake, and A. Thakur, "Optimization of scallop design for cylinder head of a multi-cylinder diesel engine for reduction of combustion deck temperatures and simultaneously enhancing combustion deck fatigue margin," SAE Technical Paper 2021-01-1233, 2021, doi: 10.4271/2021-01-1233.

[31] X. Wang, J. Duan, and J. Sun, "The influence of IC engine working condition on the lubrication characteristics of piston ring," SAE Technical Paper 2019-01-0591, 2019, doi: 10.4271/2019-01-0591.

[32] M. Groendyk and D. Rothamer, "Effects of fuel physical properties on auto-ignition characteristics in a heavy duty compression ignition engine," SAE Int. J. Fuels Lubr., vol. 8, no. 1, 2015, doi: 10.4271/2015-01-0952.

[33] Boston University, "Mechanics of Materials: Twist," Mechanics of Slender Structures, Boston University, n.d. [Online]. Available: https://www.bu.edu/moss/mechanics-of-materials-twist/. [Accessed: Feb. 4, 2026].

[34] E. Vitz, J. W. Moore, J. Shorb, X. Prat-Resina, T. Wendorff, and A. Hahn, "Gay-Lussac’s Law – The Relationship Between Pressure and Temperature," LibreTexts Chemistry, n.d. [Online]. Available: https://chem.libretexts.org/Courses/Saint_Francis_University/CHEM_113%3A_Human_Chemistry_I_(Muino)/08%3A_Gases_Liquids_and_Solids/8.07%3A_Gay-

Lussac%27s_Law-_The_Relationship_Between_Pressure_and_Temperature. [Accessed: Feb. 18, 2026].

[35] K. Vora and B. Ghosh, "Vibration due to piston slap and combustion in gasoline and diesel engines," SAE Technical Paper 911060, 1991, doi: 10.4271/911060.

[36] D. Hosny and R. Young, "A system approach for the assessment of cavitation corrosion damage of cylinder liners in internal combustion engines," SAE Technical Paper 930581, 1993, doi: 10.4271/930581.

[37] G. Glyniadakis, M. D'Agostini, and M. Casagrande, "Liner vibration and cavitation," SAE Technical Paper 2006-01-2512, 2006, doi: 10.4271/2006-01-2512.

[38] V. Demarchi and F. Windlin, "Cavitation erosion on cylinder liners," SAE Technical Paper 952250, 1995, doi: 10.4271/952250.

[39] G. Green and R. Engelstad, "A technique for the analysis of cylinder liner vibrations and cavitation," SAE Technical Paper 930582, 1993, doi: 10.4271/930582.

[40] A. Jaipuria, P. Lakshminarayanan, A. Khan, and D. Sarmah, "Crankshaft peak firing pressure bearing capability enhancement," SAE Int. J. Fuels Lubr., vol. 3, no. 2, pp. 322–335, 2010, doi: 10.4271/2010-01-1527.\

[41] P. Lakshminarayanan, S. Stephen, A. Dani, K. Kale, et al., "Design and development of a torsional vibration rubber damper," SAE Technical Paper 990023, 1999, doi: 10.4271/990023.

[42] M. Ukhande, R. Mane, and G. Shegavi, "Optimization of crankshaft torsional rigidity for fatigue strength improvement using CAE," SAE Technical Paper 2012-01-0404, 2012, doi: 10.4271/2012-01-0404.

[43] A. Londhe and V. Yadav, "Design and optimization of crankshaft torsional vibration damper for a 4-cylinder 4-stroke engine," SAE Technical Paper 2008-01-1213, 2008, doi: 10.4271/2008-01-1213.

[44] M. Fonte, B. Li, L. Reis, and M. Freitas, "Crankshaft failure analysis of a motor vehicle," Eng. Failure Anal., vol. 35, pp. 147–152, 2013.

[45] A. Ktari, N. Haddar, and H. F. Ayedi, "Fatigue fracture expertise of train engine crankshafts," Eng. Failure Anal., vol. 18, no. 3, pp. 1085–1093, 2011, doi: 10.1016/j.engfailanal.2011.02.007.

[46] Ö. Karakas, "Consideration of mean-stress effects on fatigue life of welded magnesium joints by the application of the Smith–Watson–Topper and reference radius concepts," Int. J. Fatigue, vol. 49, pp. 1–17, Apr. 2013, doi: 10.1016/j.ijfatigue.2012.11.007.

[47] S. S. K. Singh and S. Abdullah, "Effects of mean stress on the durability assessment for an automobile crankshaft using Markov chain modelling technique," J. Mech. Eng., vol. SI 7, no. 1, pp. 19–28, Nov. 2018.

[48] S. S. Shinde, C. S. Pathak, and M. Ukhande, "Fatigue life assessment of crankshaft under bending and torsional loading," Int. J. Eng. Res. Technol. (IJERT), vol. 2, no. 11, pp. 1–6, Nov. 2013.

[49] P. P. Urone and R. Hinrichs, "Hooke's law: Stress and strain revisited," in College Physics 2e, 2nd ed. Houston, TX, USA: OpenStax, 2015. [Online]. Available: https://openstax.org/details/books/college-physics-2e.

[50] D. Woodyard, "Chapter One – Theory and general principles," in Pounder's Marine Diesel Engines and Gas Turbines, 9th ed., 2009, pp. 1–40, doi: 10.1016/B978-0-7506-8984-7.00001-1.

[51] S. Gopujkar, J. Worm, and D. Robinette, "Methods of pegging cylinder pressure to maximize data quality," SAE Technical Paper 2019-01-0721, 2019, doi: 10.4271/2019-01-0721.

[52] M. Tess, D. Kowalski, J. Piehl, and N. Hubble, "Durability effects of low-cetane fuels on military diesel engines – Phase I: Cummins VTA903 initial risk assessment," presented at GVSC Tech Talk, Mar. 2026.

[53] T. Feese and G. Beshouri, "Engine crankshaft failures due to torsional natural frequency excited by dual fuel operation," in Proceedings of the Torsional Vibration Symposium, Engineering Dynamics Incorporated, San Antonio, TX, USA, 2017.

Appendix

Pressure Traces and Ignition Delay Calculations

Fuel A

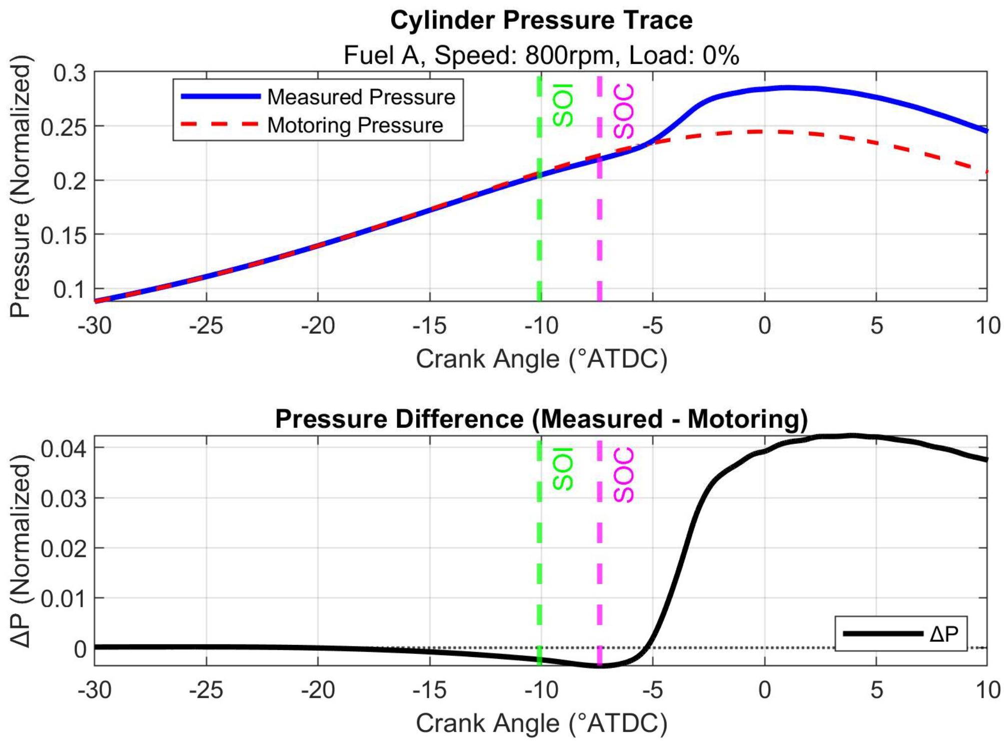
Cylinder Pressure Trace
Fuel A, Speed: 800rpm, Load: 0%
Pressure (Normalized)
Measured Pressure
Motoring Pressure
SOI
SOC
0.3
0.25
0.2
0.15
0.1
-30
-25
-20
-15
-10
-5
0
5
10
Crank Angle (°ATDC)
Pressure Difference (Measured - Motoring)
ΔP (Normalized)
SOI
SOC
ΔP
0.04
0.03
0.02
0.01
0
-30
-25
-20
-15
-10
-5
0
5
10
Crank Angle (°ATDC)

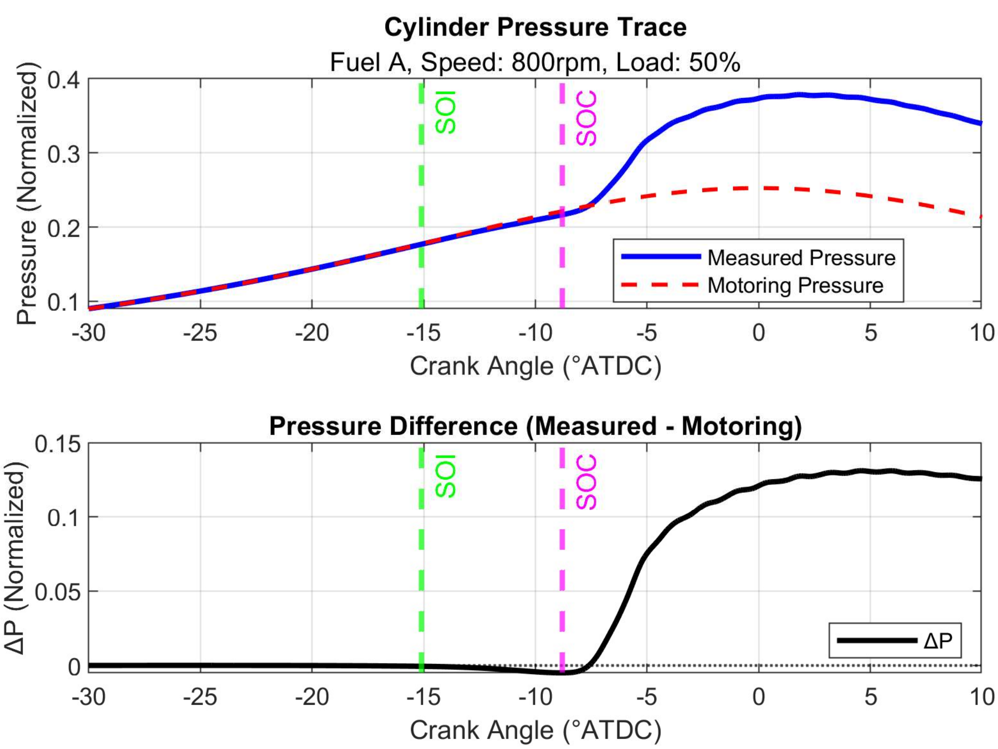
Cylinder Pressure Trace
Fuel A, Speed: 800rpm, Load: 50%
Pressure (Normalized)
SOI
SOC
Measured Pressure
Motoring Pressure
0.4
0.3
0.2
0.1
-30
-25
-20
-15
-10
-5
0
5
10
Crank Angle (°ATDC)
Pressure Difference (Measured - Motoring)
ΔP (Normalized)
SOI
SOC
ΔP
0.15
0.1
0.05
0
-30
-25
-20
-15
-10
-5
0
5
10
Crank Angle (°ATDC)

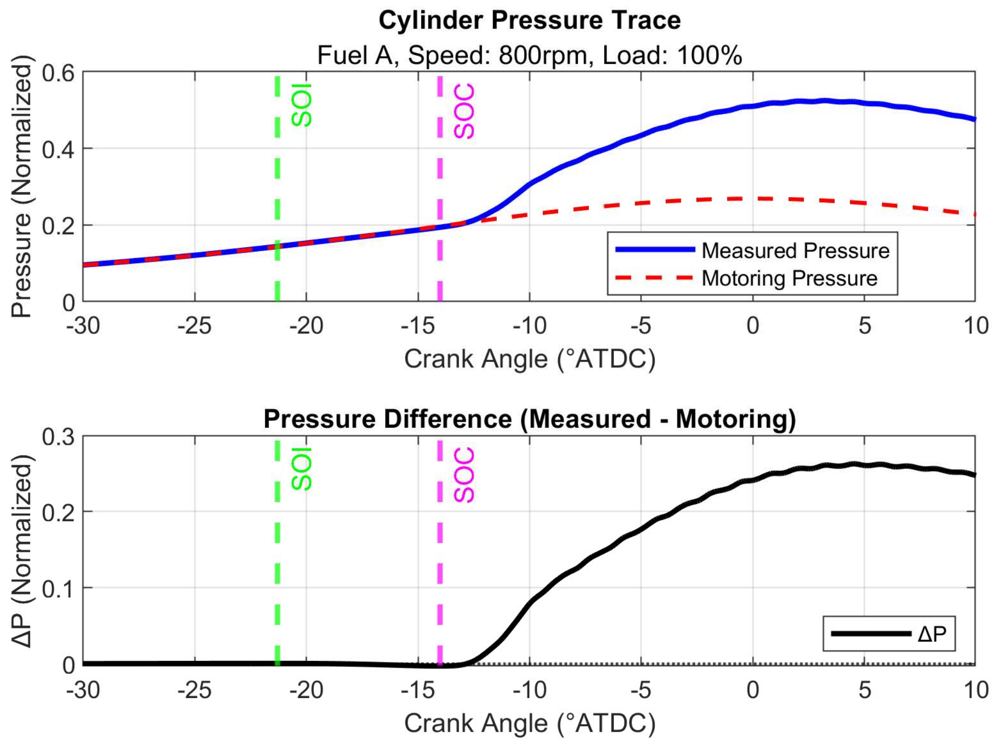
Cylinder Pressure Trace
Fuel A, Speed: 800rpm, Load: 100%
Pressure (Normalized)
0.6
0.4
0.2
0
SOI
SOC
Measured Pressure
Motoring Pressure
-30
-25
-20
-15
-10
-5
0
5
10
Crank Angle (°ATDC)
Pressure Difference (Measured - Motoring)
ΔP (Normalized)
0.3
0.2
0.1
0
SOI
SOC
ΔP
-30
-25
-20
-15
-10
-5
0
5
10
Crank Angle (°ATDC)

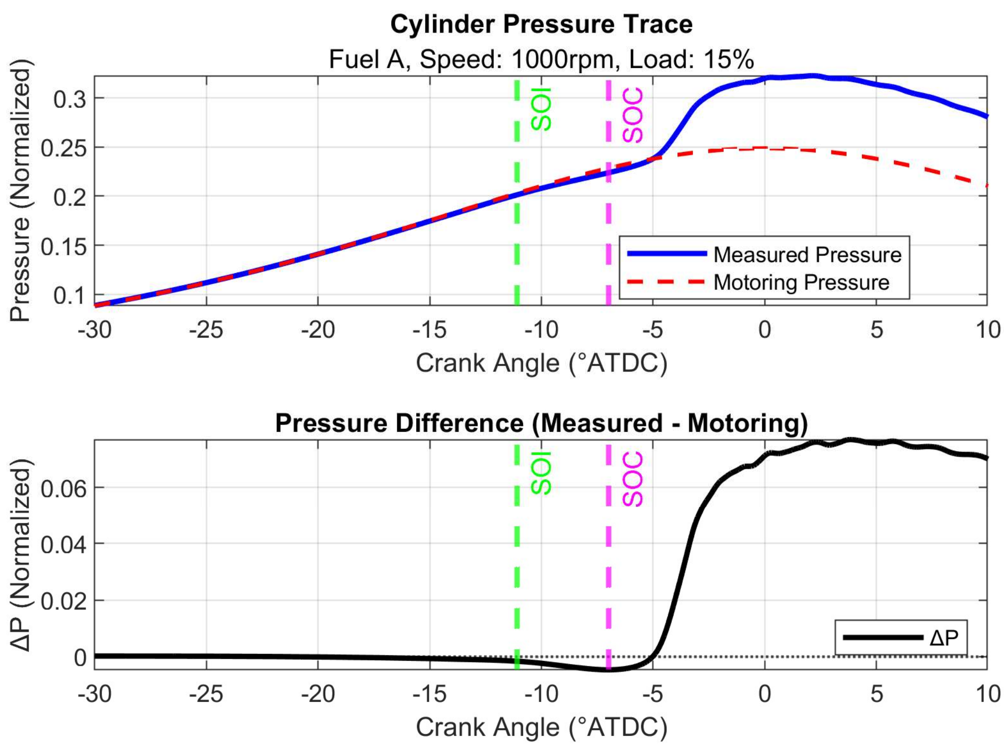
Cylinder Pressure Trace
Fuel A, Speed: 1000rpm, Load: 15%
Pressure (Normalized)
0.3
0.25
0.2
0.15
0.1
SOI
SOC
Measured Pressure
Motoring Pressure
-30
-25
-20
-15
-10
-5
0
5
10
Crank Angle (°ATDC)
Pressure Difference (Measured - Motoring)
ΔP (Normalized)
0.06
0.04
0.02
0
SOI
SOC
ΔP
-30
-25
-20
-15
-10
-5
0
5
10
Crank Angle (°ATDC)

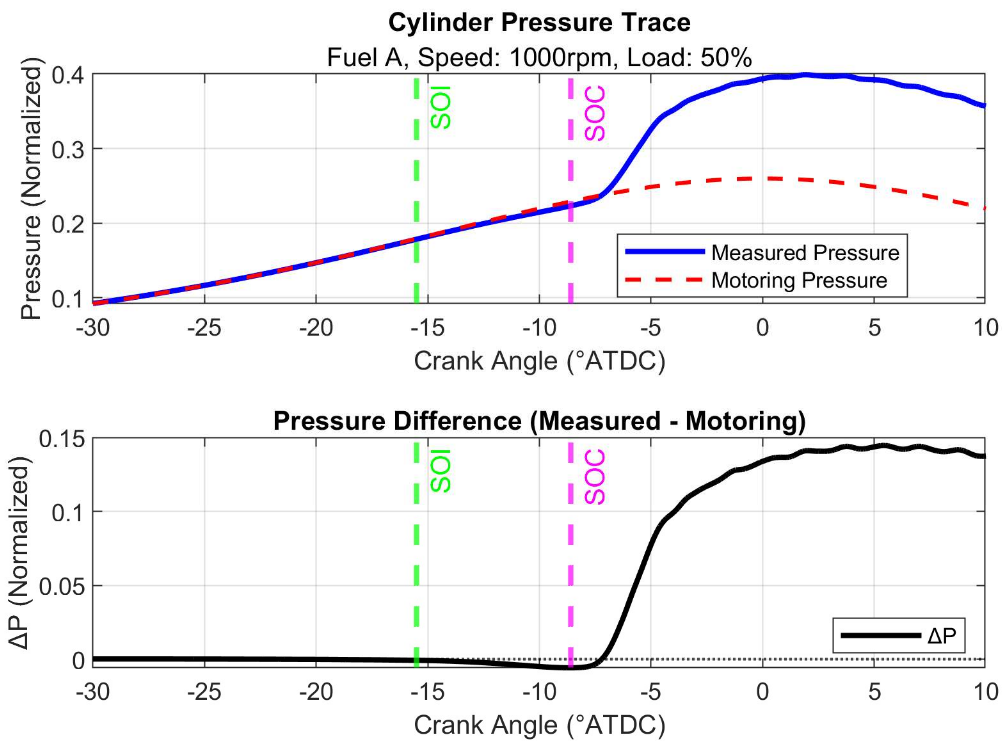
Cylinder Pressure Trace
Fuel A, Speed: 1000rpm, Load: 50%
Pressure (Normalized)
Crank Angle (°ATDC)
SOI
SOC
Measured Pressure
Motoring Pressure
Pressure Difference (Measured - Motoring)
ΔP (Normalized)
ΔP

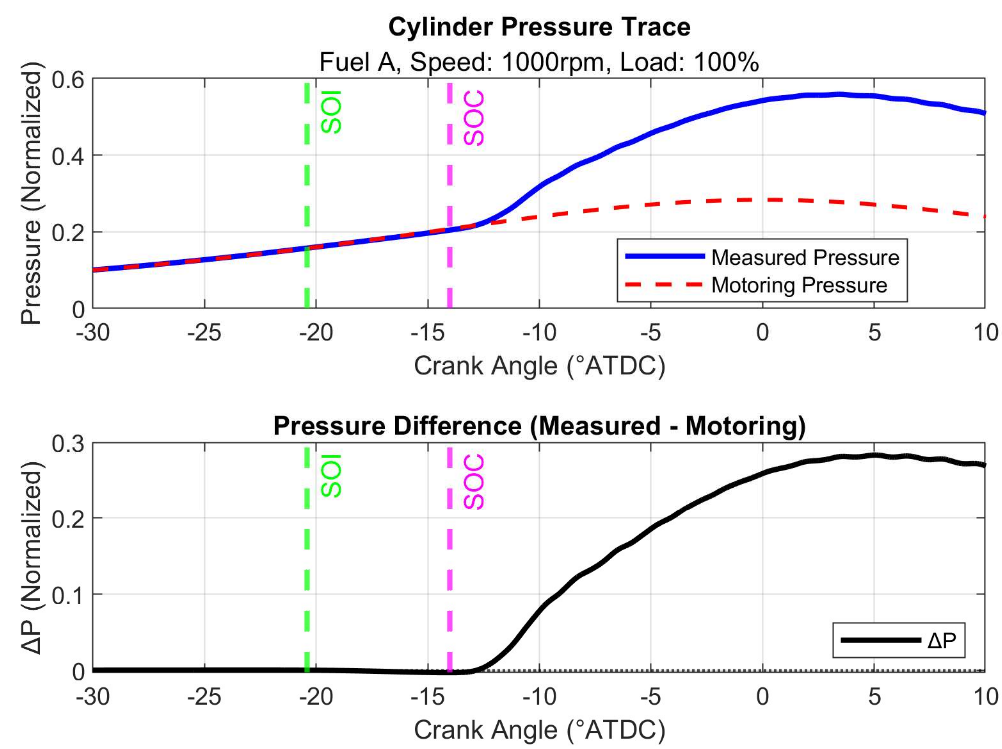
Cylinder Pressure Trace
Fuel A, Speed: 1000rpm, Load: 100%
Pressure (Normalized)
Crank Angle (°ATDC)
SOI
SOC
Measured Pressure
Motoring Pressure
Pressure Difference (Measured - Motoring)
ΔP (Normalized)
ΔP

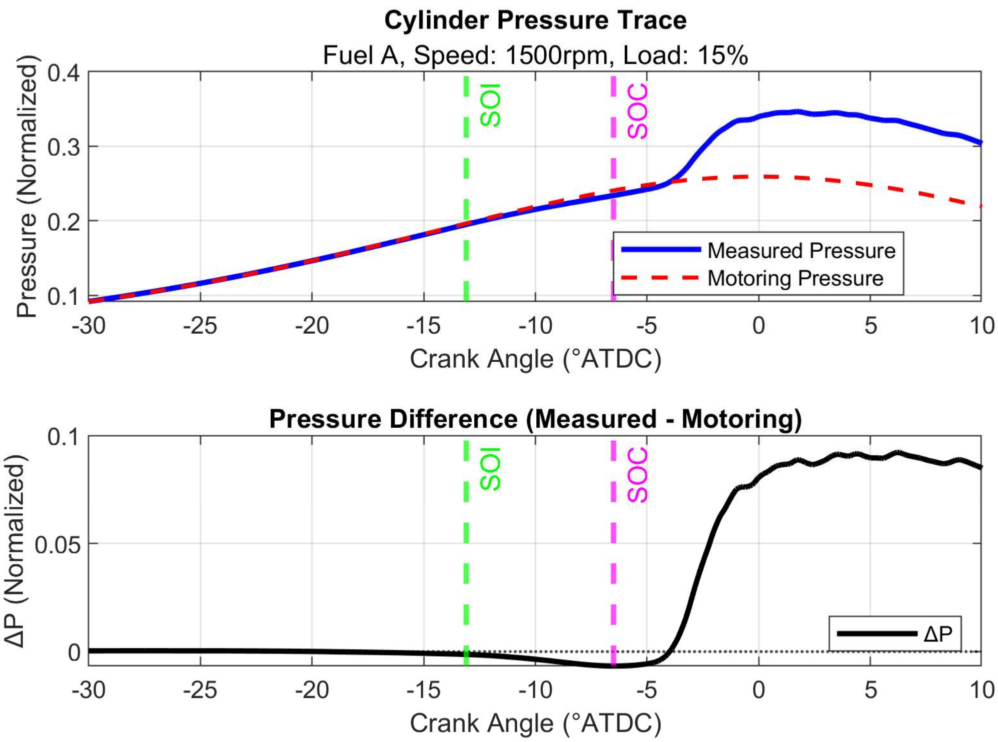
Cylinder Pressure Trace
Fuel A, Speed: 1500rpm, Load: 15%
Pressure (Normalized)
SOI
SOC
Measured Pressure
Motoring Pressure
Crank Angle (°ATDC)
Pressure Difference (Measured - Motoring)
ΔP (Normalized)
ΔP

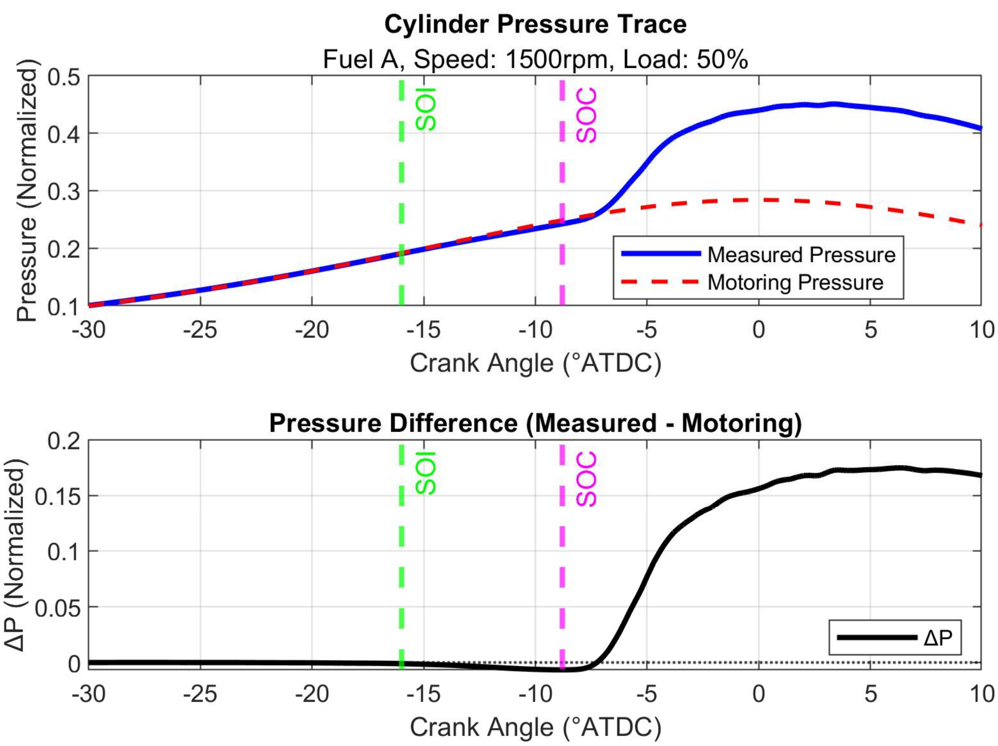
Cylinder Pressure Trace
Fuel A, Speed: 1500rpm, Load: 50%
Pressure (Normalized)
SOI
SOC
Measured Pressure
Motoring Pressure
Crank Angle (°ATDC)
Pressure Difference (Measured - Motoring)
ΔP (Normalized)
ΔP

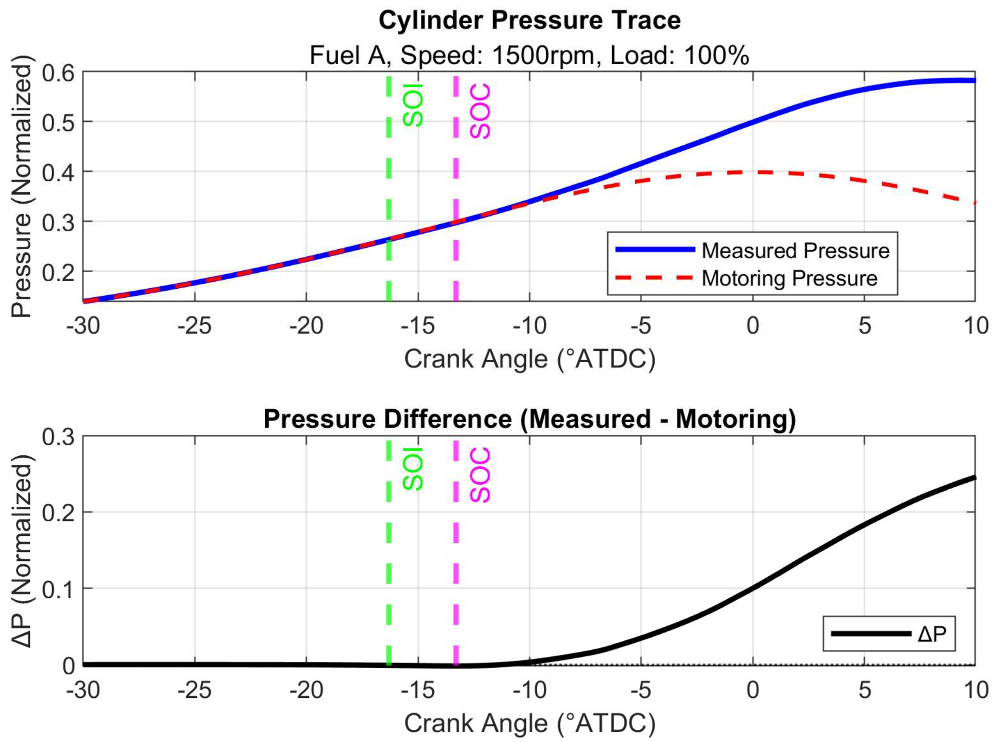
Cylinder Pressure Trace
Fuel A, Speed: 1500rpm, Load: 100%
Pressure (Normalized)
SOI
SOC
Measured Pressure
Motoring Pressure
Crank Angle (°ATDC)
Pressure Difference (Measured - Motoring)
ΔP (Normalized)
ΔP

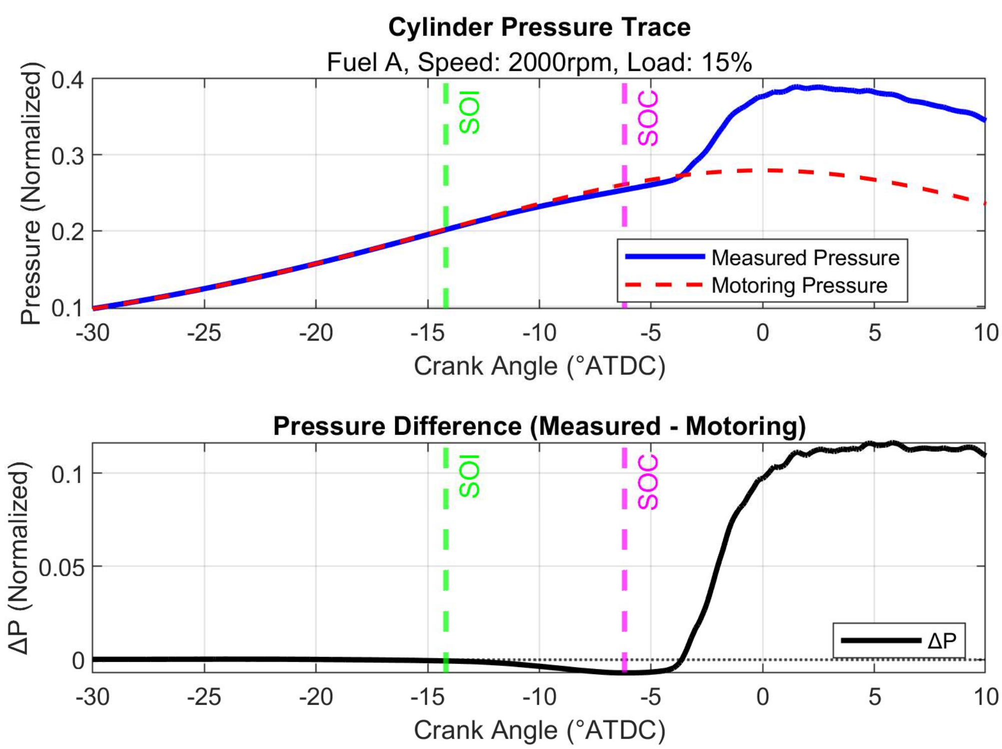
Cylinder Pressure Trace
Fuel A, Speed: 2000rpm, Load: 15%
Pressure (Normalized)
SOI
SOC
Measured Pressure
Motoring Pressure
Crank Angle (°ATDC)
Pressure Difference (Measured - Motoring)
ΔP (Normalized)
ΔP

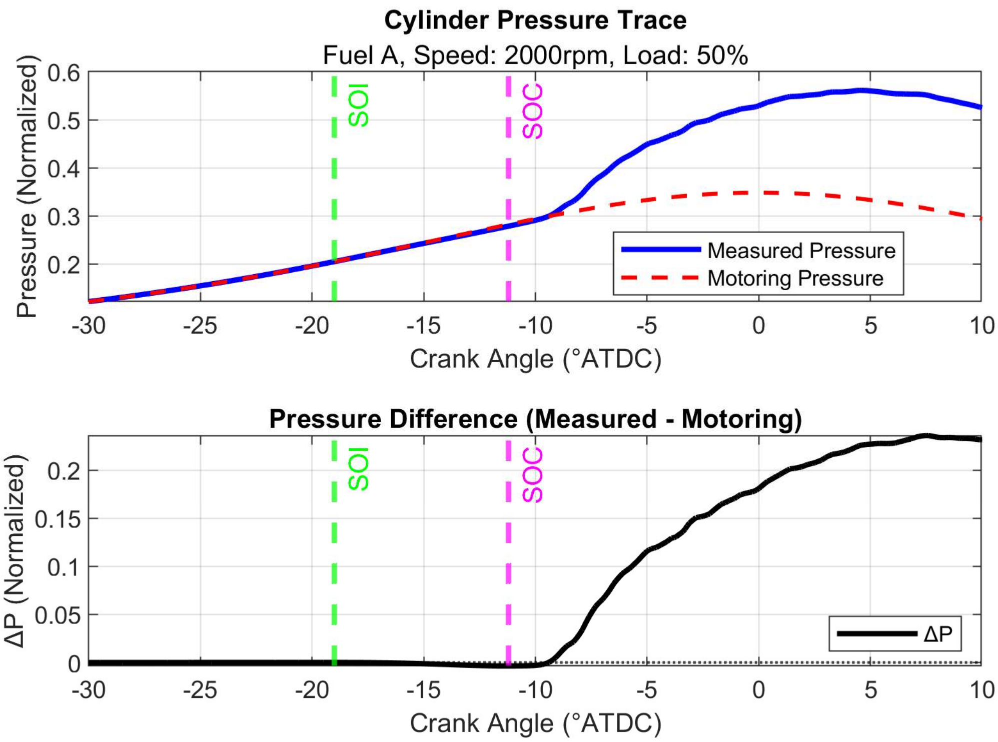
Cylinder Pressure Trace
Fuel A, Speed: 2000rpm, Load: 50%
Pressure (Normalized)
SOI
SOC
Measured Pressure
Motoring Pressure
Crank Angle (°ATDC)
Pressure Difference (Measured - Motoring)
ΔP (Normalized)
ΔP

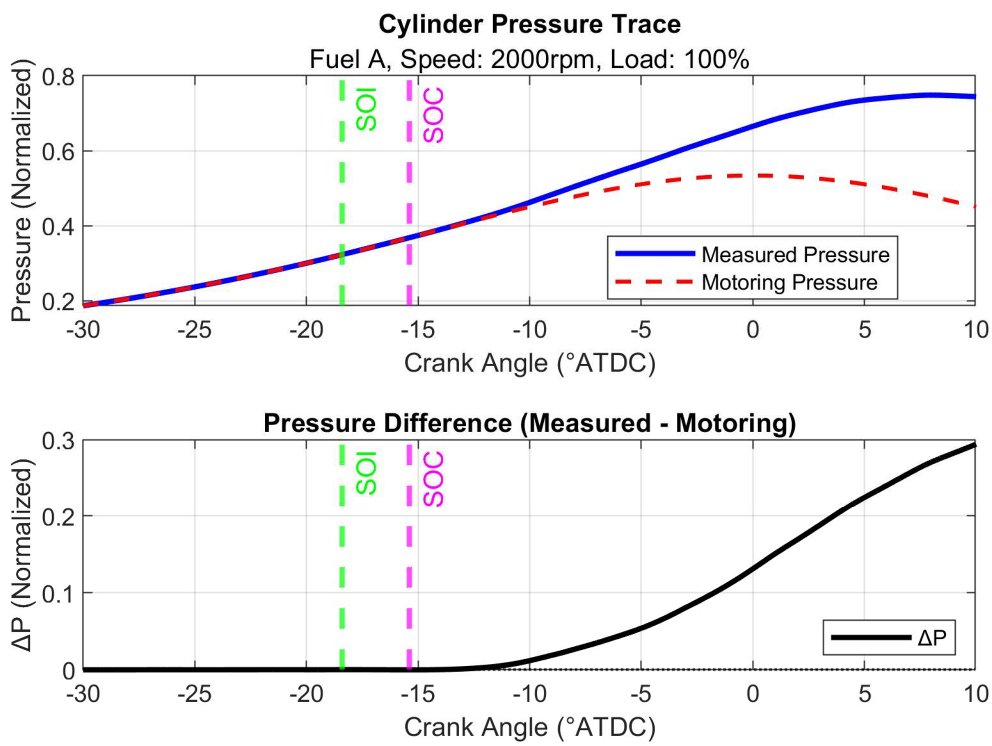
Cylinder Pressure Trace
Fuel A, Speed: 2000rpm, Load: 100%
Pressure (Normalized)
SOI
SOC
Measured Pressure
Motoring Pressure
Crank Angle (°ATDC)
Pressure Difference (Measured - Motoring)
ΔP (Normalized)
ΔP

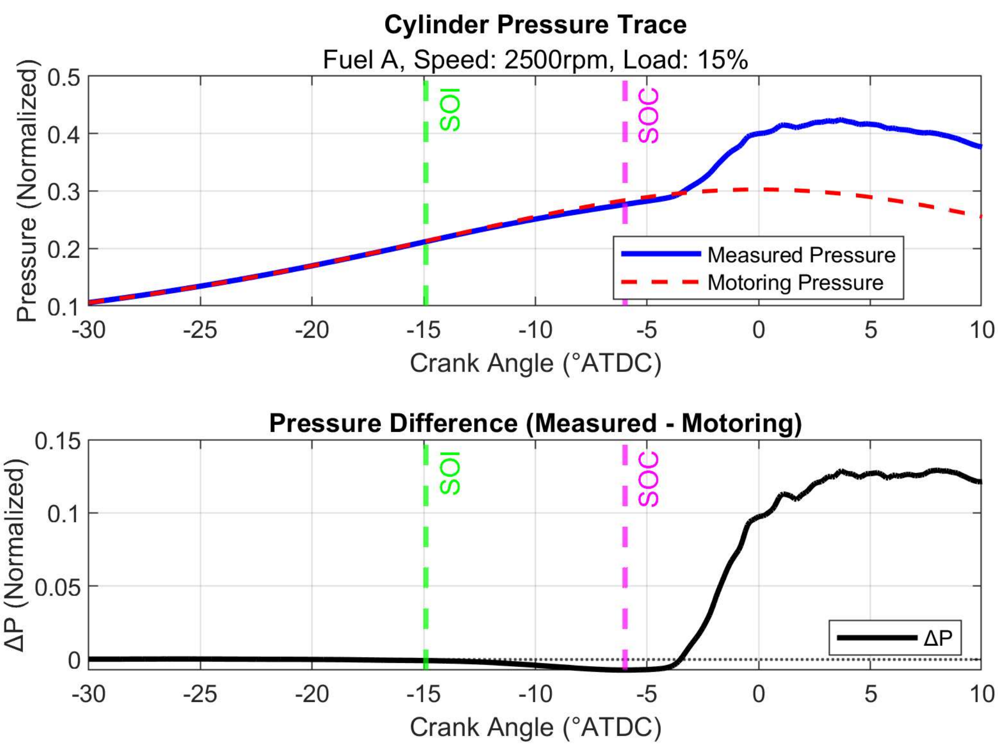
Cylinder Pressure Trace
Fuel A, Speed: 2500rpm, Load: 15%
Pressure (Normalized)
SOI
SOC
Measured Pressure
Motoring Pressure
Crank Angle (°ATDC)
Pressure Difference (Measured - Motoring)
ΔP (Normalized)
ΔP

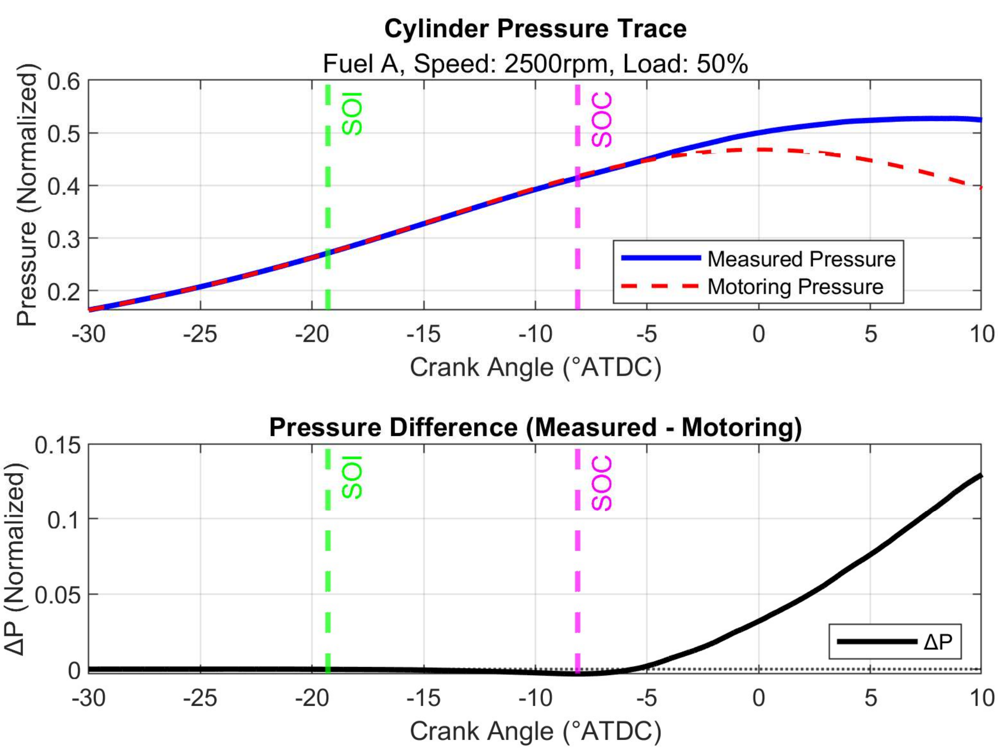
Cylinder Pressure Trace
Fuel A, Speed: 2500rpm, Load: 50%
Pressure (Normalized)
SOI
SOC
Measured Pressure
Motoring Pressure
Crank Angle (°ATDC)
Pressure Difference (Measured - Motoring)
ΔP (Normalized)
ΔP

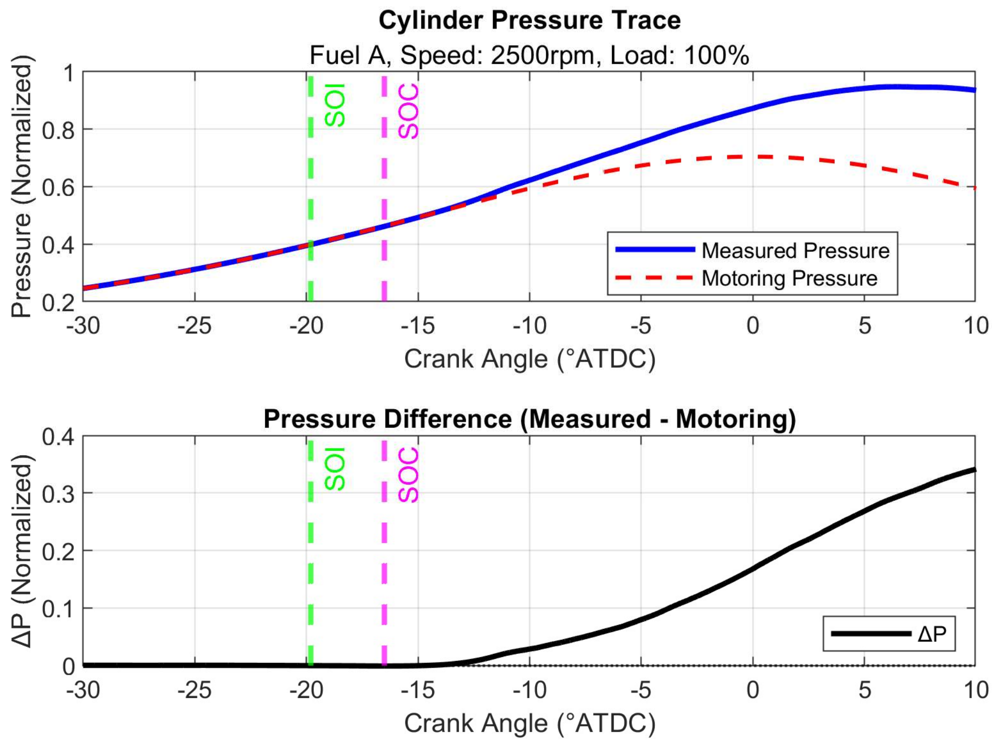
Cylinder Pressure Trace
Fuel A, Speed: 2500rpm, Load: 100%
Pressure (Normalized)
SOI
SOC
Measured Pressure
Motoring Pressure
Crank Angle (°ATDC)
Pressure Difference (Measured - Motoring)
ΔP (Normalized)
ΔP
Crank Angle (°ATDC)

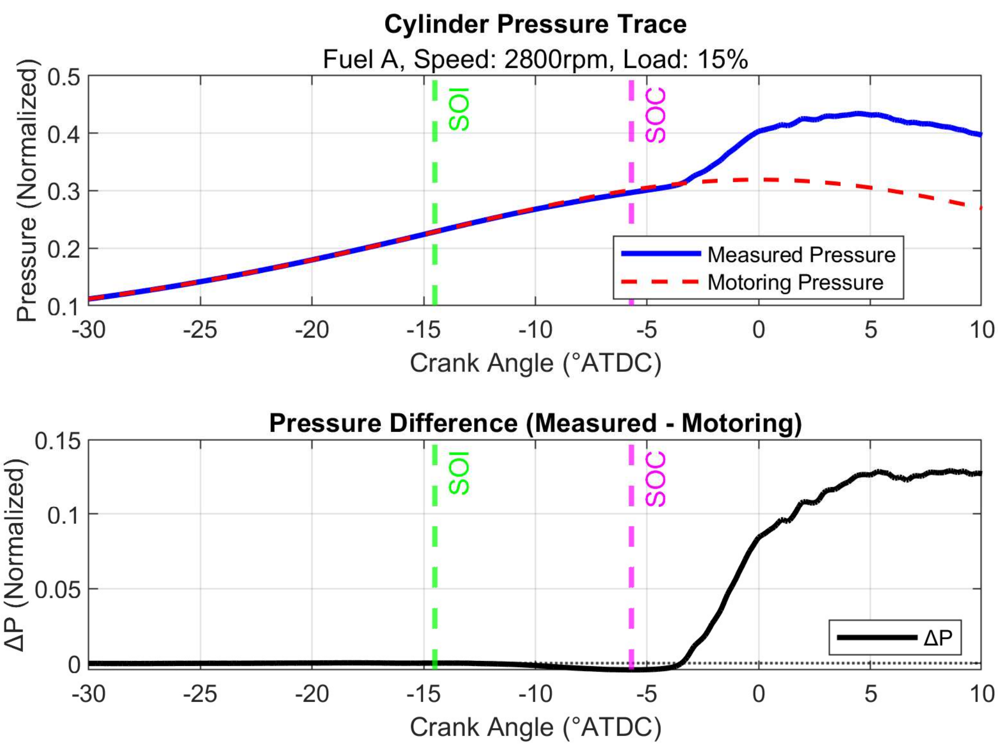
Cylinder Pressure Trace
Fuel A, Speed: 2800rpm, Load: 15%
Pressure (Normalized)
SOI
SOC
Measured Pressure
Motoring Pressure
Crank Angle (°ATDC)
Pressure Difference (Measured - Motoring)
ΔP (Normalized)
ΔP
Crank Angle (°ATDC)

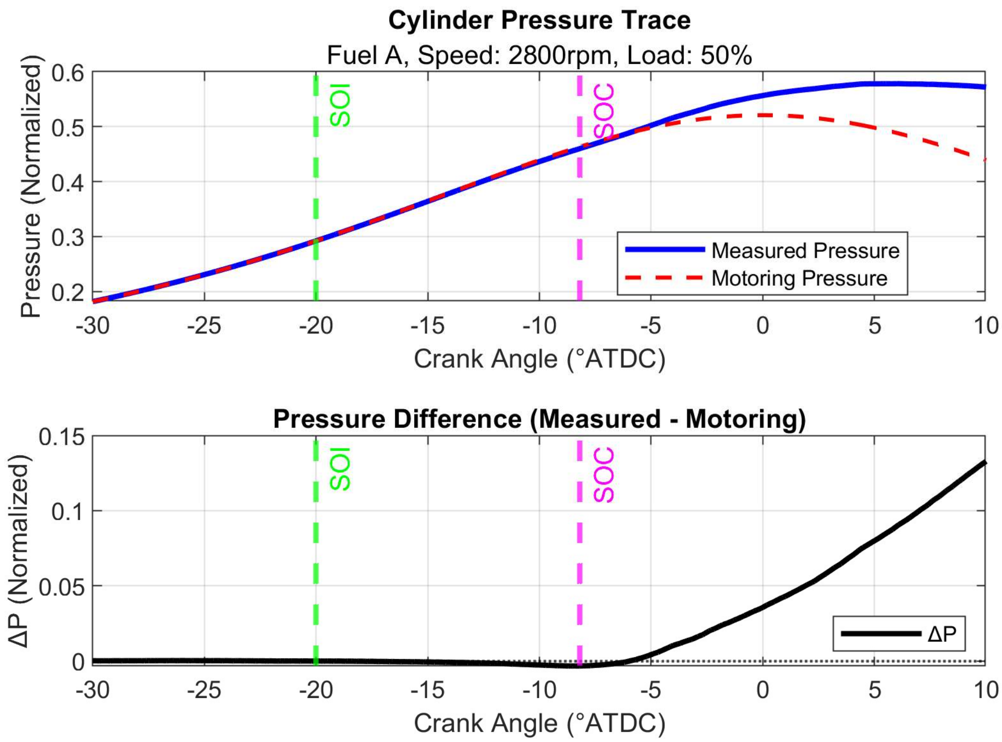
Cylinder Pressure Trace
Fuel A, Speed: 2800rpm, Load: 50%
Pressure (Normalized)
SOI
SOC
Measured Pressure
Motoring Pressure
Crank Angle (°ATDC)
Pressure Difference (Measured - Motoring)
ΔP (Normalized)
ΔP
Crank Angle (°ATDC)

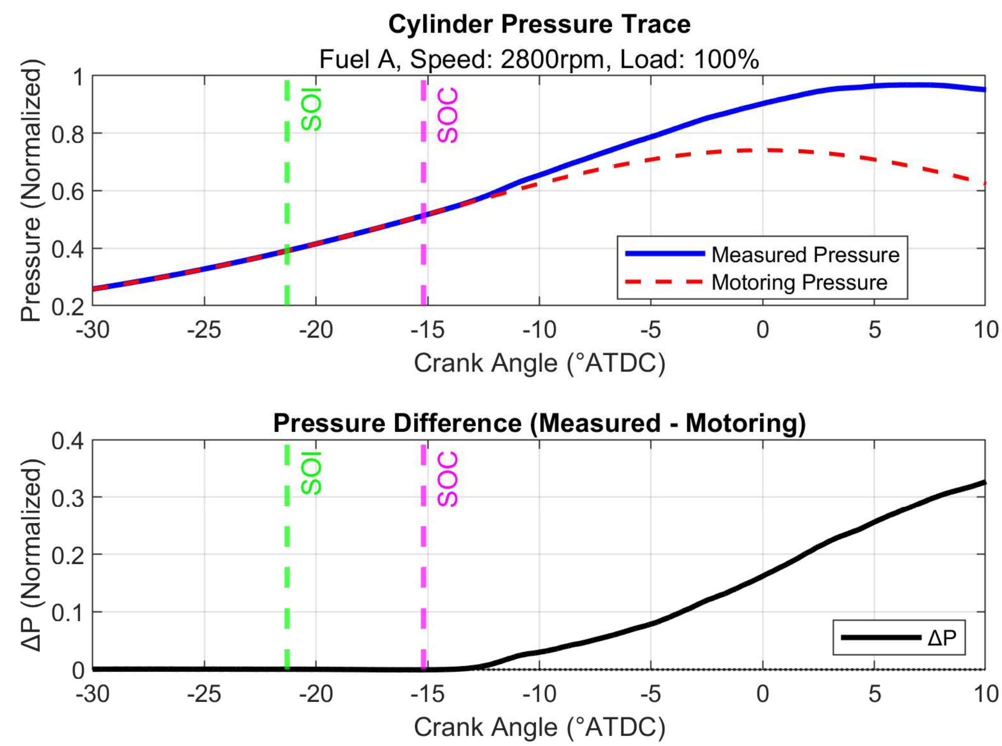
Cylinder Pressure Trace
Fuel A, Speed: 2800rpm, Load: 100%
Pressure (Normalized)
SOI
SOC
Measured Pressure
Motoring Pressure
Crank Angle (°ATDC)
Pressure Difference (Measured - Motoring)
ΔP (Normalized)
ΔP
Crank Angle (°ATDC)

Fuel B

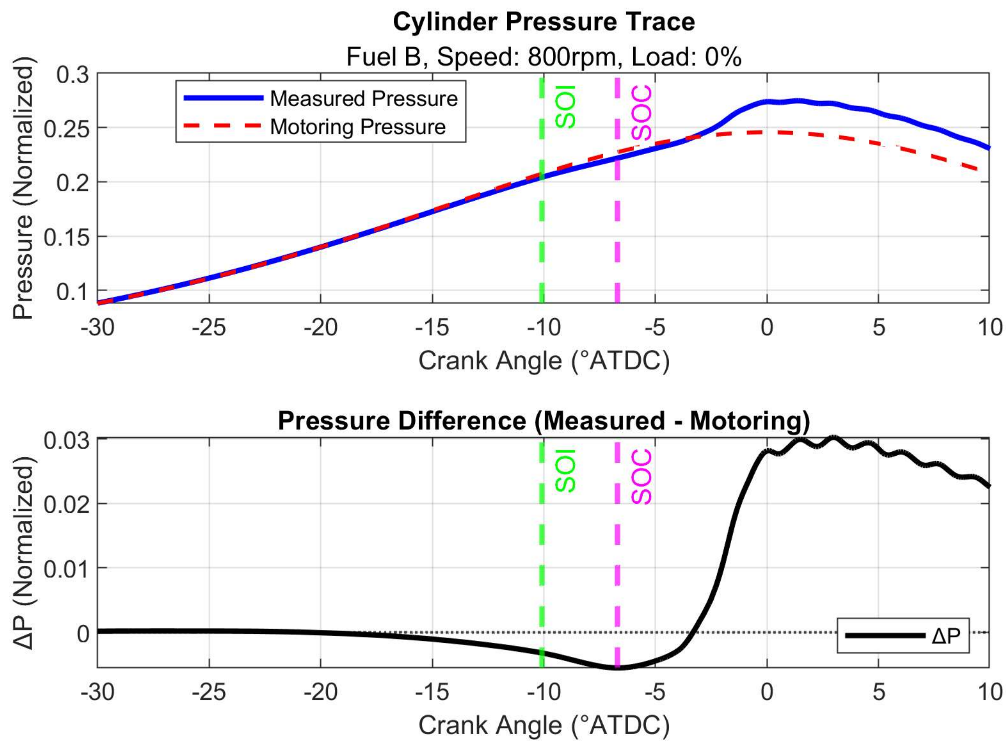
Cylinder Pressure Trace
Fuel B, Speed: 800rpm, Load: 0%
Measured Pressure
Motoring Pressure
SOI
SOC
Pressure (Normalized)
0.3
0.25
0.2
0.15
0.1
-30
-25
-20
-15
-10
-5
0
5
10
Crank Angle (°ATDC)
Pressure Difference (Measured - Motoring)
ΔP (Normalized)
0.03
0.02
0.01
0
ΔP
Crank Angle (°ATDC)

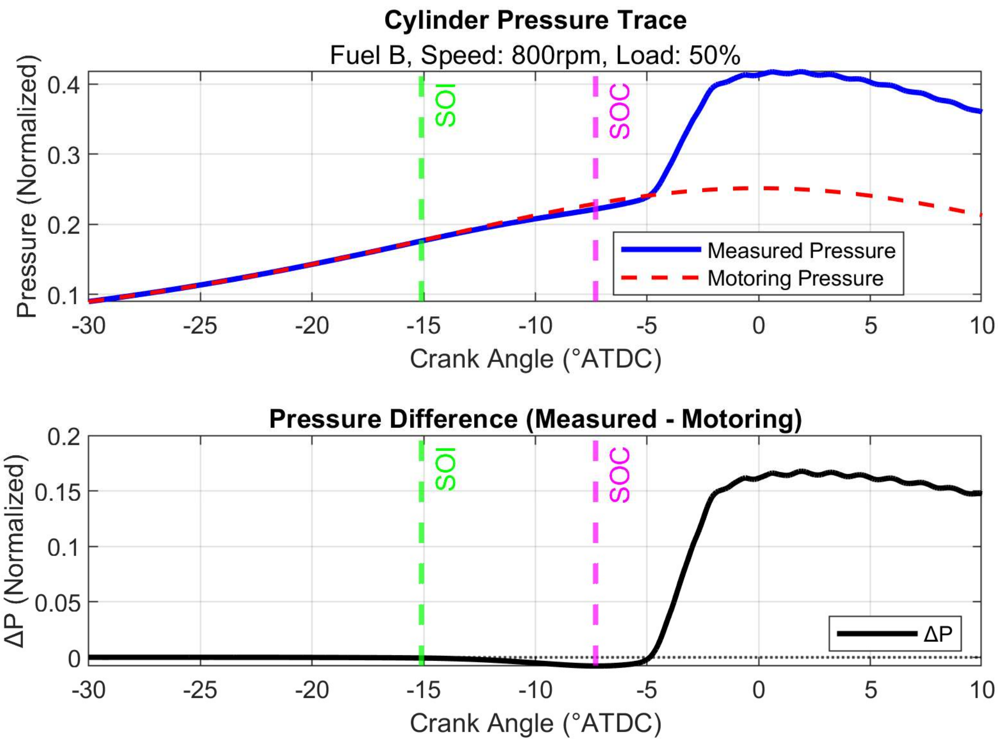
Cylinder Pressure Trace
Fuel B, Speed: 800rpm, Load: 50%
Pressure (Normalized)
SOI
SOC
Measured Pressure
Motoring Pressure
Crank Angle (°ATDC)
Pressure Difference (Measured - Motoring)
ΔP (Normalized)
ΔP
Crank Angle (°ATDC)

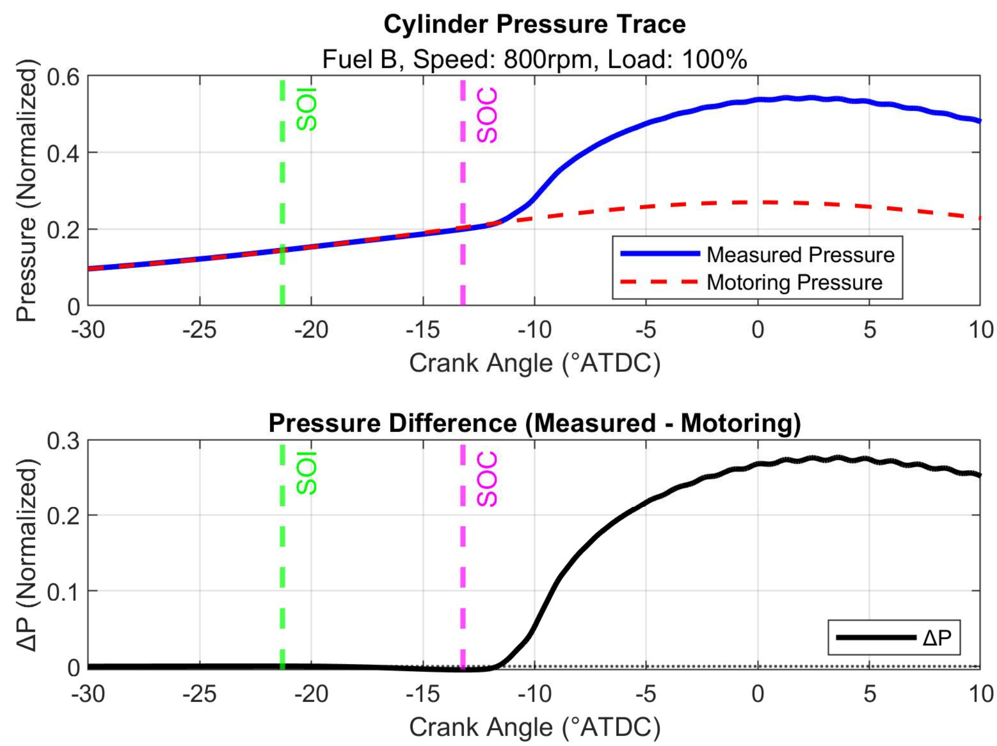
Cylinder Pressure Trace
Fuel B, Speed: 800rpm, Load: 100%
Pressure (Normalized)
SOI
SOC
Measured Pressure
Motoring Pressure
Crank Angle (°ATDC)
Pressure Difference (Measured - Motoring)
ΔP (Normalized)
ΔP
Crank Angle (°ATDC)

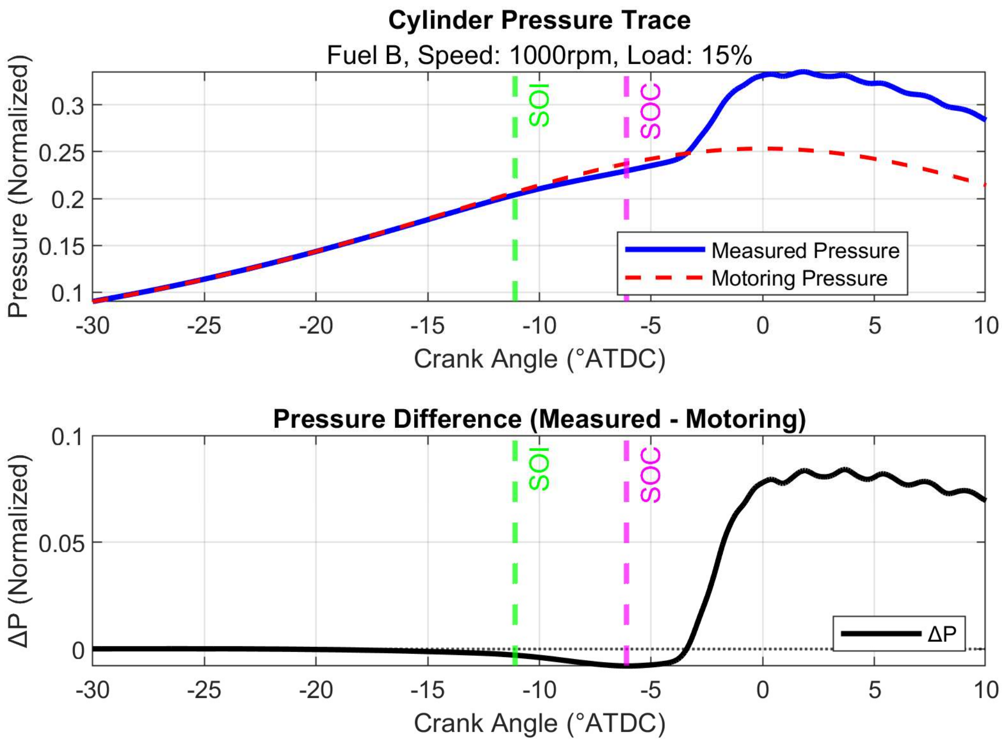

Cylinder Pressure Trace
Fuel B, Speed: 1000rpm, Load: 15%
Pressure (Normalized)
SOI
SOC
Measured Pressure
Motoring Pressure
Crank Angle (°ATDC)
Pressure Difference (Measured - Motoring)
ΔP (Normalized)
ΔP

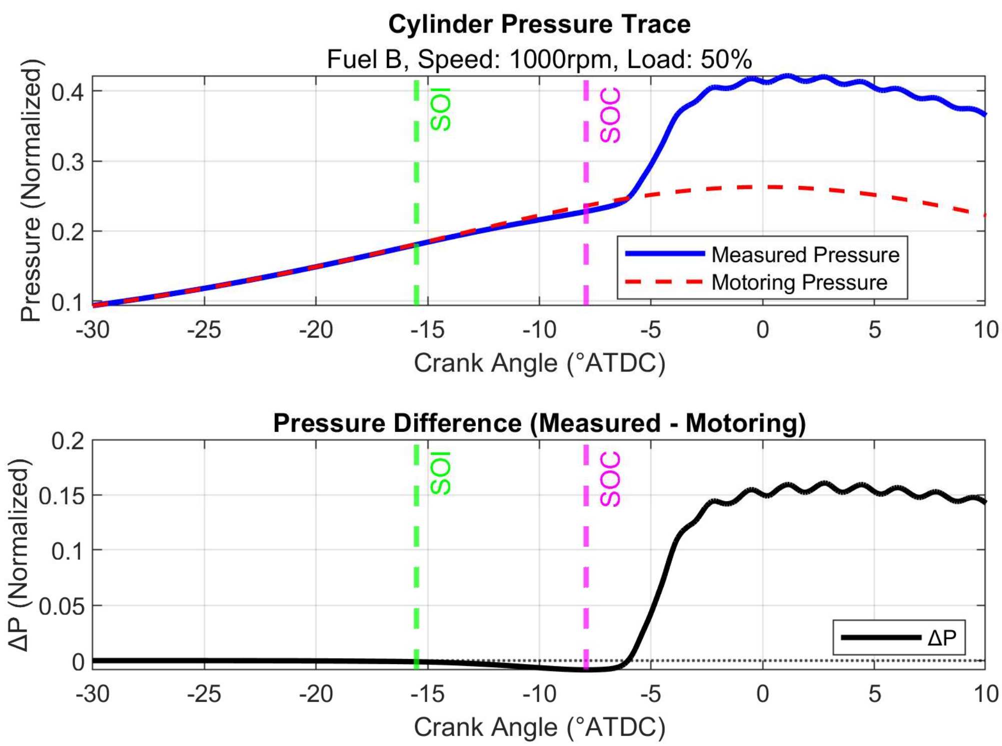

Cylinder Pressure Trace
Fuel B, Speed: 1000rpm, Load: 50%
Pressure (Normalized)
SOI
SOC
Measured Pressure
Motoring Pressure
Crank Angle (°ATDC)
Pressure Difference (Measured - Motoring)
ΔP (Normalized)
ΔP

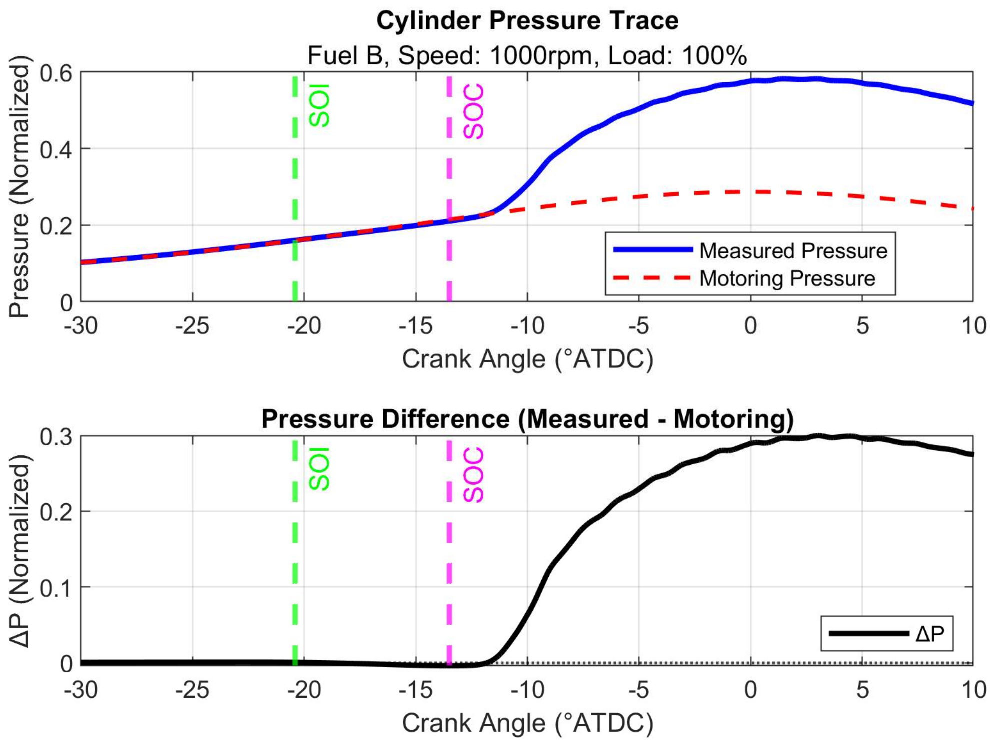
Cylinder Pressure Trace
Fuel B, Speed: 1000rpm, Load: 100%
Pressure (Normalized)
SOI
SOC
Measured Pressure
Motoring Pressure
Crank Angle (°ATDC)
Pressure Difference (Measured - Motoring)
ΔP (Normalized)
ΔP
Crank Angle (°ATDC)

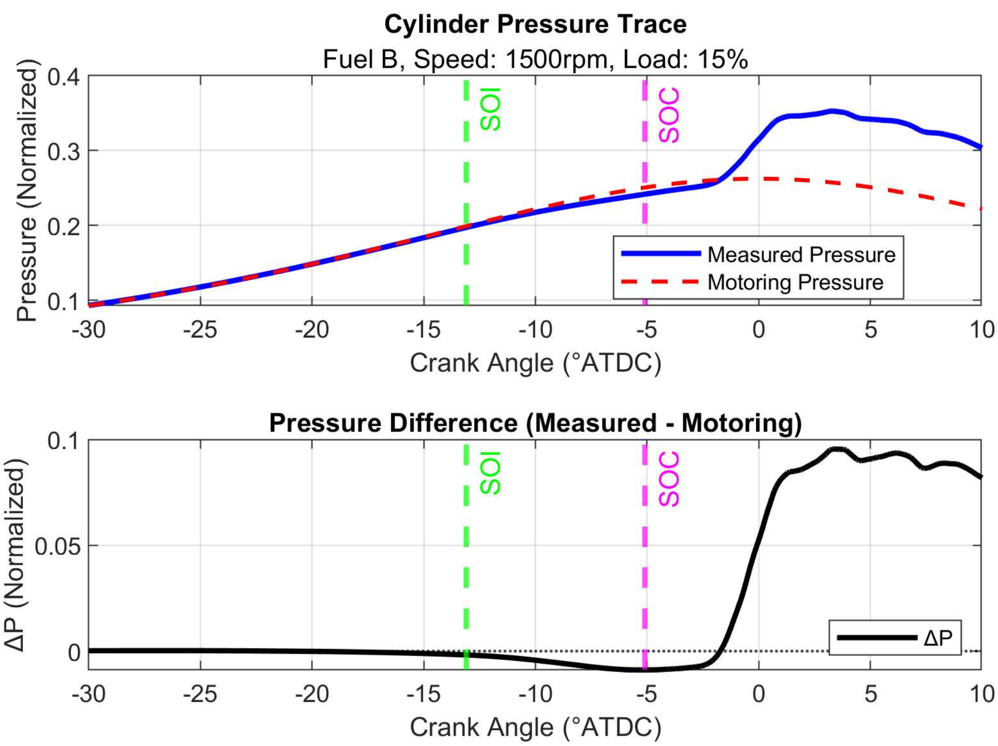
Cylinder Pressure Trace
Fuel B, Speed: 1500rpm, Load: 15%
Pressure (Normalized)
SOI
SOC
Measured Pressure
Motoring Pressure
Crank Angle (°ATDC)
Pressure Difference (Measured - Motoring)
ΔP (Normalized)
ΔP
Crank Angle (°ATDC)

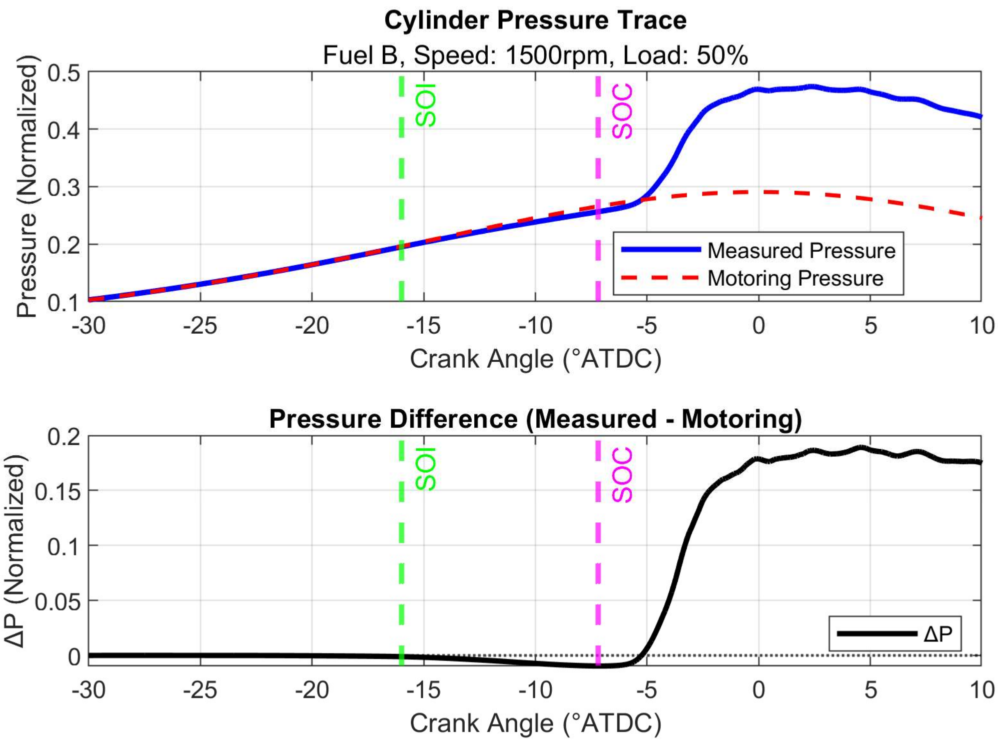
Cylinder Pressure Trace
Fuel B, Speed: 1500rpm, Load: 50%
Pressure (Normalized)
0.1
0.2
0.3
0.4
0.5
SOI
SOC
Measured Pressure
Motoring Pressure
-30 -25 -20 -15 -10 -5 0 5 10
Crank Angle (°ATDC)
Pressure Difference (Measured - Motoring)
ΔP (Normalized)
0
0.05
0.1
0.15
0.2
SOI
SOC
ΔP
-30 -25 -20 -15 -10 -5 0 5 10
Crank Angle (°ATDC)

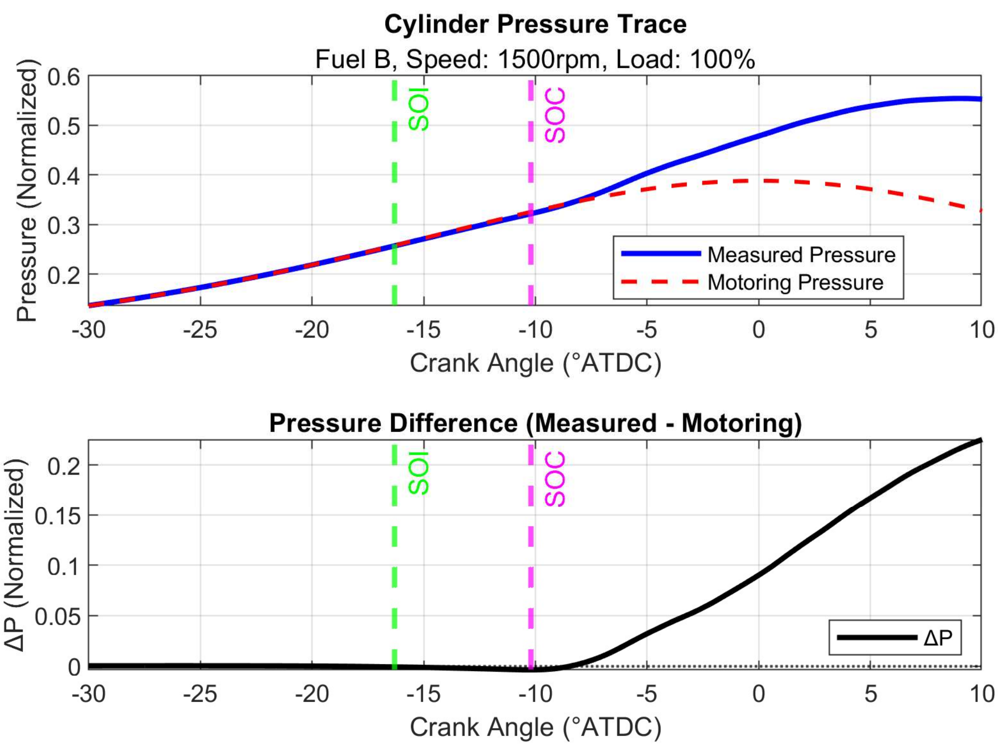
Cylinder Pressure Trace
Fuel B, Speed: 1500rpm, Load: 100%
Pressure (Normalized)
0.2
0.3
0.4
0.5
0.6
SOI
SOC
Measured Pressure
Motoring Pressure
-30 -25 -20 -15 -10 -5 0 5 10
Crank Angle (°ATDC)
Pressure Difference (Measured - Motoring)
ΔP (Normalized)
0
0.05
0.1
0.15
0.2
SOI
SOC
ΔP
-30 -25 -20 -15 -10 -5 0 5 10
Crank Angle (°ATDC)

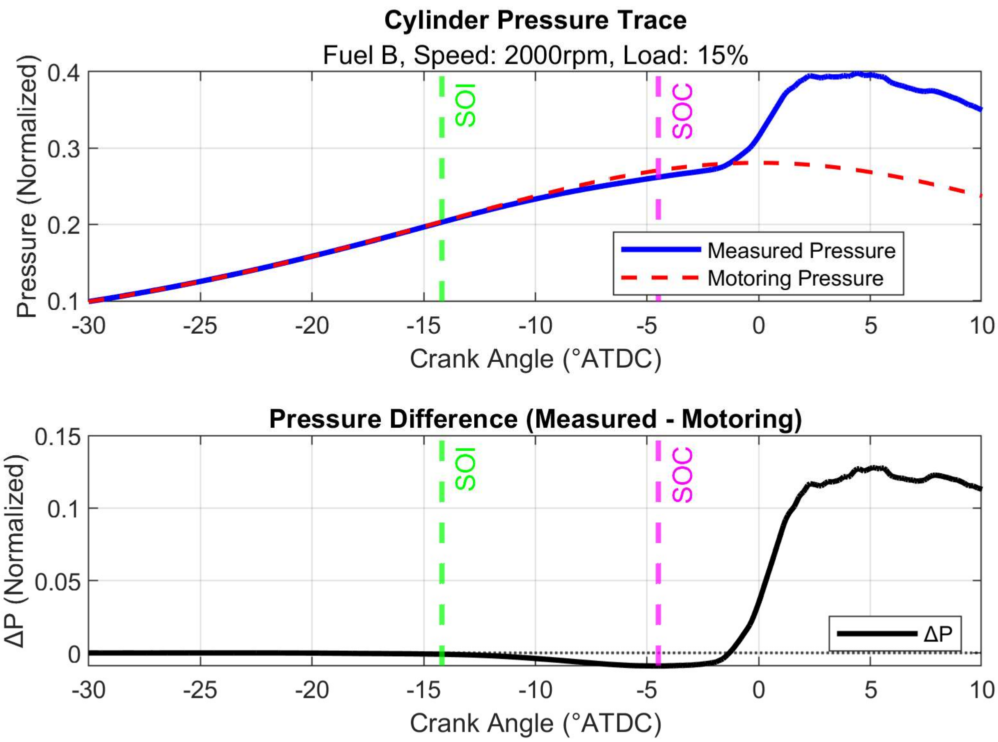
Cylinder Pressure Trace
Fuel B, Speed: 2000rpm, Load: 15%
Pressure (Normalized)
SOI
SOC
Measured Pressure
Motoring Pressure
Crank Angle (°ATDC)
Pressure Difference (Measured - Motoring)
ΔP (Normalized)
ΔP

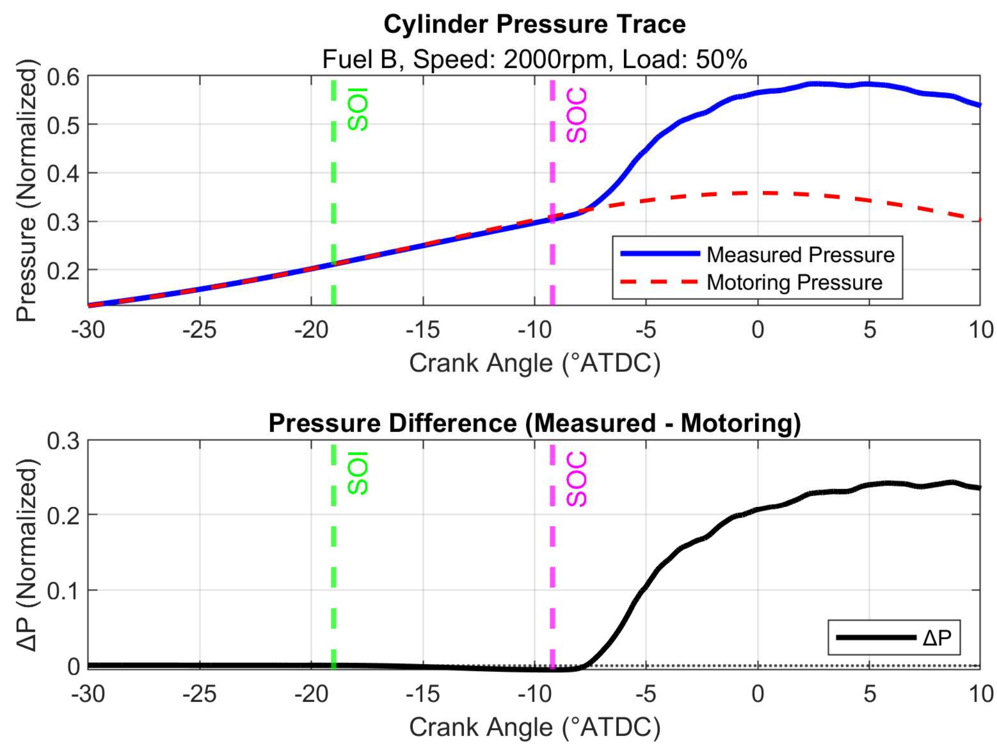
Cylinder Pressure Trace
Fuel B, Speed: 2000rpm, Load: 50%
Pressure (Normalized)
SOI
SOC
Measured Pressure
Motoring Pressure
Crank Angle (°ATDC)
Pressure Difference (Measured - Motoring)
ΔP (Normalized)
ΔP

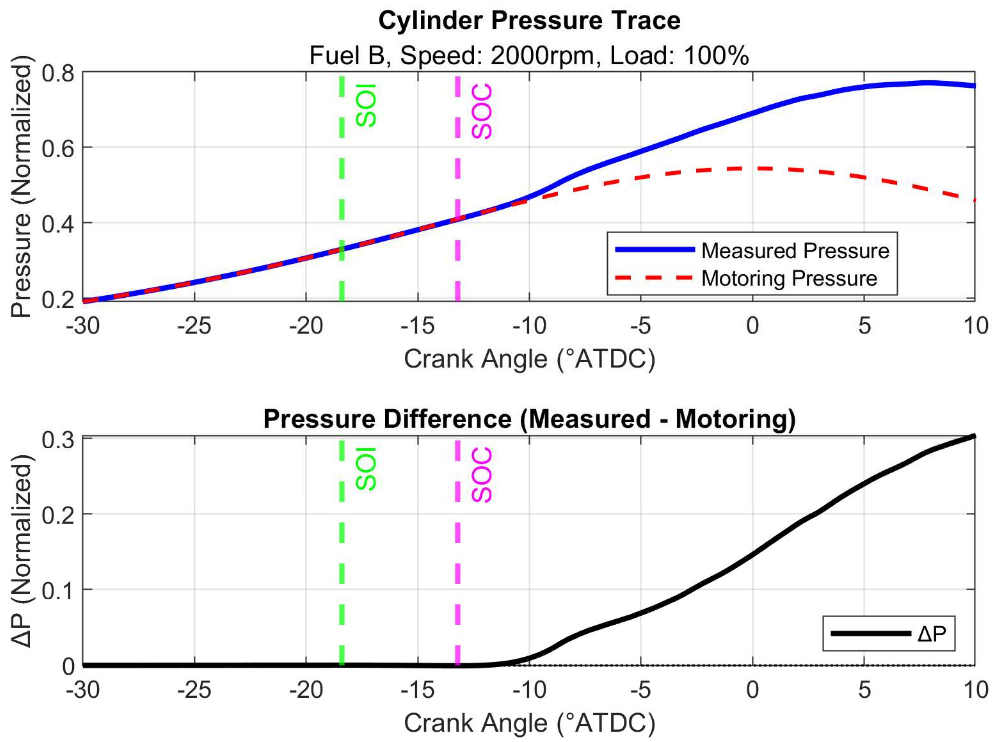

Cylinder Pressure Trace
Fuel B, Speed: 2000rpm, Load: 100%
Pressure (Normalized)
SOI
SOC
Measured Pressure
Motoring Pressure
Crank Angle (°ATDC)
Pressure Difference (Measured - Motoring)
ΔP (Normalized)
ΔP

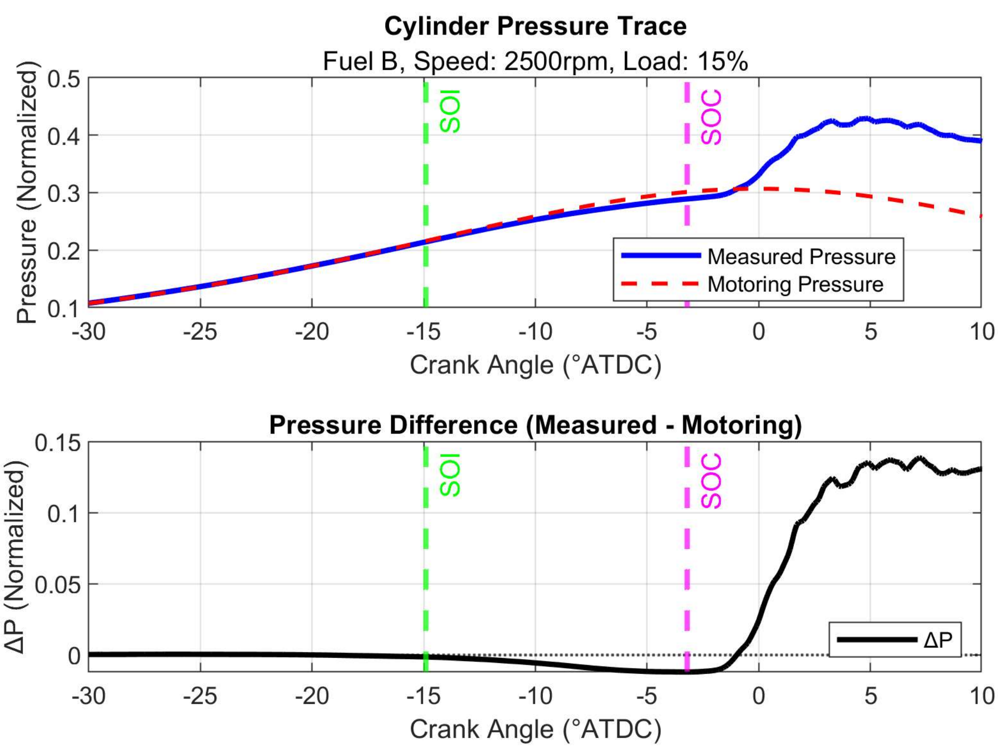

Cylinder Pressure Trace
Fuel B, Speed: 2500rpm, Load: 15%
Pressure (Normalized)
SOI
SOC
Measured Pressure
Motoring Pressure
Crank Angle (°ATDC)
Pressure Difference (Measured - Motoring)
ΔP (Normalized)
ΔP

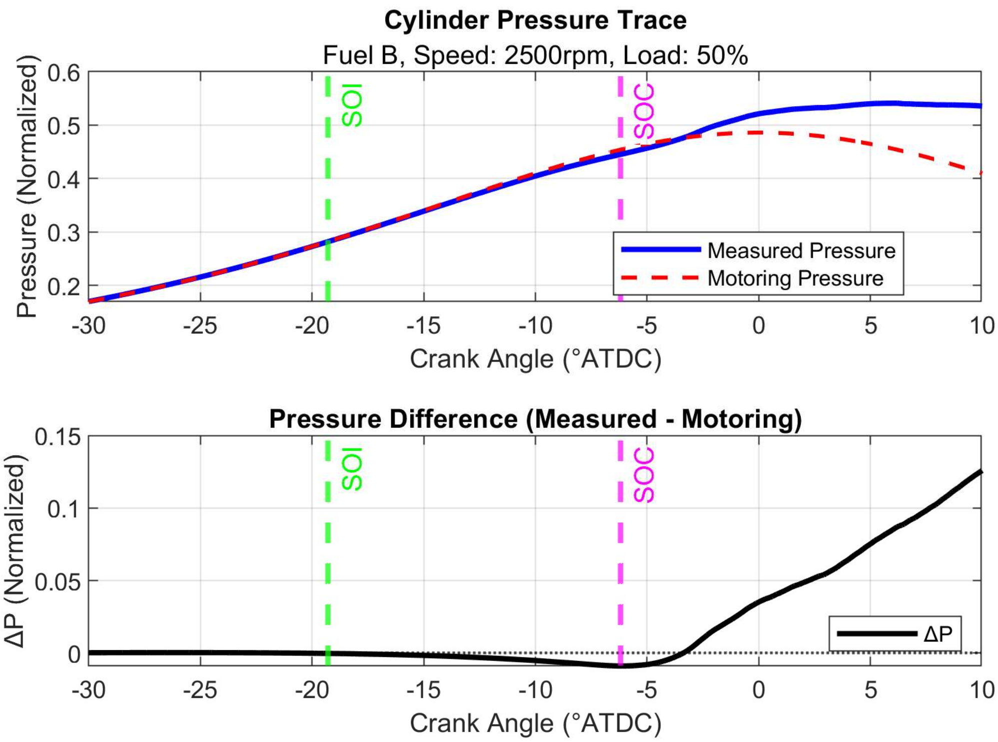
Cylinder Pressure Trace
Fuel B, Speed: 2500rpm, Load: 50%
Pressure (Normalized)
SOI
SOC
Measured Pressure
Motoring Pressure
Crank Angle (°ATDC)
Pressure Difference (Measured - Motoring)
ΔP (Normalized)
SOI
SOC
ΔP
Crank Angle (°ATDC)

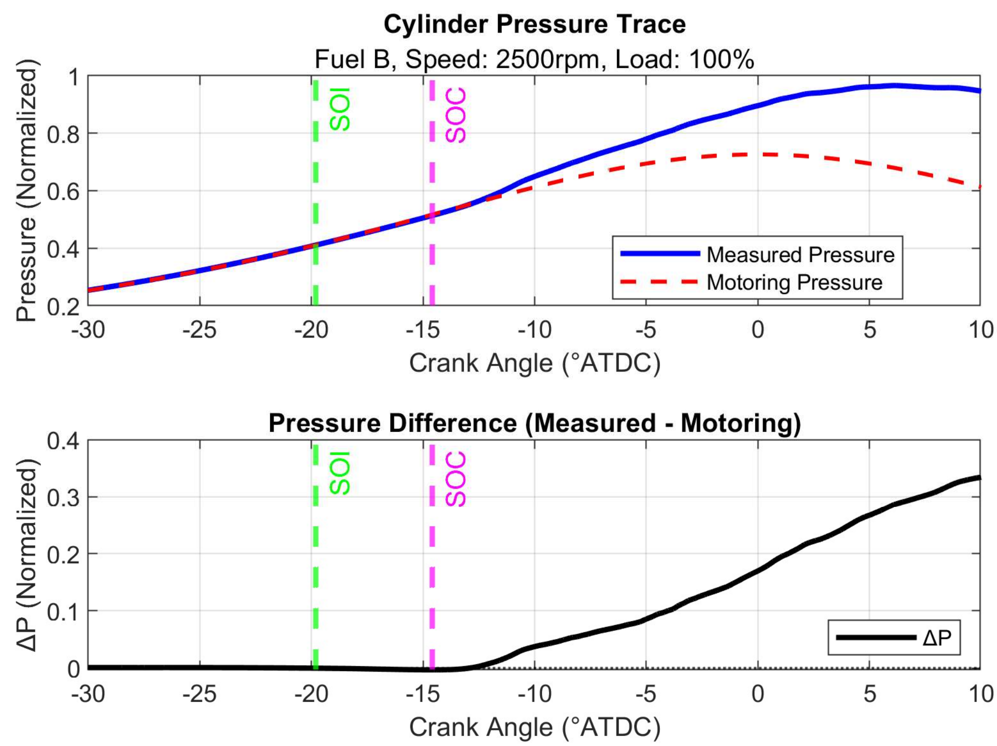
Cylinder Pressure Trace
Fuel B, Speed: 2500rpm, Load: 100%
Pressure (Normalized)
SOI
SOC
Measured Pressure
Motoring Pressure
Crank Angle (°ATDC)
Pressure Difference (Measured - Motoring)
ΔP (Normalized)
SOI
SOC
ΔP
Crank Angle (°ATDC)

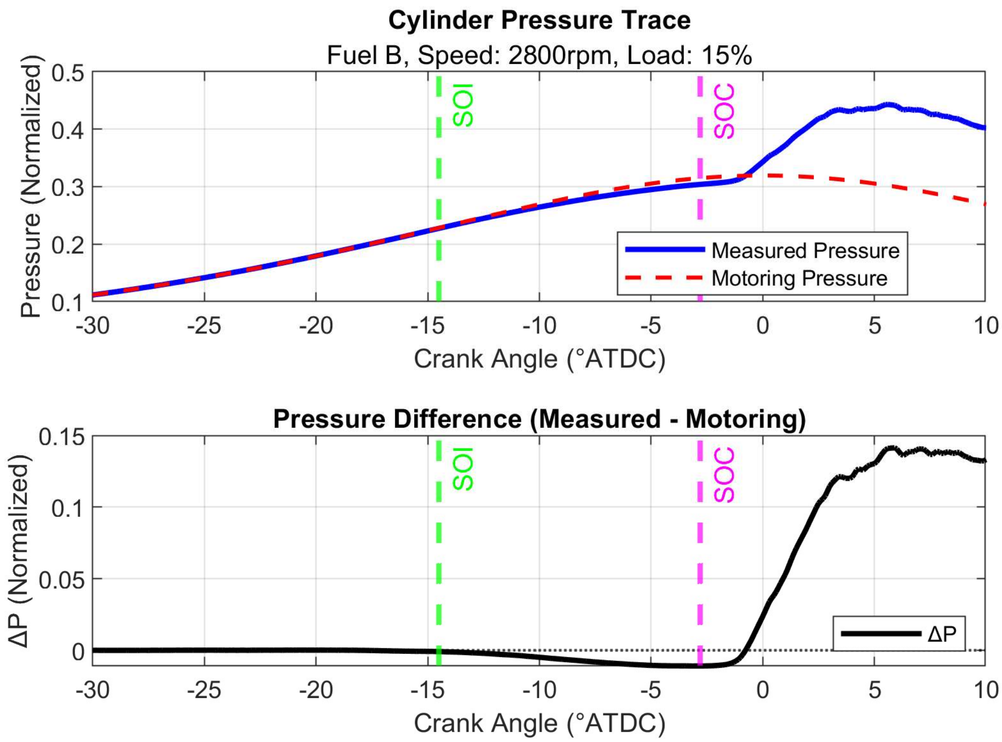

Cylinder Pressure Trace
Fuel B, Speed: 2800rpm, Load: 15%
Pressure (Normalized)
SOI
SOC
Measured Pressure
Motoring Pressure
Crank Angle (°ATDC)
Pressure Difference (Measured - Motoring)
ΔP (Normalized)
ΔP

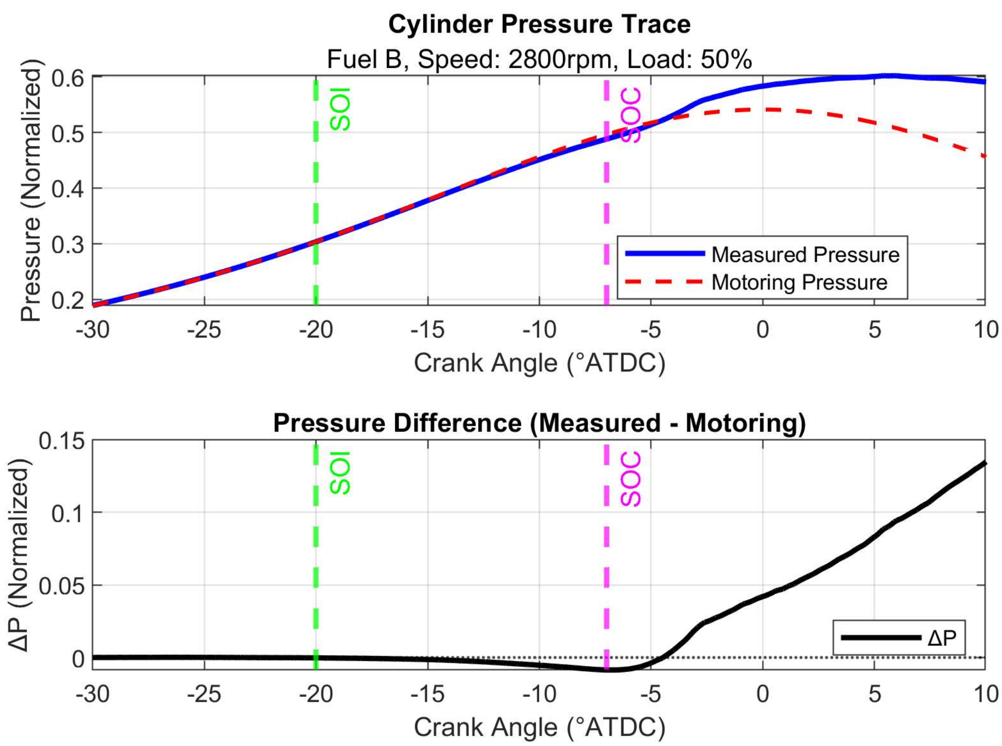

Cylinder Pressure Trace
Fuel B, Speed: 2800rpm, Load: 50%
Pressure (Normalized)
SOI
SOC
Measured Pressure
Motoring Pressure
Crank Angle (°ATDC)
Pressure Difference (Measured - Motoring)
ΔP (Normalized)
ΔP

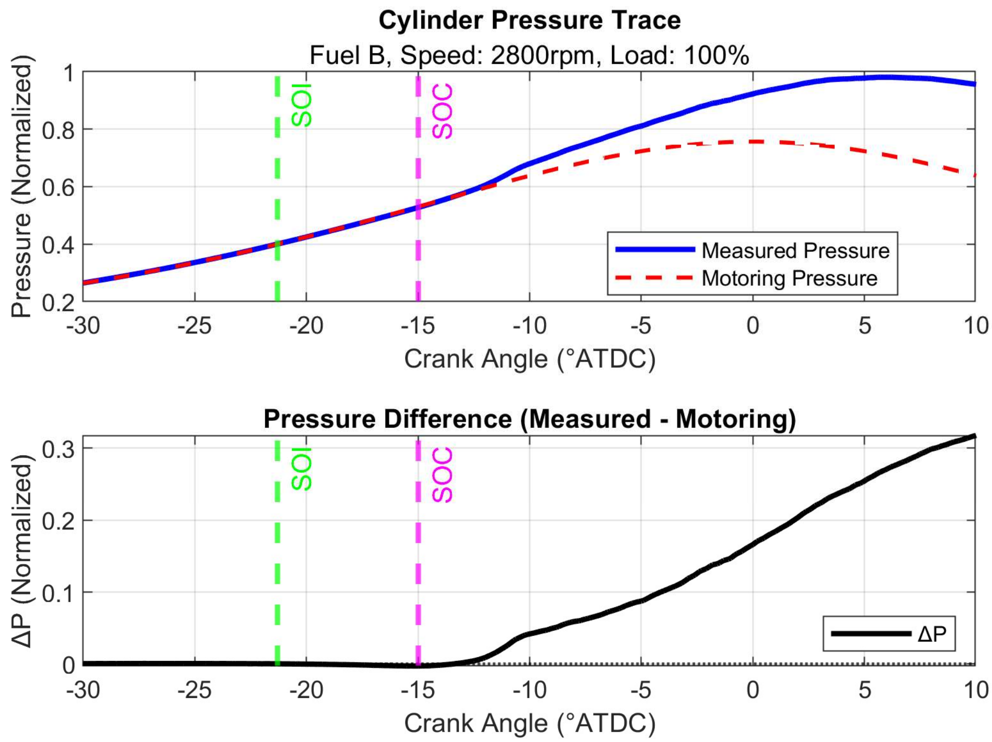
Cylinder Pressure Trace
Fuel B, Speed: 2800rpm, Load: 100%
Pressure (Normalized)
SOI
SOC
Measured Pressure
Motoring Pressure
Crank Angle (°ATDC)
Pressure Difference (Measured - Motoring)
ΔP (Normalized)
ΔP
Crank Angle (°ATDC)

Fuel C

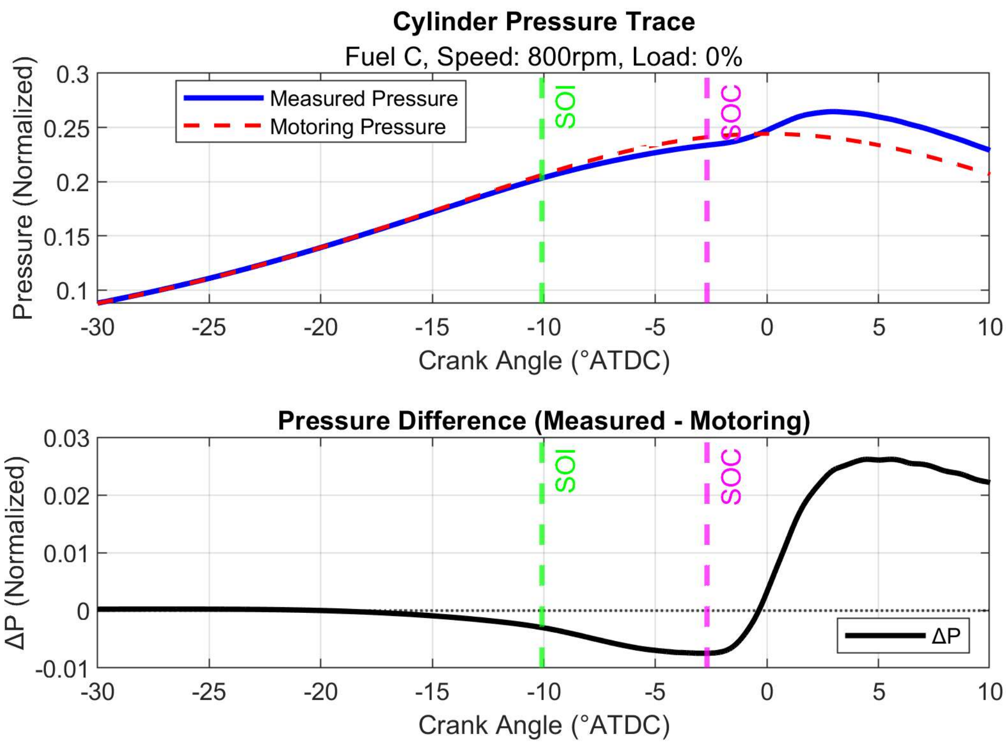

Cylinder Pressure Trace
Fuel C, Speed: 800rpm, Load: 0%
Measured Pressure
Motoring Pressure
SOI
SOC
Pressure (Normalized)
0.3
0.25
0.2
0.15
0.1
-30
-25
-20
-15
-10
-5
0
5
10
Crank Angle (°ATDC)
Pressure Difference (Measured - Motoring)
ΔP (Normalized)
0.03
0.02
0.01
0
-0.01
ΔP

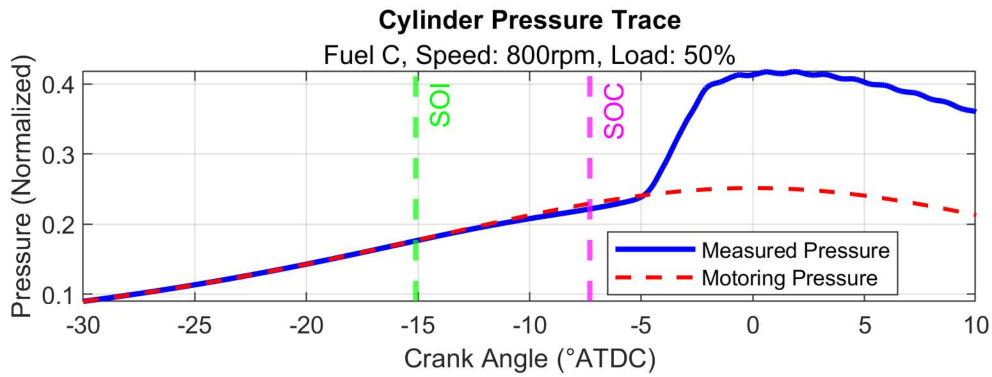
Cylinder Pressure Trace
Fuel C, Speed: 800rpm, Load: 50%
Pressure (Normalized)
SOI
SOC
Measured Pressure
Motoring Pressure
Crank Angle (°ATDC)

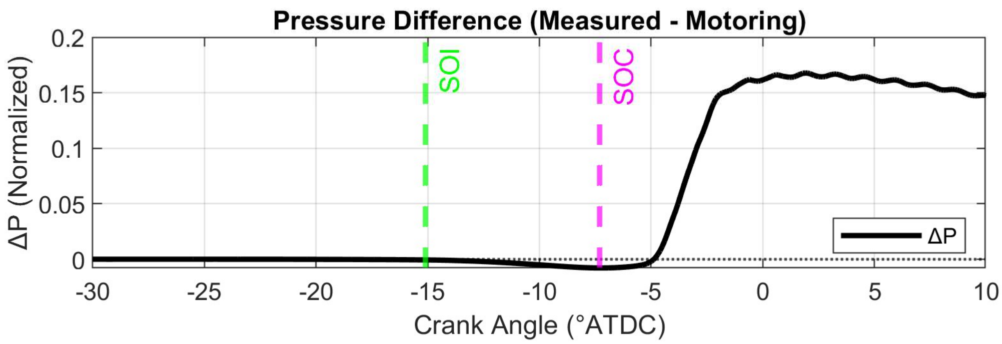
Pressure Difference (Measured - Motoring)
ΔP (Normalized)
SOI
SOC
ΔP
Crank Angle (°ATDC)

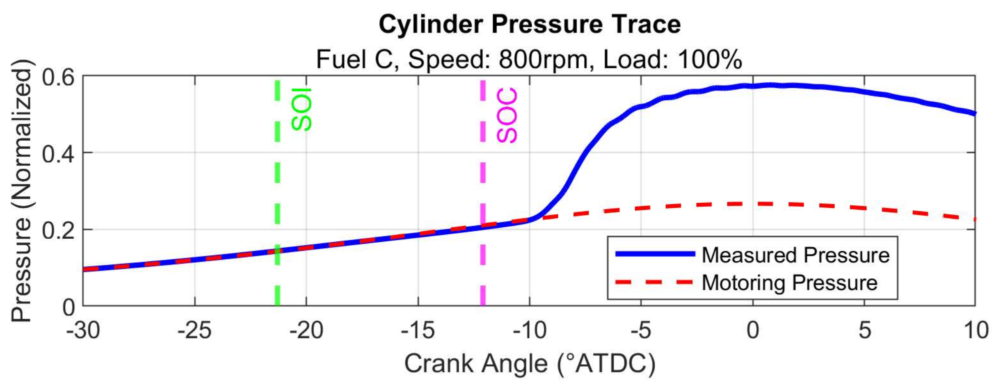
Cylinder Pressure Trace
Fuel C, Speed: 800rpm, Load: 100%
Pressure (Normalized)
SOI
SOC
Measured Pressure
Motoring Pressure
Crank Angle (°ATDC)

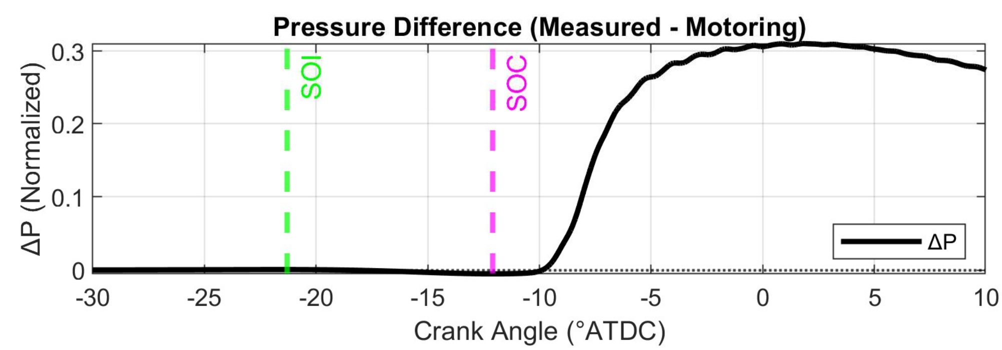
Pressure Difference (Measured - Motoring)
ΔP (Normalized)
SOI
SOC
ΔP
Crank Angle (°ATDC)

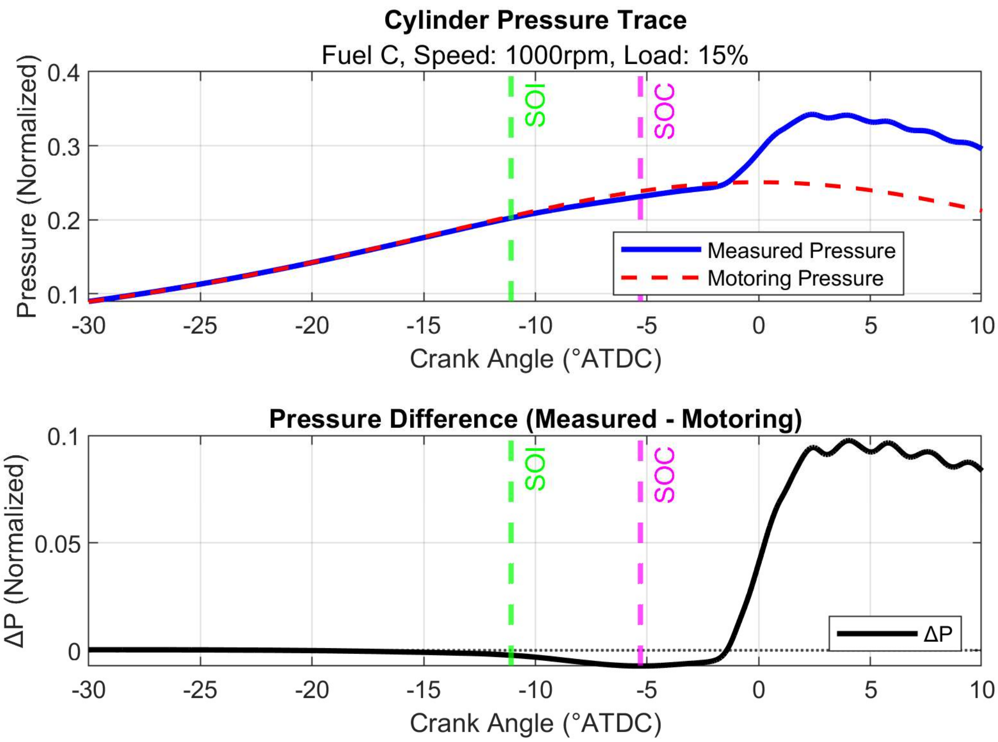
Cylinder Pressure Trace
Fuel C, Speed: 1000rpm, Load: 15%
Pressure (Normalized)
0.4
0.3
0.2
0.1
SOI
SOC
Measured Pressure
Motoring Pressure
-30
-25
-20
-15
-10
-5
0
5
10
Crank Angle (°ATDC)
Pressure Difference (Measured - Motoring)
ΔP (Normalized)
0.1
0.05
0
ΔP

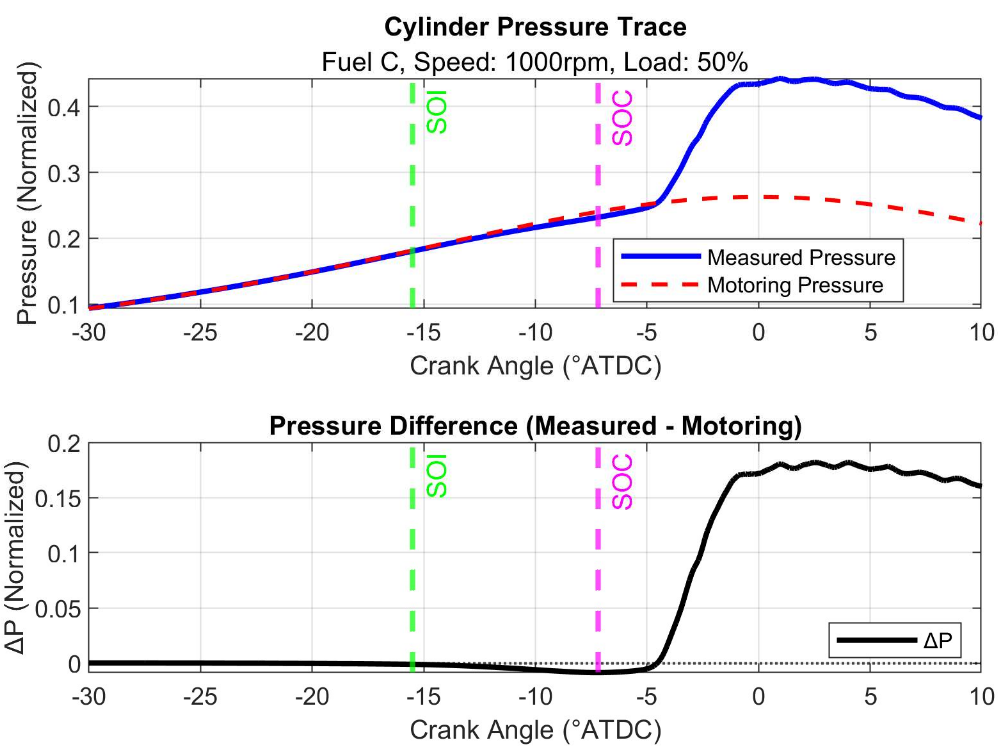
Cylinder Pressure Trace
Fuel C, Speed: 1000rpm, Load: 50%
Pressure (Normalized)
0.4
0.3
0.2
0.1
SOI
SOC
Measured Pressure
Motoring Pressure
-30
-25
-20
-15
-10
-5
0
5
10
Crank Angle (°ATDC)
Pressure Difference (Measured - Motoring)
ΔP (Normalized)
0.2
0.15
0.1
0.05
0
ΔP

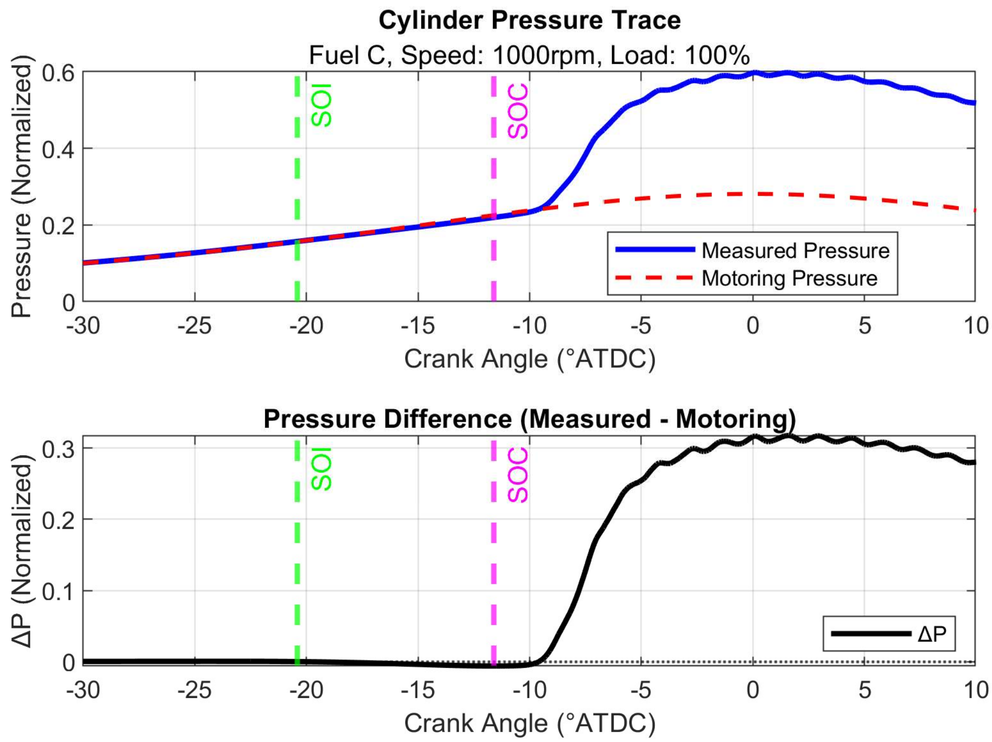
Cylinder Pressure Trace
Fuel C, Speed: 1000rpm, Load: 100%
Pressure (Normalized)
SOI
SOC
Measured Pressure
Motoring Pressure
Crank Angle (°ATDC)
Pressure Difference (Measured - Motoring)
ΔP (Normalized)
ΔP
Crank Angle (°ATDC)

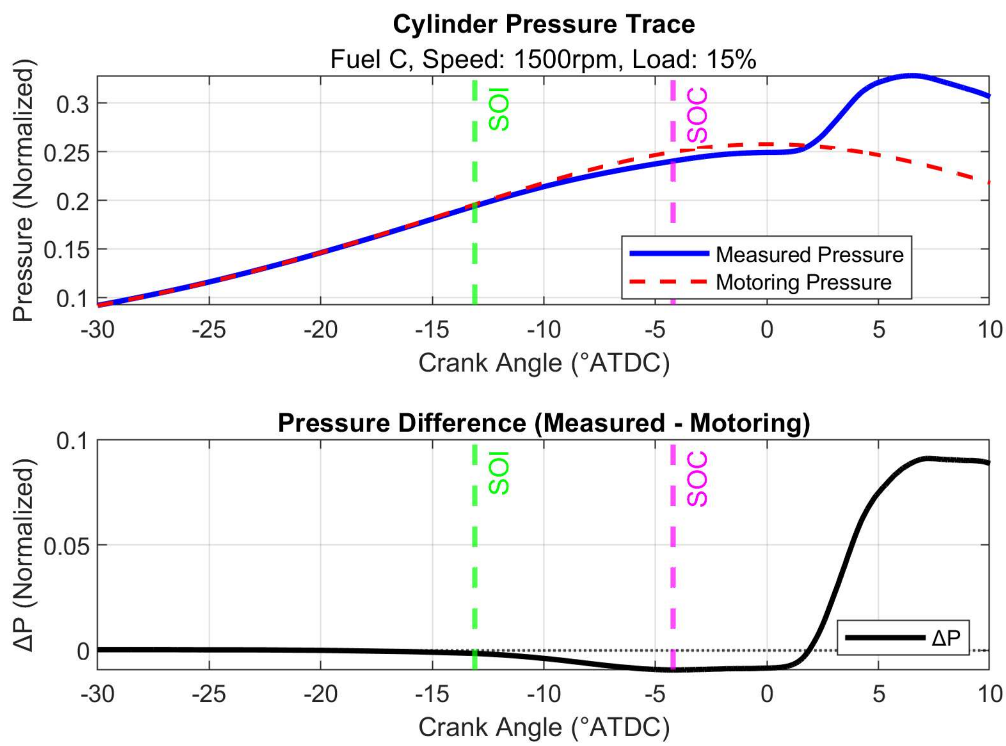
Cylinder Pressure Trace
Fuel C, Speed: 1500rpm, Load: 15%
Pressure (Normalized)
SOI
SOC
Measured Pressure
Motoring Pressure
Crank Angle (°ATDC)
Pressure Difference (Measured - Motoring)
ΔP (Normalized)
ΔP
Crank Angle (°ATDC)

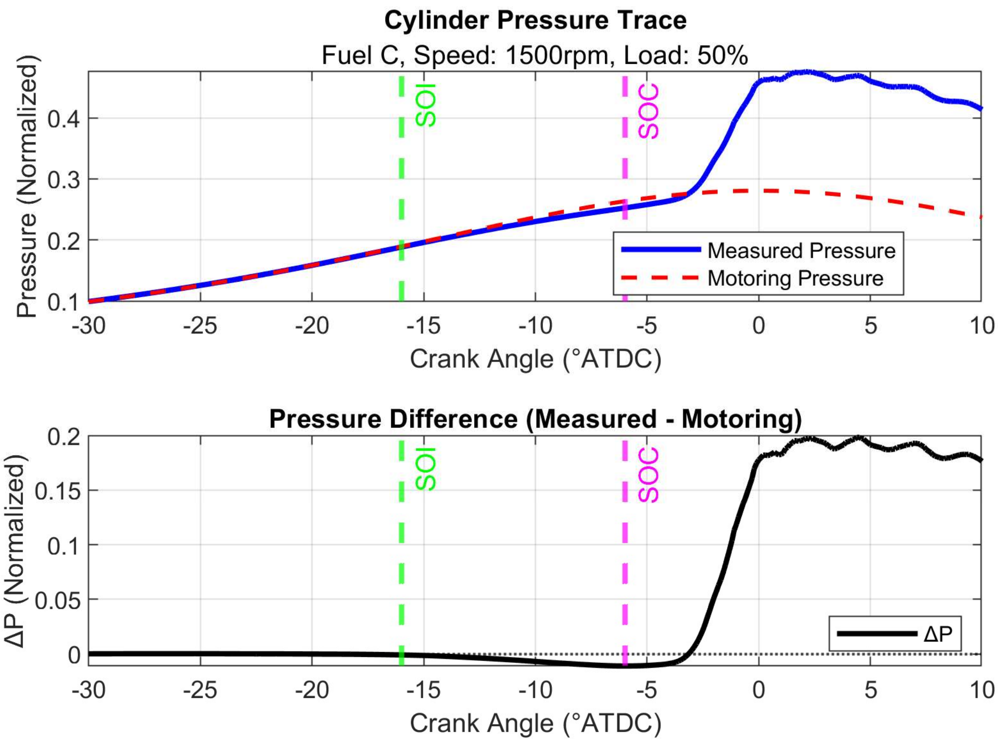
Cylinder Pressure Trace
Fuel C, Speed: 1500rpm, Load: 50%
Pressure (Normalized)
Crank Angle (°ATDC)
SOI
SOC
Measured Pressure
Motoring Pressure
Pressure Difference (Measured - Motoring)
ΔP (Normalized)
Crank Angle (°ATDC)
SOI
SOC
ΔP

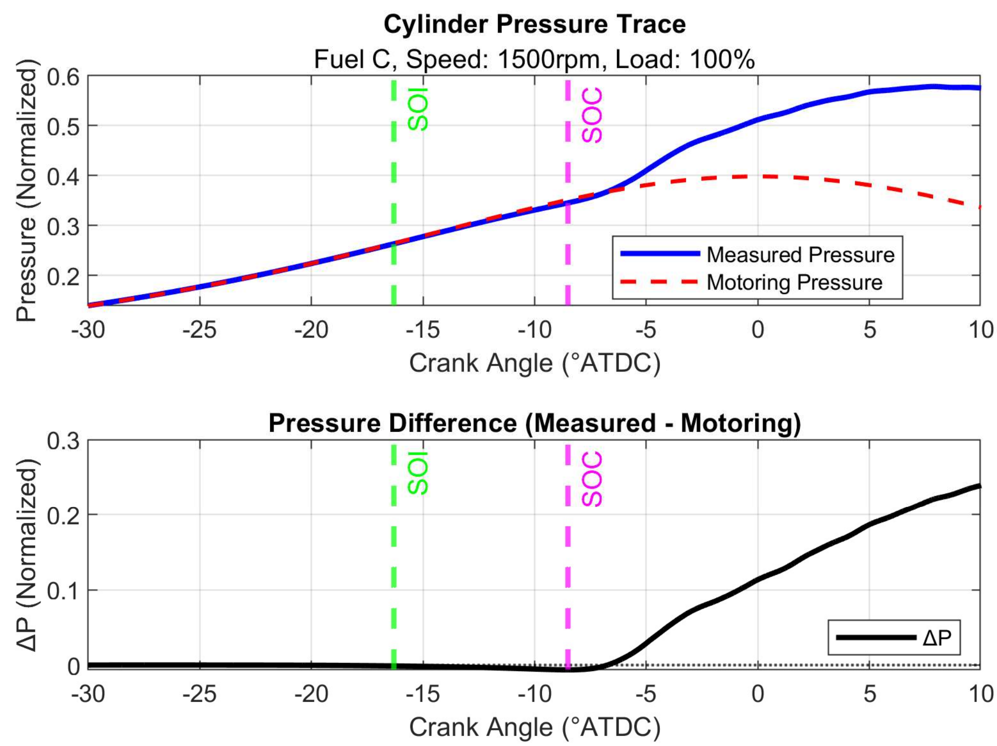
Cylinder Pressure Trace
Fuel C, Speed: 1500rpm, Load: 100%
Pressure (Normalized)
Crank Angle (°ATDC)
SOI
SOC
Measured Pressure
Motoring Pressure
Pressure Difference (Measured - Motoring)
ΔP (Normalized)
Crank Angle (°ATDC)
SOI
SOC
ΔP

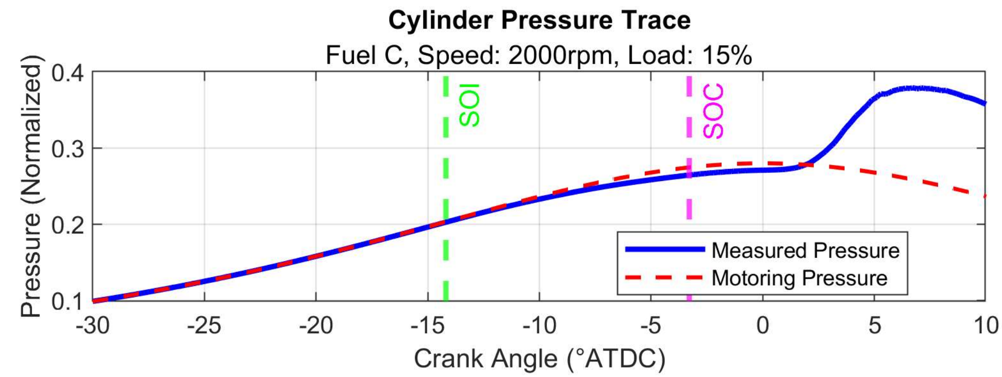
Cylinder Pressure Trace
Fuel C, Speed: 2000rpm, Load: 15%
Pressure (Normalized)
SOI
SOC
Measured Pressure
Motoring Pressure
Crank Angle (°ATDC)
Pressure Difference (Measured - Motoring)
ΔP (Normalized)
ΔP
Crank Angle (°ATDC)

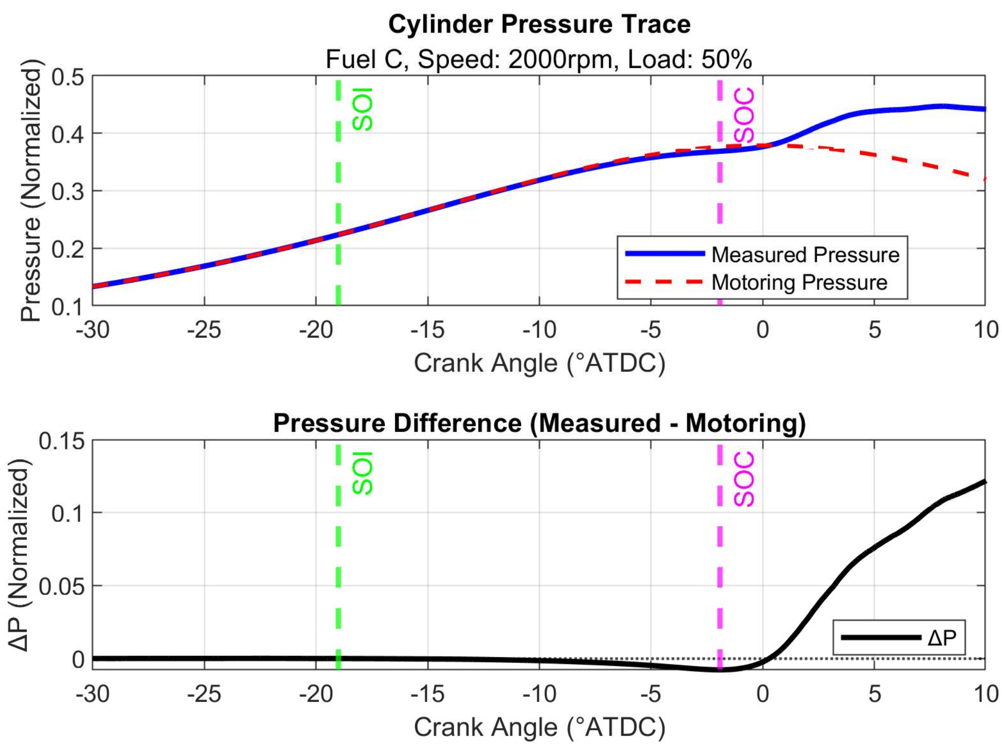
Cylinder Pressure Trace
Fuel C, Speed: 2000rpm, Load: 50%
Pressure (Normalized)
SOI
SOC
Measured Pressure
Motoring Pressure
Crank Angle (°ATDC)
Pressure Difference (Measured - Motoring)
ΔP (Normalized)
ΔP
Crank Angle (°ATDC)

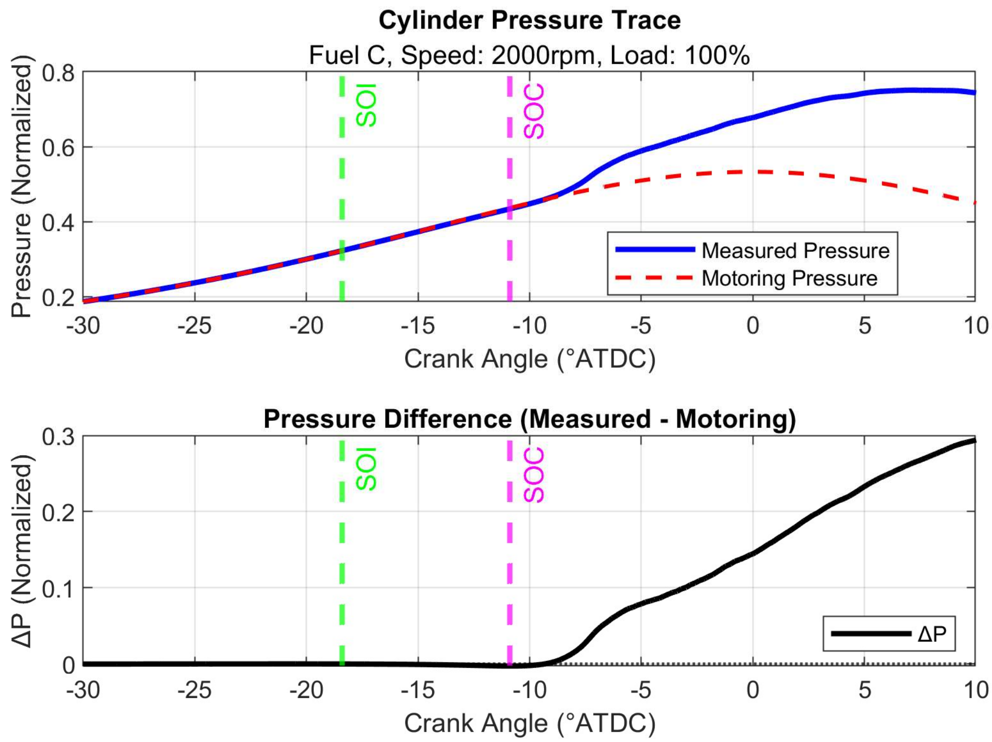
Cylinder Pressure Trace
Fuel C, Speed: 2000rpm, Load: 100%
Pressure (Normalized)
0.8
0.6
0.4
0.2
-30
-25
-20
-15
-10
-5
0
5
10
Crank Angle (°ATDC)
SOI
SOC
Measured Pressure
Motoring Pressure
Pressure Difference (Measured - Motoring)
ΔP (Normalized)
0.3
0.2
0.1
0
-30
-25
-20
-15
-10
-5
0
5
10
Crank Angle (°ATDC)
SOI
SOC
ΔP

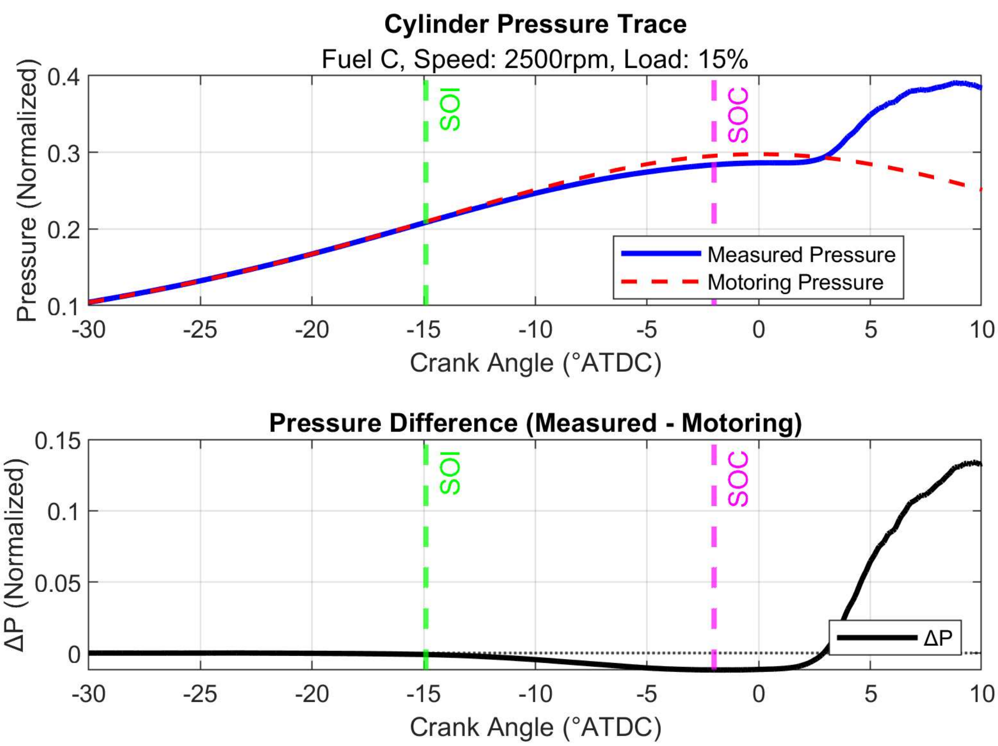
Cylinder Pressure Trace
Fuel C, Speed: 2500rpm, Load: 15%
Pressure (Normalized)
0.4
0.3
0.2
0.1
-30
-25
-20
-15
-10
-5
0
5
10
Crank Angle (°ATDC)
SOI
SOC
Measured Pressure
Motoring Pressure
Pressure Difference (Measured - Motoring)
ΔP (Normalized)
0.15
0.1
0.05
0
-30
-25
-20
-15
-10
-5
0
5
10
Crank Angle (°ATDC)
SOI
SOC
ΔP

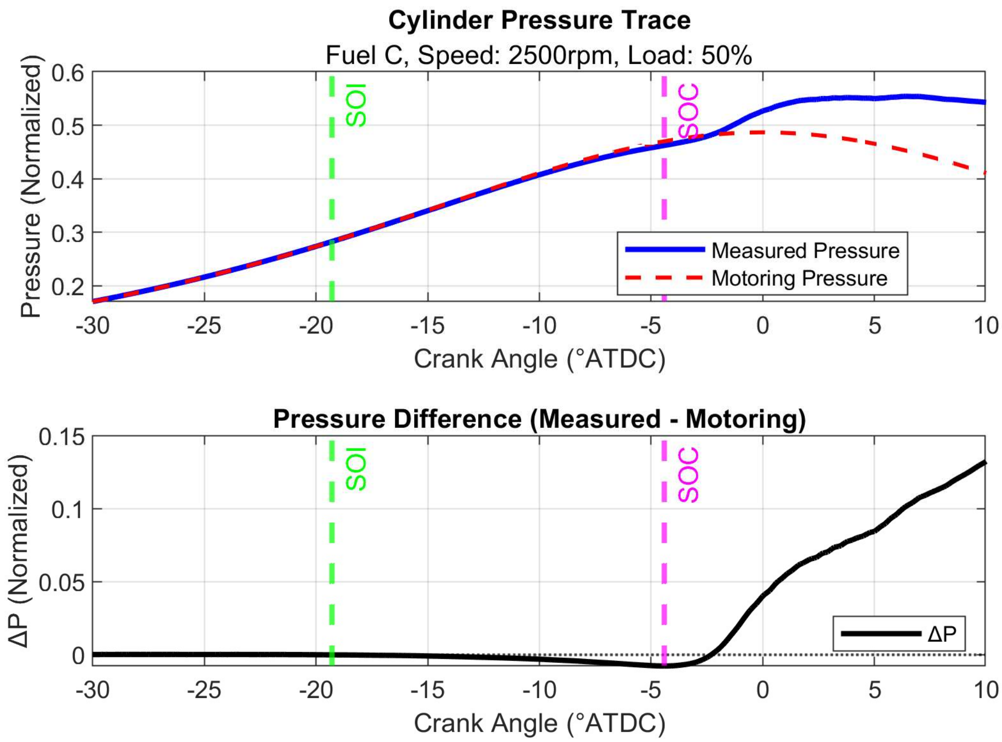
Cylinder Pressure Trace
Fuel C, Speed: 2500rpm, Load: 50%
Pressure (Normalized)
SOI
SOC
Measured Pressure
Motoring Pressure
Crank Angle (°ATDC)
Pressure Difference (Measured - Motoring)
ΔP (Normalized)
ΔP

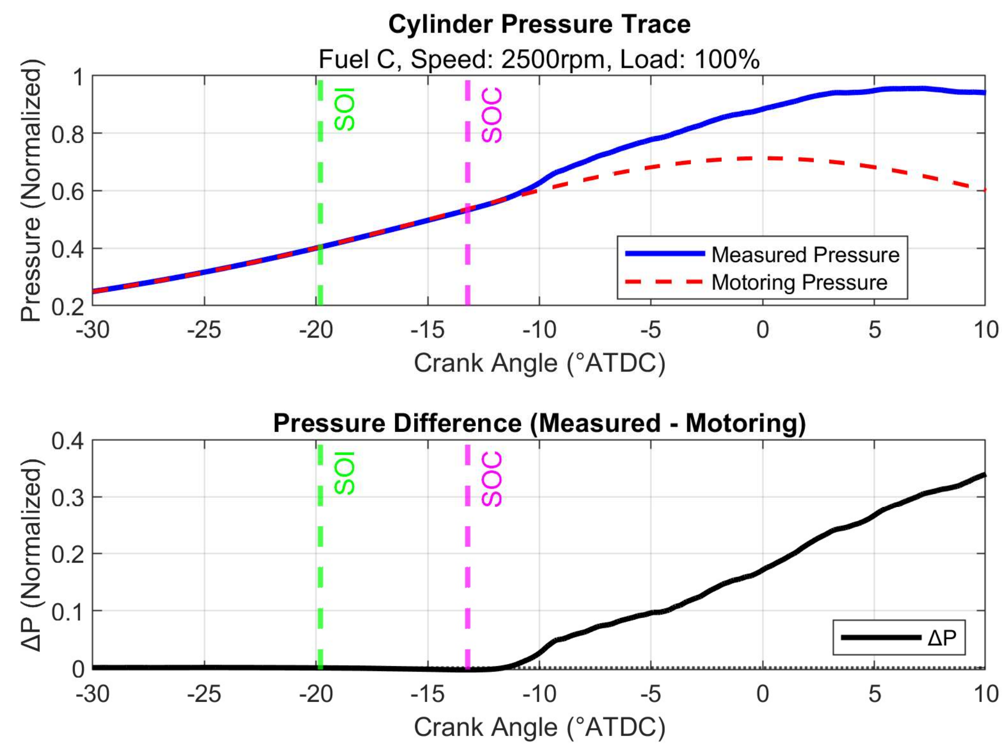
Cylinder Pressure Trace
Fuel C, Speed: 2500rpm, Load: 100%
Pressure (Normalized)
SOI
SOC
Measured Pressure
Motoring Pressure
Crank Angle (°ATDC)
Pressure Difference (Measured - Motoring)
ΔP (Normalized)
ΔP

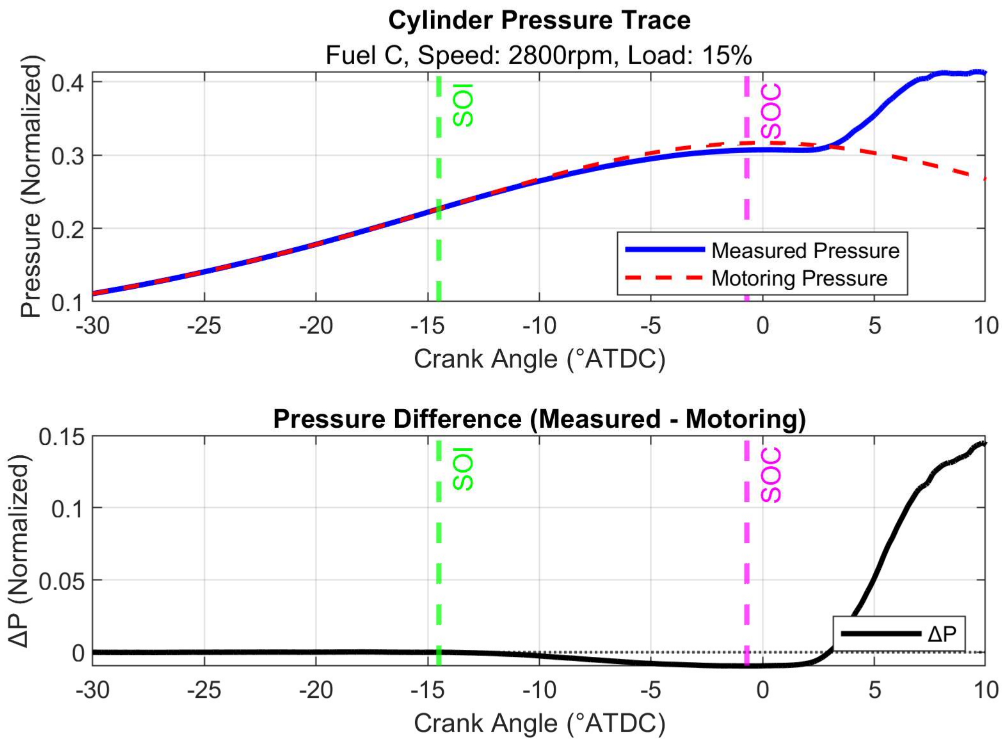
Cylinder Pressure Trace
Fuel C, Speed: 2800rpm, Load: 15%
Pressure (Normalized)
Crank Angle (°ATDC)
SOI
SOC
Measured Pressure
Motoring Pressure
Pressure Difference (Measured - Motoring)
ΔP (Normalized)
ΔP

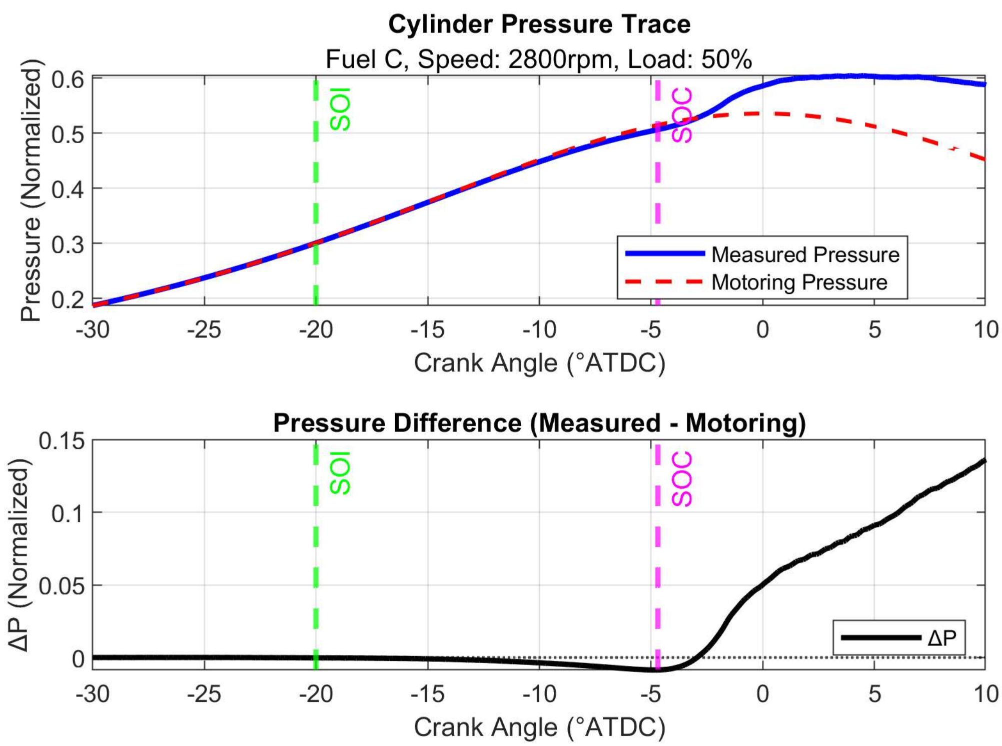
Cylinder Pressure Trace
Fuel C, Speed: 2800rpm, Load: 50%
Pressure (Normalized)
Crank Angle (°ATDC)
SOI
SOC
Measured Pressure
Motoring Pressure
Pressure Difference (Measured - Motoring)
ΔP (Normalized)
ΔP

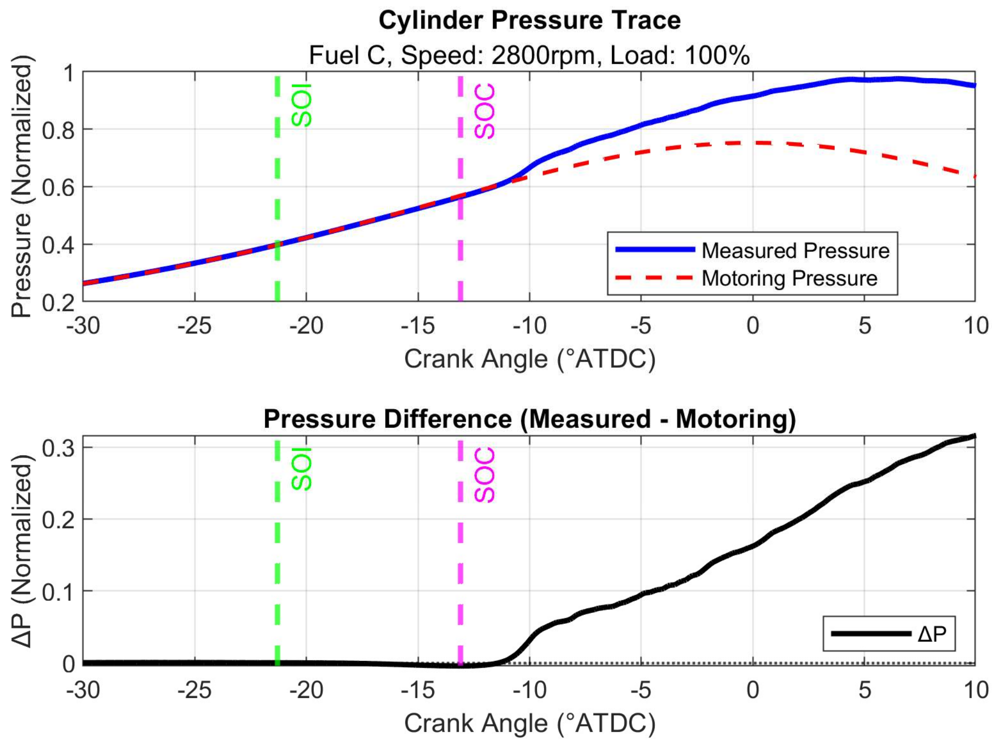
Cylinder Pressure Trace
Fuel C, Speed: 2800rpm, Load: 100%
Pressure (Normalized)
SOI
SOC
Measured Pressure
Motoring Pressure
Crank Angle (°ATDC)
Pressure Difference (Measured - Motoring)
ΔP (Normalized)
ΔP